

Czech Technical University in Prague

Faculty of Electrical Engineering

Department of Electromagnetic Field

**Feasibility Study of Microwave Differential Tomography
for Medical Diagnostics and Therapy**

Doctoral Thesis

Ing. Ilja Merunka

Prague, October 2020

Ph.D. Programme: Electrical Engineering and Information Technology (P2612)

Branch of study: Radioelectronics (2601V010)

Supervisor: Prof. Ing. Jan Vrba, CSc.

Supervisor-Specialist: Doc. Dr.-Ing. Jan Vrba, M.Sc.

Prohlášení

Prohlašuji, že dizertační práci: „Feasibility Study of Microwave Differential Tomography for Medical Diagnostics and Therapy“ jsem vypracoval samostatně s použitím literatury, kterou uvádím na seznamu přiloženém k této práci.

Declaration

I hereby declare that I have authored the doctoral thesis: "Feasibility Study of Microwave Differential Tomography for Medical Diagnostics and Therapy" on my own using the literature, which I list in the bibliography attached to this work.

In Prague on

Signature of the author

Abstract

Electromagnetic (EM) medical technologies are expanding worldwide for both diagnostics and therapy. As these technologies use non-ionizing radiation, have potential to be inexpensive and can often be used as minimally invasive, they have been in the focus of significant research efforts in recent years. The functional principle of these technologies is based on the existence of a difference in dielectric properties of different tissue types or between healthy and diseased tissues. Thus, accurate knowledge of the dielectric properties of biological tissues is fundamental to EM medical technologies. Over the past decades, numerous studies were conducted to expand the dielectric repositories. However, dielectric data is not yet available for every tissue type and at every temperature and frequency. Therefore, considerable attention is paid to this issue in this dissertation thesis.

This dissertation thesis is mainly focused on contribution to new technological approaches of microwave tomography (MWT), especially to its theory and near future clinical applications. I decided to concentrate mostly on the quantitative deterministic iterative approach. This approach seems to be the one of the most promising for medical application of MWT.

Further in this work, a prototype of a laboratory microwave imaging system suitable to methodically test the ability to image, detect, and classify human brain strokes using microwave technology is presented. It consists of an antenna array holder equipped with ten newly developed slot bowtie antennas, a 2.5 D reconfigurable and replaceable human head phantom, stroke phantoms, and related measuring technology and software. This prototype was designed to allow measurement of a complete S-matrix of the antenna array. The reconfigurable and replaceable phantom of human head has 23 predefined positions for stroke phantom placement. This setting allows repeated measurements for the stroke phantoms of different types, sizes/shapes, and at different positions. It is therefore suitable for large-scale measurements with high variability of measured data for stroke detection and classification based on machine learning methods. To verify the functionality of the measuring system, complete S-parameters matrix was measured for a hemorrhagic phantom sequentially placed on mentioned 23 positions and spatial distribution of dielectric parameters was reconstructed using implemented deterministic iterative reconstruction algorithm. The results correlate well with the actual position of the stroke phantom and its type. Our results support the statements of other groups working in this field, that the detection and differentiation of the strokes by means of microwave technique should be possible.

Combinations of microwave hyperthermia system (MHTS) and non-invasive differential temperature measurement system based on MWT is discussed in this dissertation thesis as well.

In conclusion - The following 5 main aims of this dissertation thesis (focussed on new development of microwave technologies to be used for MWT) can be summarized as follows:

- Design of special antenna systems for microwave tomography (Chapter 3, 5 and 9)
- Complex permittivity measurement of human tissues (Chapter 6)
- Study of reconstruction algorithms for microwave tomography and its implementation (Chapter 2, 7 and 8)
- Development of a system for brain stroke detection and classification (Chapter 2, 4 and 9)
- Development of temperature dependent model of dielectric properties of an agar phantom for testing of a system combining MHTS and MWT (Chapter 5)

Keywords: Microwave tomography, brain stroke detection, medical diagnostics, complex permittivity measurement.

Anotace

Elektromagnetické (EM) lékařské technologie jsou považovány za perspektivní jak pro diagnostiku, tak i pro terapii. Vzhledem k tomu, že tyto technologie využívají neionizující záření, mají potenciál být levné a velmi často je lze provozovat minimálně invazivně, byly v posledních letech předmětem významného výzkumného úsilí. Funkční princip těchto technologií je založen na existenci rozdílu v dielektrických vlastnostech různých typů tkání nebo mezi tkáněmi zdravými a patologickými. Znalost přesných dielektrických vlastností biologických tkání je proto pro lékařské EM technologie zásadní. Během posledních desetiletí byly provedeny četné studie za účelem rozšíření databází dielektrických vlastností biologických tkání. Nicméně tato data stále nejsou k dispozici pro všechny druhy tkání, pro danou teplotu a frekvenci. Těto problematice je proto v dizertační práci věnována značná pozornost.

Tato disertační práce je ale zaměřena především na příspěvek k novým technologickým přístupům mikrovlnné tomografie (MWT), zejména k její teorii a klinickým aplikacím v blízké budoucnosti. Konkrétně je cílena na využití kvantitativního deterministického iterativního rekonstrukčního algoritmu. Tento přístup se pro aplikaci MWT v medicíně zdá být jedním z nejslibnějších.

Dále je v této disertační práci představen prototyp laboratorního mikrovlnného zobrazovacího systému vhodného pro metodologické testování zobrazování, detekce a klasifikace cévních mozkových příhod pomocí mikrovlnné technologie. Skládá se z držáku anténního pole vybaveného deseti nově vyvinutými šterbinovými anténami, 2.5 D rekonfigurovatelného a vyměnitelného fantomu lidské hlavy, fantomů mrtvice a související měřicí technologie a softwaru. Tento prototyp byl navržen tak, aby umožňoval měření kompletní S-matice anténního pole. Rekonfigurovatelný a vyměnitelný fantom hlavy má 23 předdefinovaných pozic pro umístění fantomu mozkové příhody. Tím je umožněno opakované měření fantomů mozkových příhod různých typů, velikostí / tvarů a na různých pozicích. Navržený fantom je proto vhodný pro opakovaná měření s vysokou variabilitou naměřených dat pro detekci a klasifikaci mozkové příhody na základě metod strojového učení. Pro ověření funkčnosti měřicího systému bylo provedeno měření kompletní matice S-parametrů s použitím fantomu krvácivé mozkové příhody umístěným postupně na všech zmíněných 23 pozicích. Na takto naměřená data byl aplikován implementovaný deterministický iterativní rekonstrukční algoritmus prostorového rozložení hodnot dielektrických vlastností. Dosažené výsledky dobře korelují se skutečnou polohou fantomu mozkové mrtvice a jeho typem. Naše výsledky tak podporují tvrzení dalších skupin pracujících v této oblasti, že by detekce a diferenciací cévních mozkových příhod pomocí mikrovlnné techniky měla být možná.

V této disertační práci je také diskutována kombinace mikrovlnného hypertermického systému (MHTS) a neinvazivního systému měření diferenční teploty na základě MWT.

Na závěr - následujících 5 hlavních cílů této disertační práce (zaměřených na nový vývoj mikrovlnných technologií pro využití v MWT) lze shrnout takto:

- Návrh speciálního anténního systému pro mikrovlnnou tomografii (kapitola 3, 5 a 9)
- Měření komplexní permitivity lidských tkání (kapitola 6)
- Studium rekonstrukčních algoritmů pro mikrovlnnou tomografii a jejich implementace (kapitola 2, 7 a 8)
- Vývoj systému pro detekci a klasifikaci mozkové mrtvice (kapitola 2, 4 a 9)
- Vývoj modelu teplotní závislosti dielektrických vlastností agarového fantomu pro testování systému kombinující MWT a MWT (kapitola 5)

Klíčová slova: Mikrovlnná tomografie, detekce mozkové příhody, zdravotnická diagnostika, měření komplexní permittivity.

Acknowledgments

First, I would like to thank to my supervisors, Prof. Ing. Jan Vrba, Ph.D and Doc. Dr.-Ing. Jan Vrba, M.Sc., for their valuable consultations and advises during my whole Ph.D studies. It helped me to achieve good results which are presented in this doctoral thesis.

I would like to thank also to the whole Department of electromagnetic field, especially to the head of this department, Prof. Ing. Pavel Pechač, Ph.D, for a very nice and inspiring working environment and support.

Notation

<i>Symbol</i>	<i>Unit</i>	<i>Quantity</i>
\mathbf{r}	(m)	Position vector
\mathbf{E}	(V/m)	Electric field
\mathbf{H}	(A/m)	Magnetic field
\mathbf{D}	(C/m ²)	electric flux density
\mathbf{B}	(Wb/m ²)	magnetic flux density
\mathbf{J}	(A/m ²)	Electric current density
ρ	(C/m ³)	Volume electric charge density
j	-	Imaginary unit
J	-	Jacobian matrix
I	-	Identity matrix
S_{11}	(dB)	Module of S-parameter
SAR	(W·kg ⁻¹)	Specific absorption rate
σ	(S·m ⁻¹)	Electric conductivity
ρ	(kg·m ⁻³)	Tissue density
x	(m)	Distance
ϑ	(°C)	Temperature
V	(m ³)	Volume
ϵ_r	(-)	Relative permittivity
c_0	(m·s ⁻¹)	Speed of light
$\hat{\epsilon}$	(F·m ⁻¹)	Complex permittivity
μ	(H·m ⁻¹)	Permeability
μ_0	(H·m ⁻¹)	Permeability of vacuum
ϵ_0	(F·m ⁻¹)	Permittivity of vacuum
ϵ'	(F·m ⁻¹)	Real part of complex permittivity
ϵ'_r	(-)	Real part of relative permittivity
ϵ''	(F·m ⁻¹)	Imaginary part of complex permittivity
ϵ''_r	(-)	Imaginary part or relative permittivity
ϵ_∞	(F·m ⁻¹)	Permittivity at infinite frequency
ω	(s ⁻¹)	Angular frequency
$\Psi^{(n)}$	(-)	n-th scattered data/measurements
Γ		Classification accuracy
Ξ		Classification error

Contents

1.	Microwave Imaging: State of the Art	1
1.1	Introduction	1
1.2	Hardware solutions and reconstruction algorithms	2
1.3	Radar based approach	2
1.4	Microwave tomography.....	2
1.5	Main aims of dissertation thesis	4
1.6	Description/Overview of dissertation thesis.....	5
2.	Image Reconstruction Algorithm: Iterative algorithm with Gauss Newton optimization	9
2.1	General definitions.....	9
2.1.1	Basic concepts - EM field.....	9
2.1.2	Placement of an object into the propagation/background medium	10
2.2	Description of iterative algorithm with Gauss Newton optimization	11
2.2.1	Image reconstruction procedure	12
3.	Antenna Elements for Microwave Tomography	13
3.1	Comparison of four different antenna elements.....	13
3.1.1	Criteria for evaluation of the antennas.....	13
3.1.2	Selected antennas and evaluation scenario	13
3.1.3	Numerical simulations.....	14
3.1.4	Results	15
3.1.5	Conclusion of the antenna element comparison.....	17
3.2	Novel bowtie slot antenna for microwave imaging of strokes and its comparison to the waveguide based antenna	17
3.2.1	Desired parameters of new antenna element.....	18
3.2.2	Compared antenna elements	18
3.2.3	Numerical results and discussion.....	19
3.2.4	Manufacturing reproducibility of bowtie slot antenna	21
3.2.5	Conclusion of comparison of bowtie slot and waveguide based antenna elements	22
4.	Laboratory Microwave Imaging System for Detection and Classification of Strokes	23
4.1	Data acquisition	23
4.1.1	Measuring setup	23
4.1.2	Measuring container and antennas	24
4.1.3	Calibration procedure	24
4.1.4	Liquid phantoms preparation	25
4.1.5	Measuring procedure.....	25
4.2	Results	25
4.2.1	Measured data	26

4.2.2	Detection of stroke and its position.....	27
4.3	Conclusion.....	28
5.	Temperature Dependent Complex Permittivity Model of Agar Phantom for Microwave Temperature Distribution Monitoring During Microwave Hyperthermia Treatment.....	31
5.1	Introduction.....	31
5.2	Measuring set up.....	31
5.3	Measurement procedure.....	32
5.4	Data processing.....	33
5.5	Results.....	33
5.6	Conclusion - noise in measured data and sensing volume.....	33

Chapters 6, 7, 8 and 9 are based on the papers published in peer-reviewed journals.

6.	Dielectric Measurement of Biological Tissues: Challenges and Common Practices.....	41
6.1	Introduction.....	42
6.2	Tissue Dielectric Properties: Background and Relevant Works.....	44
6.2.1	Basics of Dielectric Properties.....	44
6.2.2	Dielectric Property Studies in the Literature.....	45
6.3	Measurement Approaches.....	47
6.3.1	Overview of Measurement Techniques.....	47
6.3.2	Evolution of the Coaxial Probe Design and Fabrication.....	50
6.4	Calibration and Confounders.....	51
6.4.1	Standard Calibration.....	51
6.4.2	Calibration Procedure and Confounders.....	52
6.4.3	Confounders Introduced in the System after Calibration.....	54
6.5	Validation and Measurement Uncertainty.....	54
6.5.1	Validation Liquids: Models, and Their Advantages and Disadvantages.....	55
6.5.2	Uncertainty Calculation.....	58
6.6	Tissue Sample Preparation and Measurement Procedure.....	59
6.6.1	Probe Selection Considerations.....	59
6.6.2	Tissue Preparation and Handling.....	61
6.6.3	Procedure for Tissue Measurements.....	64
6.7	Tissue Sample Histological Analysis.....	67
6.7.1	Factors Impacting Histological Analysis.....	67
6.7.2	The Link between Heterogeneity, Histology, and Sensing Volume.....	68
6.7.3	Histological Analysis Techniques in Dielectric Studies.....	69
6.8	Discussion and Conclusions.....	70

7.	Real-Time Brain Stroke Detection Through a Learning-by-Examples Technique—An Experimental Assessment	83
7.1	Introduction	84
7.2	Mathematical formulation	84
7.3	Experimental validation	86
7.4	Conclusion	88
8.	Instantaneous Brain Stroke Classification and Localization from Real Scattering Data	91
8.1	Introduction	92
8.2	Brain stroke classification and normalization method	93
8.3	Experimental assessment.....	94
8.4	Conclusion.....	96
9.	Microwave Tomography System for Methodical Testing of Human Brain Stroke Detection Approaches	99
9.1	Introduction	100
9.2	Microwave Imaging System Description.....	101
9.2.1	Phantoms of Head and Brain Strokes, Antenna Array	101
9.2.2	Antenna Elements.....	101
9.2.3	Measurement Setup and Settings.....	103
9.2.4	Calibration.....	103
9.2.5	Liquid Phantom Composition and Dielectric Properties.....	104
9.2.6	Measuring Procedure.....	104
9.3	Measured Data.....	104
9.4	Application of Image Reconstruction Algorithm to Measured Data.....	105
9.5	Image Reconstruction Procedure.....	105
9.6	Discussion.....	107
9.7	Conclusion.....	108
10.	Thesis Conclusion	111
10.1	Summary	111
10.2	Conclusion	113
11.	Publications of the author.....	115
11.1	Publications in journals with an impact factor.....	115
11.1.1	Publications related to the thesis	115
11.1.2	Publications not related to the thesis	115
11.2	International conference contributions.....	116
11.2.1	International conference contributions related to the thesis	116
11.2.2	Abstracts related to the thesis	117
11.2.3	International conference contributions not related to the thesis.....	117

11.3	Scientific projects participation	119
11.3.1	International projects.....	119
11.3.2	National projects	119
11.4	Membership in conference organizing committee.....	119
11.5	International internship	119
11.6	Special awards.....	119

List of figures

Figure 2.1, Flowchart of reconstruction procedure – one iteration.	12
Figure 3.1, Compared antennas - Microstrip patch antenna with cut out sides (I.), microstrip folded patch antenna (II.), waveguide antenna (III.) and coaxial monopole wire antenna (IV.).	14
Figure 3.2, Measuring container and positions of active antennas (A1 and A2).	14
Figure 3.3, $ S_{11} $ and $ S_{21} $ parameters for tested antennas.	15
Figure 3.4, Comparison of isolines of electromagnetic power loss density for every antenna in x-y plane (1 GHz) in linear scale.	16
Figure 3.5, Sensitivity of S parameters to a change in dielectric properties of the phantom. Colors of the lines correspond to the antennas (same like in previous figures).	17
Figure 3.6, Geometries of rectangular waveguide-based (a) and bowtie slot (b) antenna elements.	18
Figure 3.7, Dimensions of the bowtie slot antenna element.	19
Figure 3.8, Layout of the main container for liquid head phantom. Red and blue circles represent different positions of antenna elements and different positions stroke phantoms, respectively. Height of the main container is 20 cm and the antenna plane lies in the middle of the height.(a) 3D view and (b) 2D section of the head phantom: antenna (red circles) and stroke admissible locations (blue crosses).	19
Figure 3.9, Magnitude of reflection (a) and transmission (b) coefficients for two considered antenna elements.	20
Figure 3.10, Magnitudes of all independent (due to the symmetry of the simulated geometry) S-parameters for both considered antenna elements. MN marks the antenna numbers.	20
Figure 3.11, Normalized differences in transmission coefficients for the MWT system without inhomogeneity and with inhomogeneity ($\sigma = 0.6$ S/m and $\epsilon_r = 30$) - sensitivity of the system to the presence of non-homogeneity. Bowtie slot antenna (a) and rectangular waveguide-based antenna (b).	20
Figure 3.12, Isolines of the module of electric field intensity phasor in the planes xy (a) and xz (b). Isolines correspond to 10%, 1% and 0.1% of the maximum module of electric field intensity phasor at the aperture of the rectangular waveguide-based antenna.	21
Figure 3.13, Photograph of manufactured bowtie slot antennas.	21
Figure 3.14., Measured reflection coefficients of manufactured bowtie slot antennas, respectively.	21
Figure 4.1, A photograph of the measuring setup.	24
Figure 4.2, 3D model of measuring container with antennas and cylindrical sample holder – inhomogeneity. ...	25
Figure 4.3, Dimensions of measuring container with marked positions of stroke phantom.	25
Figure 4.4, Example of measured data – real and imaginary part of measured S-parameter matrix when the measuring container was filled with homogenous phantom only and when the inhomogeneities were included subsequently.	26
Figure 4.5, Differences in measured signals (haemorrhagic stroke phantom at position P1 vs. grey matter phantom) are represented by green bars, with standard deviations ($2 \cdot \text{std}_{HA} + 2 \cdot \text{std}_{Empty}$) represented by blue bars on the top. Results of T-test at the significance level of 1 % are represented by black stars (0.01 – hypothesis was not supported, 0 hypothesis was supported).	27
Figure 4.6, Standard deviation in measured S parameters for all positions of strokes together.	27

Figure 4.7, Cumulative images showing detection of strokes (every color represents one position – namely P1, P2, P3, P4, P5, P17, P18, P19, P25) a), b) – synthetic data, hemorrhage, c), d) – synthetic data necrosis, e), f) – measured data, hemorrhage, g), h) – measured data necrosis.	29
Figure 5.1, Measuring setup for measurement of complex permittivity of the agar phantom at different temperatures. (PC – personal computer, VNA – vector network analyser, T – thermometer and temperature stable water bath).....	32
Figure 5.2, Procedure of complex permittivity measurement.....	32
Figure 5.3, Data processing procedure.	33
Figure 5.4, Measured complex permittivity of distilled water (solid lines) with standard uncertainty together with fitted model (dashed lines).	34
Figure 5.5, Measured complex permittivity of agar phantom (solid lines) with standard uncertainty together with fitted model (dashed lines).	34
Figure 5.6, A 25 dB decrease in amplitude of E-field in deionized water for different frequencies.....	35
Figure 5.7, Measurement on the same agar phantom but after calibration with 0.1 M NaCl in the same container.	35
Figure 6.1, Open-ended coaxial probe technique: (a) Schematised measurement set-up, including the Vector Network Analyser (on the right), the cable connecting one port of the VNA to the coaxial probe, the probe bracket, and the liquid sample being measured; (b) top and side cross-sections of the coaxial probe, with electric field orientation indicated.	49
Figure 6.2, Flow chart of the common steps to minimise tissue-related errors in in vivo and ex-vivo measurements.	66
Figure 6.3, Diagram of sample composition by tissue type (fat—orange, gland—blue). A side view of the sample is shown, with slices marked. The dielectric probe measurement location is denoted with a black oval on the top of Slice	68
Figure 7.1, 3D view and of the head phantom (D_{inv}).....	86
Figure 7.2, 2D section of the head phantom (D_{inv}): antennas positions (red dots) and admissible locations (blue crosses).....	86
Figure 7.3, Experimental MI system for real-time brain stroke detection.	87
Figure 7.4, Behaviour of the classification accuracy and error versus the number of training samples considered during the off-line phase.....	88
Figure 8.1, Geometry of the test scenario with the head phantom model (D), T = 10 sources/receivers, and the Q = 23 admissible brains stroke positions.....	93
Figure 8.2, Experimental MI system for real-time brain stroke imaging.	95
Figure 8.3, Experimental Assessment (Brain Stroke Classification, M = 230) – classification accuracy index, Γ , vs training size, N.....	95
Figure 8.4, Experimental Assessment (Brain Stroke Localization, M = 230) – classification accuracy index, Γ , vs training size, N.....	96
Figure 9.1, Bottom view of measuring container with marked positions of the stroke phantoms. Black: walls of the antenna holder, yellow: antennas with ports, blue: matching liquid, white: head phantom vessel,	

green: liquid phantom of human head, and red: liquid phantom of stroke at position P7 (all dimensions are in mm).	102
Figure 9.2, 3D model of measuring container with antennas and cylindrical phantom of stroke marked blue (a) and the photograph of the measuring setup (b).	102
Figure 9.3, Photograph of the antenna element from the side facing to the phantom (a) (dimensions in cm) and measured magnitude of S11 for all antennas in frequency range 0.6 - 1.4 GHz heading to the liquid homogeneous phantom of human head (b). Central operating frequency is marked by a dashed line. ..	103
Figure 9.4, Response of the system ((a) relative change in the modulus of S-matrix and (b) change in the phase of S-matrix in degrees) to a presence of the hemorrhagic stroke phantom at 23 different positions (y axes) in the phantom of human head.	105
Figure 9.5, Results (a, b) of iterative reconstruction procedure for hemorrhagic stroke phantom at position P7 (marked by white circle) and evolution (c, d) of relative permittivity and conductivity over the iterations (i = 1 for the first iteration, i = 10 for the tenth iteration) on the line going through the center of the stroke phantom (marked by dashed white lines). Actual values of both relative permittivity and conductivity are marked by solid black lines in graphs (c) and (d).	106
Figure 9.6, Detection of position of the strokes from reconstructed images. Circles mark the actual position of the stroke; dots of adequate color show the detected positions.	107

List of tables

Table 3.1, Maximal sizes, reflection, transmission and bandwidth of compared antennas	15
Table 4.1, Phantoms composition and measured dielectric parameters at 1 GHz. Compositions are in weight percent at 20 °C.....	25
Table 6.1. Use of the commercial probe in recent works. Studies involving breast tissues are shaded in grey. The others involve liver tissues, apart from the porcine skin study in Karacolak et al. [116]. In the column “Relative permittivity range”, the extreme values in relative permittivity are reported from lower to higher frequencies.....	51
Table 6.2, The standard calibration process: Common errors or confounders that occur for each step in the calibration process, along with the possible correction or compensation techniques. The open circuit, short circuit, and a liquid load material are shown as the three calibration standards.	52
Table 6.3, Reference liquid properties, available models, and storage and handling procedures (where f = frequency, T = temperature).....	57
Table 6.4, Example calculations of total uncertainty in dielectric data resulting from tissue-related confounders under different measurement scenarios: Uncertainty due to time from excision (μ TFE), due to temperature (μ T), and due to age (μ A). μ is the total uncertainty added to dielectric data, calculated as combined standard uncertainty. Uncertainty data is for the relative permittivity of mouse liver at 900 MHz, obtained from the literature. Note that 0.91% is $0.13\%/^{\circ}\text{C} \cdot 7^{\circ}\text{C}$	71
Table 7.1, the number of false positives and negatives (i.e., test samples wrongly assigned to class -1 and +1) for a set of representative training sizes.....	88
Table 9.1, Phantom Phantom composition in weight percent, target, and measured dielectric parameters at 1 GHz and 25°C, immediately before the measurement in the MWI system.	104
Table 9.2, Maximal values of dielectric parameters for the selected positions of the stroke phantom after the reconstruction.	107

1. Microwave Imaging: State of the Art

1.1 Introduction

Microwave imaging (MWI) in the field of medical applications became very interesting from several points of view. It has been proposed, studied and implemented by many institutions for the last 20 years [1]. MWI is often compared with other applications of electromagnetic field in medical imaging systems as X-rays, Computed Tomography (CT) and Magnetic Resonance Imaging (MRI). Very detailed comparison of these imaging systems could be done according to many different aspects, but the main strengths and shortcomings of MWI could arise from simple overview as well.

If we want to categorize the MWI system between these existing well known and widely used systems we could say the following:

- MWI is closer to the CT from the reconstruction algorithms point of view.
- MWI does not incorporate an ionizing radiation which is similar to the MRI systems.

Unfortunately, the ray based algorithms (back-projection) cannot be utilized, because the scattering effects cannot be neglected (nonlinear inverse problem) as it is in the case of CT.

Diagnostic information given by MWI is also different. As far as CT gives information about distribution of tissues densities and MRI information about distribution of protons densities or relaxations times of protons, MWI gives information about distribution of dielectric parameters inside the region of interest (ROI) [2] (Different tissues, especially tumorous tissue and healthy tissue has different dielectric parameters [3]).

It has been demonstrated that MWI is applicable for extremities imaging, like e.g. breast cancer detection, diagnostics of lung cancer, brain imaging and cardiac imaging [4]. Application of MWI in the area of osteoporosis detection and bone health monitoring seems to be feasible too because there are studies showing dielectric property variations with respect to its mineral density [1].

However, there are two main applications of MWI in medicine at this time – early breast cancer detection and brain stroke diagnosis [5]. Although 30% to 40% lower risk of dying from breast cancer was achieved when screened using mammography taken as current gold standard [6], only 56% of cancers are revealed in premenopausal women. Mammography has an overall 50% false positive, which leads to unnecessary biopsy, is uncomfortable, uses ionizing radiation and is potentially harmful for many women [5]. Reacting on the foregoing shortcomings of the mammography most of the MWI system are developed for human breast cancer diagnosis. Moreover, human breast tissue and the shape of the human breast seems to be the most suitable for MWI diagnostic devices, because the human breast tissue is low loss and the contrast between a normal and malignant tissue seems to be significant [7]. It is generally expected, that the MWI in medicine could play role as a cheap, fast and easy to use systems for diagnosis of cancer (especially breast cancer) in its early stages in the future.

Main strengths of the MWI are:

- Use of nonionizing radiation.
- Non-invasivity.
- Cost effectiveness.
- Portability.

Main shortcomings of the MWI are:

- Accuracy and resolution (both time and spatial).
- Computational intensity of reconstruction algorithms.
- Sensitivity to the noise.

The crucial parts of MWI systems are:

- Receiving and transmitting antennas.
- Coupling medium.
- Data acquisition system.
- Reconstruction / detection algorithms.

1.2 Hardware solutions and reconstruction algorithms

Several different MWI systems have already been developed. These can be simply differentiated according to the used reconstruction algorithms because there is a strong relationship between the software and hardware solutions. Two main approaches can be distinguished in MWI:

- Microwave tomographic imaging (MWT).
- Radar based imaging (RB) methods.

In the MWT, inverse scattering problem must be solved, while in the RB methods linear inverse problem is considered [8]. Example of MWT based system under clinical test can be found in [9], example of RB based system in [10], [11] and others.

According to another criteria, we can find single frequency and multi frequency systems and systems able to get qualitative or quantitative information [12]. In general, there is a set of antennas equidistantly placed around the ROI (Region of Interest) in one or more circles, or one antenna is moving around the ROI. Usually, antennas are placed in a tank which is filled with a coupling medium. Type of the antennas as well as hardware used to generate and measure signals depends on the type of the MWI system. Detection algorithms of tumours could be taken as special class (third) of MWI systems, too. These are mostly based on machine learning methods and classification of the measured signals [13].

1.3 Radar based approach

These approaches are working in time domain and its working scheme can be explained using the radar. Position of the contrast in dielectric properties in a ROI can be derived from delays between transmitted and reflected ultra-wideband pulses. Some assumptions about the propagation speed of EM field in the ROI must be done before the reconstruction. Radar based methods are mostly used to find the presence or location of the scatterers - qualitative information. Reconstruction is fast with potential of real time microwave imaging [14], because these methods are not iterative. RB approaches perform well in high contrast media. The main issues of RB approaches are the maximal resolution of reconstructed image depending on the bandwidth of the pulse, possible variations in propagation speed in the ROI and the multi path effect (many reflections from scatterers). Confocal microwave imaging (CMI) [15]–[17] incorporating delay and sum algorithm and its improved versions [18] are the most frequently used reconstruction methods based on the radar approach.

1.4 Microwave tomography

Microwave tomography is an approach which reconstructs the distribution of dielectric parameters inside the ROI by solving the inverse scattering problem. The inverse scattering problem is in general nonlinear and computational methods are utilized to solve it [8]. The most critical aspect of an inverse scattering problem is usually its ill-posedness [19]. The problem is

well-posed if its solution exists, it is unique and a small perturbation of the data results in a small perturbation in the solution, otherwise the problem is ill-posed and regularization procedures (Tikhonov regularization, including a priori information etc.) should be applied. When the objects are of low contrast and the multiple scattering effects are small, linearization of the inverse problem can be done in several ways (Born approximation, Rytov approximation and its improved versions). On the other hand, when the multiple scattering cannot be neglected, nonlinear reconstruction algorithms based on linearization procedures and/or optimization procedures (stochastic or deterministic) are used [8]. The goal of the optimization procedure is to minimize the error between the measured data and data from numerical solution of the forward problem. More detailed classification of the MWT approaches can be found in [8] or [19].

The quantitative stochastic iterative approaches [20] using forward solver seem to be the one of the most promising for medical application of MWT [8]. The stochastic methods are able to reach the global minimum of the cost function even if starting far from the final solutions. Including of a priori information and a limitation of a search space can be simply implemented [20] and can stand in for the regularization terms.

On the other hand, deterministic methods (using local optimization) performs faster because lower number of iterations (solutions of forward problem) is needed. Thus, deterministic methods are still great choice for problems which can be considered linear (weak scatters in the ROI). Local optimization procedure Gauss/Newton with log transformation together with Marquardt regularization was used in [21]. FDTD based forward solver was used. Reconstruction time equals to about 1 minute (13 iterations of algorithm) per slice. The coupling medium composes from glycerin and water (86:14). This mixture has non zero conductivity to reduce multipath scattering. The system includes 16 monopole antennas placed on the circle with diameter of 15.2 cm. The measurement on frequencies 500-1700 MHz with step 200MHz in 7 different slices takes about 4 minutes. The results from MWT were compared with results from MRI.

Plenty of different global optimization algorithms have been utilized to MWT. Some of the works dealing with stochastic MWT approaches are mentioned subsequently. Comprehensive review of optimization procedures based on evolutionary algorithms (EA) and its application into inverse scattering problematics can be found in [22] - EAs allow straightforward introduction of a priori information or constraints, they are intrinsically parallel algorithms and able to deal with floating point, discrete and binary unknowns simultaneously. EAs are suitable to face ill-posedness and nonlinearity. Between main drawbacks belong computational intensity and low convergence rates close to the global solution. Proper choice of EA, taking into account physical constraints, including of a priori information, careful definition of cost function, tuning of the control parameters and benchmark of the EA are the critical point for successful application of EA into the MWT. Dealing with the computational issues can be done by reducing the number of parameters to estimate, to consider multi-resolution strategy or multi-stage reconstruction, hybridizing the EA with a deterministic optimizer, using the fast forward solvers for secondary unknowns in every iteration and implementing EA parallel.

The particle swarm optimization procedure was used to estimate three parameters (position and size of the inhomogeneity placed in homogenous circle) in [23]. Authors used forward solver based on FDTD. Numerical model consisted of 8 ports in circle. Tikhonov and edge preserving regularization were used to deal with ill-posedness of the problem. A priori information was included in term of that dielectric properties of tissues are known, i.e. only distribution of

different tissues were estimated. The system was designed to work on frequencies from 1.5 GHz to 4.5 GHz. The results from numerical simulations were presented only. The particle swarm optimization was also used in [24]. The FDTD frequency dependent (including Debye model) based forward solver was used in [25]. The genetic algorithm was employed here in solving of the inverse scattering problem without any regularization. This system was designed to be broadband (1-10 GHz). The algorithm was tested for different tissues surrounding a tumour - different contrasts. The ROI was irradiated by Gaussian pulse plane wave from four different directions. The numerical phantoms with uniform and non-uniform distribution of fibro-glandular and fatty tissue were used because proportion of fatty to fibro-glandular tissue depends on the selected cross section of the breast [26]. Genetic algorithm (GA) is widely used in field of MWT and can be found in many approaches in its several modifications. GA based approach without using forward solver of EM field was used in [27] to detect flaws in unknown medium. Parallel implementation of GA and FDTD solver was also shown in [28]. The method was used to detect an objects placed in the ground. Authors are using plane wave irradiating the ground surface and sensors of E-field placed close to the ground surface. Five parameters had been estimated. Cross-section of inhomogeneous, infinite cylindrical object was reconstructed using the GA in [29]. Linearization of the inverse problem was done by second-order born approximation, which allows to deal with higher dielectric contrast in comparison with the first order born approximation. Two different genetic algorithms (BGA - binary coded and real-coded RGA) are accompanied in reconstruction of dielectric profile of phantom of human breast in [30]. These so called hybrid approaches take the advantages of both algorithms. Performance of genetic algorithm, neural networks (NN) and hybrid method composing from micro genetic algorithm and conjugate gradient based approaches are compared in [31]. The trained NN demonstrated similar results as the GA, but the computational time was reduced in case of NN. The hybrid approach had the shortest convergence time and achieved the best results for the one cylinder phantom. The approach combining genetic algorithm and neural networks (NN) is presented in [32]. The optimization procedure was driven by GA and the NN were responsible for the selection of new individuals generated by GA. Eleven different classifiers were used to distinguish between breast like and non-breast profiles. Non breast profiles are penalized – this plays a role as regularization. Differential evolution (DE) and Particle swarm optimization procedures were used to establish dielectric parameters of one dimensional inhomogeneous scatterer with known thickness in [33]. Combination of Ant colony optimization (ACO) – stochastic global optimization method and linear sampling method (LSM) – computationally efficient method was presented in [34] dealing with three dimensional scatterers. Finally, there is an effort to combine different imaging modalities with MWT. An interesting combination of MWT with MRI can be found in [35]. A priori information about tissues distribution from the MRI images can be included into reconstruction algorithm. To work with simplified numerical models as well as with anatomical realistic models of human breast is important when testing the reconstruction algorithms. The real values of dielectric properties of tissues contained in human breast need to be established together with dielectric properties of malignant breast tissue. Different amounts of two different tissues (adipose and gland) are contained in the breast. A review on this problematic can be found in [36].

1.5 Main aims of dissertation thesis

This dissertation thesis is mainly focused on contribution to new technological approaches of MWT, especially to its theory and near futures clinical applications. I decided to concentrate mostly on the quantitative deterministic iterative approaches. These approaches seem to be the one of the most promising for medical application of MWT [8].

The following 5 main aims of this dissertation thesis (focussed on new development of microwave technologies to be used for MWT) can be specified as follows:

- Design of special antenna systems for microwave tomography (Chapter 3, 5 and 9)
- Complex permittivity measurement of human tissues (Chapter 6)
- Study of reconstruction algorithms for microwave tomography and its implementation (Chapter 2, 7 and 8)
- Development of a system for brain stroke detection and classification (Chapter 2, 4 and 9)
- Development of temperature dependent model of dielectric properties of an agar phantom for testing of a system combining MHTS and MWT (Chapter 5)

1.6 Description/Overview of dissertation thesis

For better orientation in submitted dissertation thesis and for better understanding of its results its content will be described in following text. This dissertation thesis is arranged into 10 chapters. The work described here comes out from main research projects in which the author was involved. (list is given at the end of the Chapter 10).

Chapter 1: “Microwave Imaging: State of the Art”, brings a description of the state of the art in the area of medical applications of microwaves and specification of main aims of this dissertation thesis.

Chapter 2: “Image reconstruction algorithm: Iterative algorithm with Gauss Newton optimization” describes the basics and implementation of the imaging algorithm implemented in the frame of this dissertation.

Chapter 3: “Antennas elements for microwave tomography”. In the first part of this chapter four different antennas are compared with respect to its suitability for use in microwave tomography system. Aim of this work is to recommend an antenna element for the next generation of our microwave tomography system. Several criteria are defined in this chapter and they are evaluated for every tested antenna. This comparison includes two microstrip patch antennas, wire monopole antenna and waveguide antenna. While microwave patch antennas fulfil the best most of our criteria, waveguide antenna has the most suitable radiation pattern. The waveguide antenna element was selected as the most promising antenna element due to its symmetric radiation pattern and reduced radiation outside the imaging domain. Disadvantage of this antenna element is in its difficult fabrication. The waveguide based antenna element is compared to the slotted bowtie antenna element designed, manufactured and tested in the frame of this work. This antenna element shows similar properties in terms of radiation symmetry and limited radiation outside the imaged domain, includes symmetrization circuit and is easily manufactured with standard PCBs with high manufacturing reproducibility.

Chapter 4: “Laboratory microwave imaging system for detection and classification of strokes”. In this chapter, a prototype of a microwave imaging system for brain stroke detection and differentiation (developed at the Faculty of Biomedical Engineering of the Czech Technical University in Prague) on phantoms is presented. The prototype consists of a measuring container with eight bowtie antennas, a vector network analyser and a PC with appropriate software. The 3D printed measuring container was filled with liquid phantom of human brain grey matter. Two different phantoms of brain stroke were prepared (haemorrhagic and necrotic) and moved over 25 different positions in measuring container and thereby covering almost all possible areas in the brain phantom. The Gauss-Newton iterative reconstruction algorithm incorporating computation of EM field in 3D numerical model in every iteration and adjoint

method of computation of Jacobian was implemented and applied to measured S-parameters. Approximate position of strokes of both types can be observed from reconstructed images of conductivity based on synthetic as well as measured data even after first iteration of the algorithm. Since EM field for homogeneously filled measuring container can be computed in advance for the first iteration, the results can be obtained in couple of seconds. Furthermore, a tendency to rise or decrease in conductivity in the region of stroke can also be observed from these images, which is crucial information for differentiation of the strokes.

Chapter 5: “Temperature Dependent Complex Permittivity Model of Agar Phantom for Microwave Temperature Distribution Monitoring During Microwave Hyperthermia Treatment”. It is well known fact, that the dielectric parameters of materials are not only frequency but also temperature dependent. This fact leads to the idea of using MWT for noninvasive monitoring of the temperature in human body during cancer treatment procedure called microwave hyperthermia. To allow testing of a MWT prototypes for this purpose, tissue simulating materials with known temperature dependency of its dielectric properties are needed. From that reason complex permittivity of agar phantom material was measured and the parameter of temperature dependent model were estimated in this chapter. As the changes in complex permittivity due to a temperature change are very low, high precision and error free measurement is crucial and so our experiences with measurement with open ended coaxial probe at University of Galway, Ireland are described in chapter 6.

Chapter 6: “Dielectric Measurement of Biological Tissues: Challenges and Common Practices” is based on paper published in *Diagnostics* 2018, 8, 40; (doi: 10.3390/diagnostics8020040). It is stated here that EM medical technologies are expanding for both diagnostics and therapy. As these technologies are low-cost and minimally invasive, they have been the focus of significant research efforts in recent years. Such technologies are often based on the assumption that there is a contrast in the dielectric properties of different tissue types or that the properties of particular tissues fall within a defined range. Thus, accurate knowledge of the dielectric properties of biological tissues is fundamental to EM medical technologies. Over the past decades, numerous studies were conducted to expand the dielectric repository of biological tissues. However, dielectric data is not yet available for every tissue type and at every temperature and frequency. For this reason, dielectric measurements sometimes may be performed by researchers who are not specialists in the acquisition of tissue dielectric properties. To this end, this paper reviews the tissue dielectric measurement process performed with an open-ended coaxial probe. Given the high number of factors, including equipment- and tissue-related confounders, that can increase the measurement uncertainty or introduce errors into the tissue dielectric data, this work discusses each step of the coaxial probe measurement procedure, highlighting common practices, challenges, and techniques for controlling and compensating for confounders.

Chapter 7: “Real-time brain stroke detection through a learning-by-examples technique—An experimental assessment” is based on paper published in *Microw Opt Technol Lett.* 2017; 59: 2796–2799 (doi: 10.1002/mop.30821). The real-time detection of brain strokes is addressed within the Learning-by-Examples (LBE) framework. Starting from scattering measurements at microwave regime, a support vector machine (SVM) is exploited to build a robust decision function able to infer in real-time whether a stroke is present or not in the patient head. The proposed approach is validated in a laboratory-controlled environment by considering experimental measurements for both training and testing SVM phases. The obtained results

prove that a very high detection accuracy can be yielded even though using a limited amount of training data.

Chapter 8: “Instantaneous Brain Stroke Classification and Localization from Real Scattering Data”. is based on paper published in *Microwave and Optical Technological Letters*. 2019; 61: 805–808. (doi: 10.1002/mop.31639). This chapter presents a 2-step Learning-by-Examples approach for the real-time classification of hemorrhagic/ ischemic brain strokes and their successive localization from microwave scattering data collected around the human head. An experimental assessment against laboratory-controlled data is performed to assess the potentialities of the proposed approach towards a reliable monitoring and instantaneous diagnosis clinic protocol.

Chapter 9: “Microwave Tomography System for Methodical Testing of Human Brain Stroke Detection Approaches” is based on paper published in *International Journal of Antennas and Propagation*, Volume 2019, Article ID 4074862, 9 pages, (doi: 10.1155/2019/4074862). In this chapter, a prototype of a laboratory microwave imaging system suitable to methodically test the ability to image, detect, and classify human brain strokes using microwave technology is presented. It consists of an antenna array holder equipped with ten newly developed slot bowtie antennas, a 2.5 D reconfigurable and replaceable human head phantom, stroke phantoms, and related measuring technology and software. This prototype was designed to allow measurement of a complete S-matrix of the antenna array. The reconfigurable and replaceable phantom has currently 23 different predefined positions for stroke phantom placement. This setting allows repeated measurements for the stroke phantoms of different types, sizes/shapes, and at different positions. It is therefore suitable for large-scale measurements with high variability of measured data for stroke detection and classification based on machine learning methods. To verify the functionality of the measuring system, S-parameters were measured for a hemorrhagic phantom sequentially placed on 23 different positions and distributions of dielectric parameters were reconstructed using the Gauss-Newton iterative reconstruction algorithm. The results correlate well with the actual position of the stroke phantom and its type.

Chapter 10: “Thesis Conclusion” brings a summary of the dissertation thesis.

Chapter 11: “Publications of the author” overviews author’s own publications and his scientific activities.

2. Image Reconstruction Algorithm: Iterative algorithm with Gauss Newton optimization

In our Bio-Electromagnetics research laboratory, different existing algorithms, such as Stochastic reconstruction algorithm based on Genetic algorithm, Deterministic algorithms based on Born and distorted Born approximation were implemented and tested. This chapter is devoted to description of a deterministic iterative algorithm based on Gauss Newton optimization which is considered to be well suitable for different microwave diagnostic applications and which was implemented and tested in the frame of this dissertation thesis.

2.1 General definitions

2.1.1 Basic concepts - EM field

A common base for all the reconstruction algorithms is defined in this section. We can start with local form of Maxwell's equations for time harmonic field [19]:

$$\nabla \times \mathbf{E}(\mathbf{r}) = -j\omega\mathbf{B}(\mathbf{r}) \quad (1)$$

$$\nabla \times \mathbf{H}(\mathbf{r}) = j\omega\mathbf{D}(\mathbf{r}) + \mathbf{J}(\mathbf{r}) \quad (1)$$

$$\nabla \cdot \mathbf{H}(\mathbf{r}) = \rho(\mathbf{r}) \quad (2)$$

$$\nabla \cdot \mathbf{B}(\mathbf{r}) = 0 \quad (3)$$

Here, \mathbf{r} denotes the position vector in meters, \mathbf{E} , \mathbf{H} , \mathbf{D} , and \mathbf{B} , are complex vector fields describing the electromagnetic field, more specifically: electric field (V/m), the magnetic field (A/m), the electric flux density (C/m²) and the magnetic flux density (Wb/m²). Further ρ and \mathbf{J} denotes the sources and represents volume electric charge density (C/m³) and electric current density (A/m²). ω is the angular frequency.

Moreover, constitutive equations specific for the medium where the propagation of the field takes place are provided to make the solution of the Maxwell's equations unique. For most of the materials (including all human tissues) hold following constitutive equations:

$$\mathbf{D}(\mathbf{r}) = \bar{\epsilon}\mathbf{E}(\mathbf{r}) \quad (4)$$

$$\mathbf{B}(\mathbf{r}) = \bar{\mu}\mathbf{H}(\mathbf{r}) \quad (5)$$

Where $\bar{\epsilon}$ and $\bar{\mu}$ are dielectric permittivity (F/m) and magnetic permeability tensors (H/m). The isotropic materials are characterized by following equations:

$$\bar{\epsilon} = \epsilon(\mathbf{r})\bar{\mathbf{I}} \quad (6)$$

$$\bar{\mu} = \mu(\mathbf{r})\bar{\mathbf{I}} \quad (7)$$

Where $\bar{\mathbf{I}}$ is the identity tensor and ϵ and μ scalar functions, respectively dielectric permittivity and magnetic permeability. Dielectric permittivity and magnetic permeability are often defined relatively to permittivity and permeability of vacuum ($\epsilon_0 \approx 8.85 \times 10^{-12}$ F/m, $\mu_0 \approx 4\pi \times 10^{-7}$ H/m) as follows:

$$\epsilon_r(\mathbf{r}) = \frac{\epsilon(\mathbf{r})}{\epsilon_0} \quad (8)$$

$$\mu_r(\mathbf{r}) = \frac{\mu(\mathbf{r})}{\mu_0} \quad (9)$$

For conductive materials also holds following equation:

$$\mathbf{J}_i(\mathbf{r}) = \sigma(\mathbf{r})\mathbf{E}(\mathbf{r}) \quad (10)$$

Where \mathbf{J}_i corresponds to induced current by the field and σ is electric conductivity of the material. Effective dielectric conductivity (complex valued dielectric permittivity) can be then introduced as:

$$\varepsilon(\mathbf{r}) = \varepsilon_0 \left(\varepsilon_r(\mathbf{r}) - j \frac{\sigma(\mathbf{r})}{\omega \varepsilon_0} \right) = \varepsilon_0 (\varepsilon_r'(\mathbf{r}) - j \varepsilon_r''(\mathbf{r})) \quad (11)$$

The purpose of the dielectric image reconstruction algorithms is to retrieve the complex dielectric permittivity $\varepsilon(\mathbf{r})$.

2.1.2 Placement of an object into the propagation/background medium

The propagation of electromagnetic field is influenced by inclusion of a scatterer. This is an object with different dielectric parameters of the surrounding medium. In this case the total (perturbed) electric field (\mathbf{E}_{tot}) is composed from incident unperturbed (\mathbf{E}_{inc}) field and scattered field (\mathbf{E}_{scat}):

$$\mathbf{E}_{\text{tot}}(\mathbf{r}) = \mathbf{E}_{\text{inc}}(\mathbf{r}) + \mathbf{E}_{\text{scat}}(\mathbf{r}). \quad (12)$$

If the object and the configuration are known, then the total field can be calculated. This procedure is called as direct scattering problem. If the object is unknown and its parameters must be deduced from the measurement of the total field, the problem is called inverse scattering problem. Since we only can measure the total field \mathbf{E}_{tot} , the relation between the measurements of the \mathbf{E}_{tot} field and the properties of the scatterer must be deduced. This can be done by using volume equivalence principle, which shows that the \mathbf{E}_{scat} produced by the scattering of the field by real object can also be produced by equivalent sources radiating in free space. Those sources are dependent on the object properties and total internal field. The scattered electric field can then be expressed in integral form as [19]:

$$\mathbf{E}_{\text{scat}}(\mathbf{r}) = j\omega\mu_b \int_{V_0} \mathbf{J}_{\text{eq}}(\mathbf{r}') \bar{\mathbf{G}}(\mathbf{r}/\mathbf{r}') d\mathbf{r}' + \int_{V_0} \nabla \times \mathbf{M}_{\text{eq}}(\mathbf{r}') \bar{\mathbf{G}}(\mathbf{r}/\mathbf{r}') d\mathbf{r}', \quad (13)$$

where $\mathbf{J}_{\text{eq}}(\mathbf{r}) = j\omega[\varepsilon(\mathbf{r}) - \varepsilon_b]\mathbf{E}_{\text{tot}}(\mathbf{r})$ and $\mathbf{M}_{\text{eq}} = j\omega[\mu(\mathbf{r}) - \mu_b]\mathbf{H}_{\text{tot}}(\mathbf{r})$ represent the equivalent sources, $\bar{\mathbf{G}}$ is the free-space Green dyadic tensor [37], ε_b and μ_b background permittivity and permeability and V_0 volume of the scatterer. \mathbf{r}' is a vector describing the position of the sources. If only nonmagnetic objects are considered and so $\mathbf{M}_{\text{eq}} = 0$, equation (13) simplifies and by using the equation (12) one can obtain:

$$\mathbf{E}_{\text{tot}}(\mathbf{r}) = \mathbf{E}_{\text{inc}}(\mathbf{r}) + j\omega\mu_b \int_{V_0} j\omega[\varepsilon(\mathbf{r}') - \varepsilon_b]\mathbf{E}_{\text{tot}}(\mathbf{r}') \bar{\mathbf{G}}(\mathbf{r}/\mathbf{r}') d\mathbf{r}' \quad (14)$$

which is Fredholm linear integral equation of the second kind [38]. Since $\mathbf{E}_{\text{tot}}(\mathbf{r})$ is going to be measured only outside of the V_0 and $\mathbf{E}_{\text{tot}}(\mathbf{r})$ together with $\varepsilon(\mathbf{r})$ are unknown quantities in the volume of the object V_0 , the equation (14) turns out to be nonlinear [39].

To retrieve information of distribution of dielectric parameters inside of the region of interest from measured data at specific points, inverse scattering problem must be solved.

Inverse problems are commonly ill-posed, that make them very difficult to solve [19]. It means that at least one of those three conditions is not satisfied (ref. Hadamard 1923):

- The solution exists.
- The solution is unique (the specific set of data corresponds to the one solution).
- The solution is stable (the solution depends continuously on the data).

To control the ill-posedness of the inverse problems, regularization procedures are involved in the solutions. Those tools act by replacing of the original problem by well-posed by utilizing some additional information (a priori information). However, only approximate solution of the original problem can be expected in such a case [19].

2.2 Description of iterative algorithm with Gauss Newton optimization

Modified version of iterative reconstruction algorithm based on Gauss Newton algorithm with Tikhonov regularization [40] is described here. This algorithm is based on deterministic optimization procedure, assuming linear behaviour of outcome in every iteration when only small change in dielectric parameters is introduced. Property update (error in an object function, ΔO_k) can be calculated in every iteration according to this matrix equation [40]:

$$\Delta O_k = (J^*J + \lambda I)^{-1} J^* \Delta S_k \quad (16)$$

where J is a Jacobian matrix consisting of derivatives of the electric field with respect to the dielectric properties at every location. ΔS_k is the difference between numerically calculated and measured scattered field. The asterisk denotes the conjugate transpose here. The term λI incorporates standard Tikhonov regularization with I equaled to identity matrix and λ given by [40]:

$$\lambda = \alpha \frac{1}{N} \sum_{i=1}^N J^* J(i, i) \text{err} S^2 \quad (17)$$

Value of parameter α is determined empirically and $\text{err} S^2$ is relative mean square error of the scattered field. Value of dielectric properties at each iteration (update) can be obtained as:

$$O_{k+1} = O_k + \Delta O_k \quad (18)$$

The elements of Jacobian matrix J can be expressed as [41]:

$$J(s, r, p) = \left\langle \frac{\partial E_s}{\partial O_p}, \delta(x_r, y_r) \right\rangle \quad (19)$$

where E_s is electric field from radiation source at location s , O_p are dielectric properties at location p and r corresponds to a position of affected antenna. \langle, \rangle has a meaning of inner product of the two terms here. Computation of all the elements of Jacobian matrix one by one is computationally very intensive procedure because it requires one forward solver run (computation of EM field) per one element of the matrix. Especially when the number of estimated parameters is high, this part takes most of the computational time for the whole reconstruction. From this reason it was decided to apply so-called adjoint method of computation of Jacobian, which enables significant reduction of runs of forward solver in building process of the Jacobian matrix. By using the adjoint method, the elements of Jacobian matrix can be computed according to this equation [41]:

$$J(s, r, p) = - \left\langle \frac{\varphi_p}{j\omega\mu_0 |J_r|} E_s, E_r \right\rangle \quad (20)$$

Where φ_p is a region of parameter O_p , μ_0 is permeability of vacuum, ω is angular frequency, J_r is source current induced at the receiver at the position r and E_r is electrical field due to the auxiliary source at receiver position r . It can be deduced, that using this method, the whole row of the Jacobian matrix is calculated in only one run of the forward solver and so the dependency of computational time on the number of estimated parameters is minimized.

2.2.1 Image reconstruction procedure

The spatial distribution of dielectric properties is reconstructed iteratively involving 5 main steps at every iteration as depicted in Figure 2.1. The reconstruction procedure starts with an assumption that the dielectric properties are the same in the entire region of interest. Thanks to that all E fields, S parameter matrix and also Jacobian can be precomputed for the first iteration. First iteration of the reconstruction procedure is quick (takes less than 1 s), because the most computationally intense step can be avoided and step in dielectric parameters can be directly calculated. The second iteration starts by the run of the forward solver with updated object function for every single antenna port. The algorithm was tested using numerical model of MWT system for human head imaging describe in Chapter 9. On the current PC (i7-6700 - 3.4 GHz, 64 GB RAM - 2133 MHz) the computation of the forward problem takes about 45 minutes for all antenna ports (10) and single frequency. S parameter matrix together with E fields are exported in the next step. E-field is exported in 2 mm regular grid. This resolution sufficiently approximates the shape of included inhomogeneity and at the same time keeps the computational cost of Jacobian and property update on reasonable level. Finally, the Jacobian matrix is calculated from the E-fields. The last procedure involves computation of property update in all the locations. The iterative procedure continues by the next iteration until the error between the measured and computed scattered field is lower than specified value or after maximum amount of iterations was reached. The reconstruction algorithm was implemented in MATLAB programming environment. COMSOL Multiphysics and its Radiofrequency (RF) module was used to create numerical model of the system and to compute all the numerical simulations of electromagnetic field. Communication of COMSOL with MATLAB was ensured by LiveLink for MATLAB.

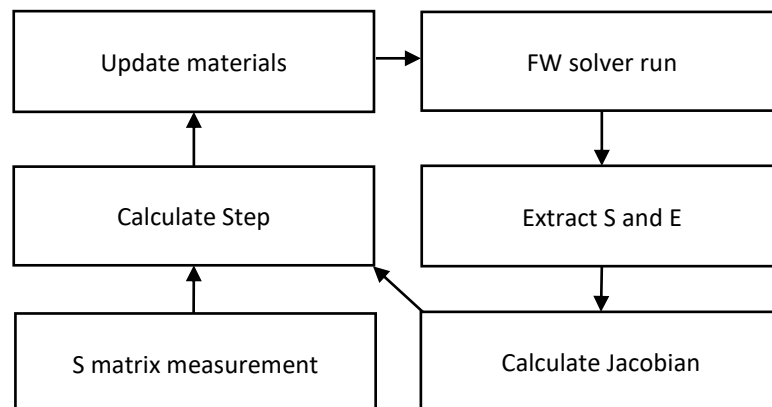


Figure 2.1, Flowchart of reconstruction procedure – one iteration.

3. Antenna Elements for Microwave Tomography

Aim of this chapter is to recommend an antenna element for the next generation of our microwave tomography system. At the beginning of this chapter, four different antennas are compared with respect to its suitability for use in microwave tomography system. Several criteria are defined in this chapter and those are evaluated for every tested antenna. These include two microstrip patch antennas, wire monopole antenna and waveguide antenna. While microwave patch antennas fulfil the best most of our criteria, waveguide antenna has the most suitable radiation pattern. As the symmetry of the radiation pattern is considered important, in the framework of this thesis, a novel planar antenna element, namely slot bowtie antenna, was designed and compared with the waveguide-based antenna element. Both antenna elements show similar properties in terms of radiation symmetry and limited radiation outside the imaged domain. The slot bowtie antenna element can be manufactured with high accuracy and low cost using standard PCB technology. This slot bowtie antenna was manufactured and tested.

3.1 Comparison of four different antenna elements

The aim of this section is to give an advice for the most suitable antenna for microwave tomography system that is under constant development at Faculty of Biomedical Engineering, CTU in Prague. This system can estimate dielectric properties in a specific region of human body. Proper antenna selection and its design is one of the crucial parts of every MWT imaging system. Firstly, parameters of an ideal antenna are defined, secondly four antennas are selected and numerically tested to evaluate which antenna meets our criteria the best. Many antennas for MWT has been developed and a few of them also used for measurement in real MWT systems. Well tested prototype for imaging of human breast in [43] can be a perfect example of using monopole wire antennas. Microwave tomography system with microstrip patch antennas with grounding plane used for different temperature monitoring can be found in [44]. And finally waveguide antennas with ceramic filling were implemented and tested with imaging of bovine leg in [45].

3.1.1 Criteria for evaluation of the antennas

The criteria listed here are selected based on our experiences with previously used antenna in the MWT system. The newly selected antenna should be less sensitive to a noise from the surroundings. This could be achieved by using an antenna with grounding plane. We are also looking for antenna, which can be fed symmetrically without need of use of any balancing circuit. Symmetric radiation pattern is also highly appreciated. The antennas must be small enough to fit next to each other on a circle with radius of 16 cm (diameter of the imaging cavity). The perfect antenna will also have the lowest absolute value of S_{11} and the highest possible transmission between the most distant antennas. When compared with radar based microwave imaging systems, bandwidth of the antennas is not as important for MWT. Finally a sensitivity of the antenna to a change in dielectric parameters inside of the imaging cavity will also be tested.

3.1.2 Selected antennas and evaluation scenario

Four different antennas were selected and evaluated (Figure 3.1). Microstrip patch antenna with cut out sides (I.), microstrip folded patch antenna (II.), waveguide antenna (III.), and coaxial monopole wire antenna (IV.). Sixteen antennas of every kind were placed on the walls of hexagonal cavity (described later) filled with matching liquid. In the cavity the antennas were matched to meet the first criterion, i.e. achieve the lowest absolute value of S_{11} (lower than -12 dB in any case). During this procedure, dimensions and shapes of antennas and positions of its

feeding ports were numerically optimized to achieve this goal. Antennas based on dielectric substrate were designed on Rogers RO4003C with thickness of 1.524 mm and following dielectric parameters: $\epsilon_r = 3.55$, $\sigma = 0.002$ S/m. The measuring container was designed to have hexagonal shape and was filled with matching liquid with relative permittivity $\epsilon_r = 45$ and conductivity $\sigma = 0.8$ S/m. There is only one exception. When the waveguide antenna was evaluated, relative permittivity of the liquid had to be increased to 50 to fulfil the requirement on the reflection coefficient (waveguide antenna dimensions were defined by standard WR-90). Inner radius of the container equals to 80 mm and it has height of 200 mm. When monopole wire antenna was tested, the radius of the container was increased to 100 mm to maintain the same distance between antennas (exposed bended parts of this antennas are on the circle with radius of 80 mm). Peripheral and bottom wall of the container was defined as perfect electric conductor.

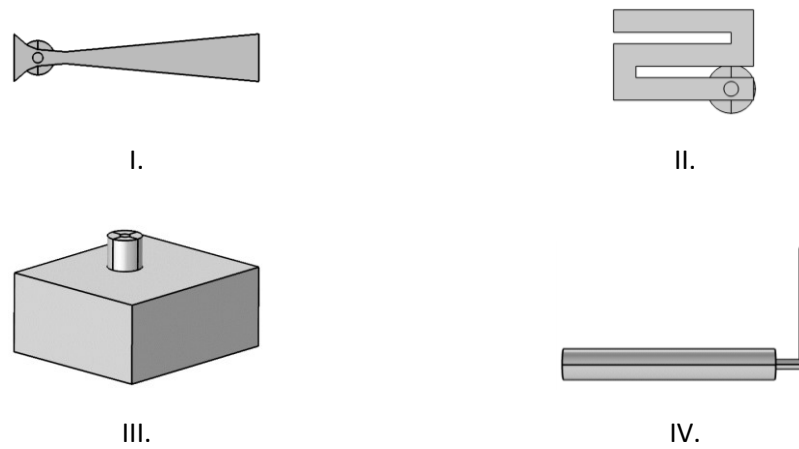


Figure 3.1, Compared antennas - Microstrip patch antenna with cut out sides (I.), microstrip folded patch antenna (II.), waveguide antenna (III.) and coaxial monopole wire antenna (IV.).

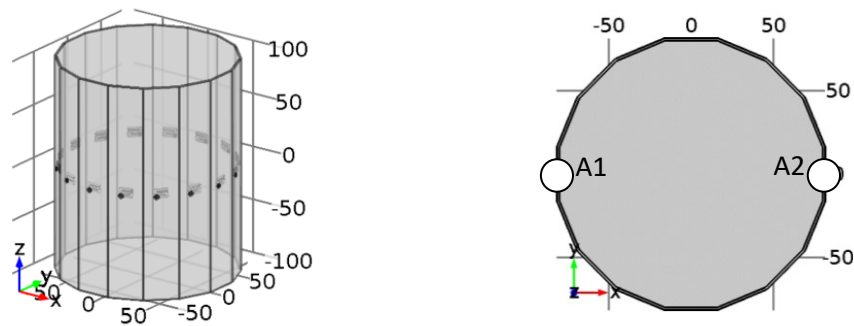


Figure 3.2, Measuring container and positions of active antennas (A1 and A2).

3.1.3 Numerical simulations

Antennas were fed by coaxial connector (dimensions of SMA) with coaxial port. Central working frequency of the MWT system was established to 1 GHz with a bandwidth of 400 MHz. The antennas were tested in this frequency range with frequency step of 20 MHz. Comsol Multiphysics and RF module was used to numerically model the antennas and to calculate the electromagnetic field. Although all sixteen antennas were placed on the wall of the container, only two most distant antennas were active – antenna A1 and A2 in Figure 3.2.

3.1.4 Results

Evaluation of results can be described in 3 following steps:

- Simulation and measurement of S_{11} and S_{21} parameters for tested antennas.
- Simulation and measurement of radiation pattern.
- Sensitivity to a change in dielectric properties.

These are described in more details in the following text.

First of all, S_{11} and S_{21} parameters were evaluated. Amplitude of S_{11} and S_{21} can be seen in Figure 3.3 and Table 3.1. The lowest value of S_{11} at 1 GHz was achieved for microstrip folded patch antenna (II.), followed by microstrip patch antenna with cut out sides (I.). We were not able to achieve lower value of S_{11} than -12.5 dB for waveguide and monopole wire antenna. Frequency dependent S_{11} traces for these two antennas are also the flattest – the resonant frequency peak is not as obvious and deep as in the case of remaining antennas. Reduction of sharpness of the peak is probably caused by high conductivity of matching liquid (observation during the matching procedure). Microstrip folded patch (II.) antenna has also the highest value of amplitude of S_{21} at 1 GHz. This could relate to the lowest S_{11} value at the same frequency for this antenna.

Table 3.1, Maximal sizes, reflection, transmission and bandwidth of compared antennas

Antenna number	Max x size (mm)	Max y size (mm)	$ S_{11}(1 \text{ GHz}) $ (dB)	$ S_{21}(1 \text{ GHz}) $ (dB)	BW (-12 dB) (GHz)
I.	6.0	31.0	-14.8	-72.2	0.94-1.14
II.	12.5	8.0	-17.0	-65.0	0.94-1.10
III.	22.9	10.2	-13.0	-68.0	0.94-1.06
IV.	28.0	1.5	-12.2	-70.6	0.96-1.02

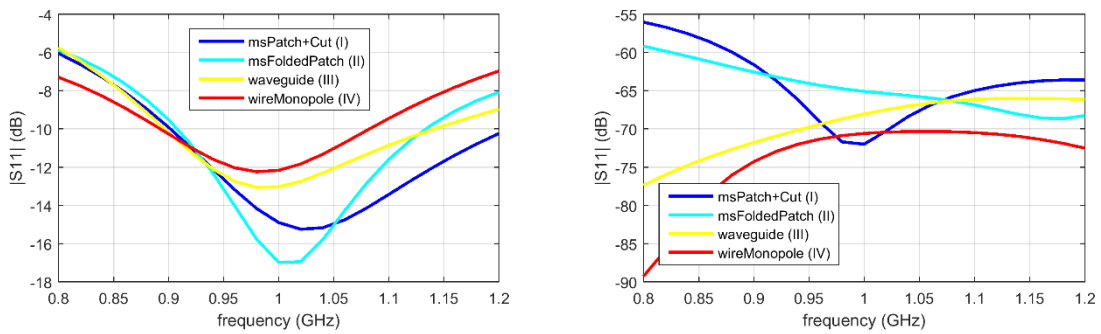


Figure 3.3, $|S_{11}|$ and $|S_{21}|$ parameters for tested antennas.

In the next step we observed contours of electromagnetic power loss densities inside of the container with matching liquid. The contours of this quantity should represent the shape of radiation pattern of antennas inside of the container in near field region of antennas. In order to compare radiation patterns for different antennas, a threshold value was established as 1/1000 of maximal value of power loss density in front of the waveguide antenna (this antenna has the most symmetric radiation pattern). There are three things to be observed in the diagrams: shape, symmetry and covered area. It can be observed, that all the evaluated antennas have very symmetric radiation pattern in XY plane. Most of the energy on the middle axes of the antennas is radiated by waveguide and wire monopole antennas, in opposite to

microstrip patch antennas, where side lobes can be observed. The largest area is covered by radiation pattern of microstrip antenna with cut of sides (I.). The smallest area is covered by radiation pattern of coaxial wire antenna. Folded microstrip patch antenna (II.) has the least symmetrical pattern in XZ plane, but almost the same asymmetry can also be observed in microstrip patch antenna with cut out sides (I.). All the patterns in XY and XZ planes are depicted in Figure 3.4.

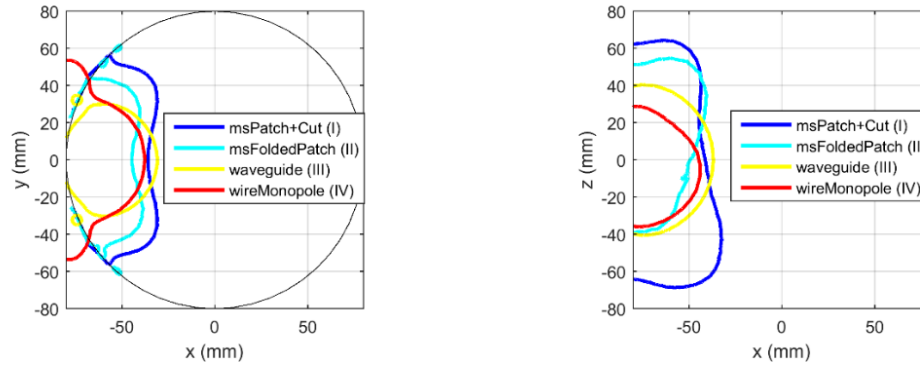


Figure 3.4, Comparison of isolines of electromagnetic power loss density for every antenna in x-y plane (1 GHz) in linear scale. All the isolines mark the same value. Black circle marks edge of the measuring container.

And finally, in this section we observed how does a change in dielectric parameters of an object placed in the matching liquid influences S parameters at the ports of the antennas. This study should reveal a sensitivity of the antennas to absolute change in dielectric parameters. The bigger the change is in S parameters, the more suitable is the antenna for MWT. For the purpose of this test, a cylinder with a radius of 40 mm was inserted in the middle of the measuring container representing some homogeneous object under the test. In the first step, relative permittivity was increased by 5 units, from 45 to 50 and conductivity kept the same (0.8 S/m) in both matching liquid in container and inserted cylinder. In the second step, conductivity was increased by 0.2 S/m to 1.0 S/m and relative permittivity kept the same (45). Absolute changes in absolute value and angle of S_{11} and S_{21} parameters were observed and are depicted in Figure 3.5. Firstly, change in relative permittivity causes almost the same change in S_{11} parameters as the change in conductivity. This can be caused by the fact, that the reflected wave travels from the interface through the same medium and is not affected as much as electromagnetic wave which goes through the inhomogeneity (the changes in angle are also very small – less than 1°). Microstrip patch antennas S_{11} are the most sensitive to a change in both relative permittivity and conductivity while amplitude and angle of S_{11} remain almost unchanged with waveguide and monopole wire antennas. Following statements can be said about the antennas and its sensitivity to the change in dielectric parameters of the inhomogeneity:

- Waveguide antenna is only sensitive to a change in conductivity in angle and amplitude of S_{21} . In other words, the biggest response in S_{21} (angle + amplitude) to a change in conductivity can be observed for waveguide antenna.
- Microstrip patch antennas shows the largest overall sensitivity.
- Microstrip folded patch antenna does not show any response in amplitude of S_{11} .
- Wire monopole antenna is resistant to changes in dielectric properties of material in amplitude of S_{11} .
- The most sensitive antenna in S_{11} (angle + amplitude) is microstrip folded patch antenna.

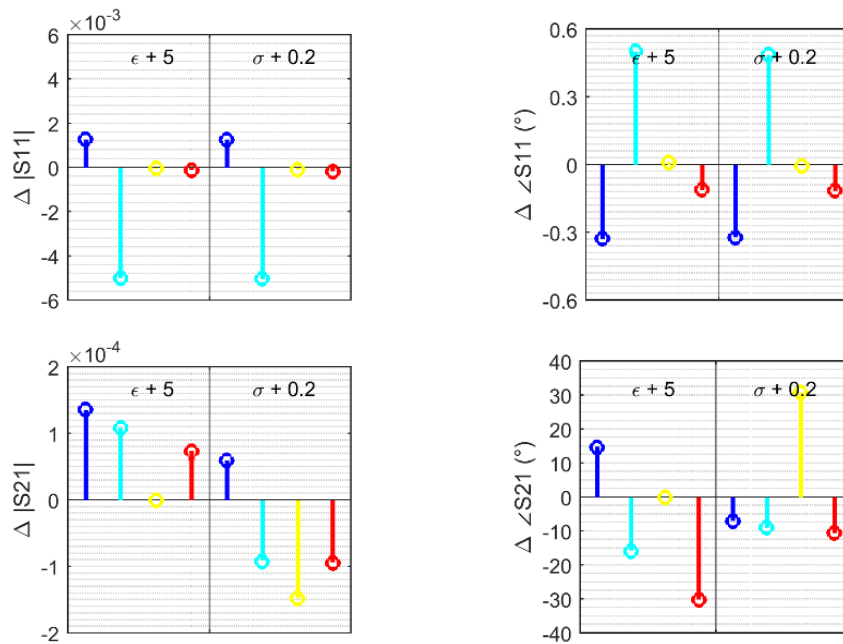


Figure 3.5, Sensitivity of S parameters to a change in dielectric properties of the phantom. Colors of the lines correspond to the antennas (same like in previous figures).

3.1.5 Conclusion of the antenna element comparison

Four different antennas were designed and evaluated according several above defined parameters. All antennas were designed to work well in the measuring container with outer wall made from metal. The evaluation procedure showed us, that well matched narrow band antenna could work well in MWT system, because a change in dielectric properties inside the measuring chamber has significant impact on measured S parameters. Microwave patch antenna fulfils our defined criteria the best, with an exception in radiation pattern where the waveguide antenna performed better.

3.2 Novel bowtie slot antenna for microwave imaging of strokes and its comparison to the waveguide based antenna

In this sub-chapter, two radiating elements were selected as a suitable candidates for use in the new generation of microwave imaging system developed at CTU in Prague. These elements are the antenna based on the rectangular waveguide as in the previous section and here proposed novel bowtie slot antenna. Both elements meet the criteria we have established above based on experience with the previous system: dominant radiation in the imaged domain, radiation symmetry and no need for a balun. The work deals with the verification of the fulfillment of the desired antenna properties and the mutual comparison of the two antenna elements by means of numerical simulations. Although both antenna elements exhibit the desired properties, the bowtie slot antenna exhibits lower internal losses compared to the rectangular waveguide-based antenna. This increases the magnitude of the transmission coefficients in our microwave imaging system by about 13 dB to about -74 dB (for the most distant antennas of the system) for the bowtie slot antenna (in comparison to the rectangular waveguide-based antenna). In addition, bowtie slot antenna elements were manufactured and as expected the high reproducibility of the production and thus reduced differences of the individual antenna elements was verified.

3.2.1 Desired parameters of new antenna element

The desired properties of the new antenna element were determined based on our experience from the previous prototypes and are listed in antenna elements comparison described above. Here, some additional or more discussed properties are listed.

1. Radiation of antenna elements should be symmetric and having one wide main lobe perpendicular to antenna aperture. The biological tissues are lossy materials and thus the magnitude of transmission coefficient can be of a very low value (< -70 dB). This represents high demands on technical parameters of switching matrix, in particular on isolation. Since all antenna elements are placed in a single plane an asymmetric radiation in z-direction means decrease of magnitude of transmission coefficients.
2. Antenna elements should be easy to manufacture and in a way which ensures good manufacturing reproducibility. In this regard waveguide antenna are less suitable.
3. Antenna elements should be mechanically stable (when a coaxial cable is connected to an antenna connector a torque wrench is used to ensure good electrical contact).

3.2.2 Compared antenna elements

As mentioned above there are two different antenna elements considered in this paper: rectangular waveguide-based antenna and a planar bowtie slot antenna (Figure 3.6 (a) and (b)). The dimensions of the aperture of the rectangular waveguide-based antenna is determined by the rectangular waveguide standard WR-90 (23 x 11 mm²) and in order to use this antenna at frequency of 1 GHz the antenna was virtually filled with material with relative permittivity $\epsilon_r = 50$. The equivalent conductivity σ was fixed to 0.8 S/m which is the same value of conductivity as in the MWT system. The length of the antenna element (dimension in x-direction) is 20 mm. The bowtie slot antenna element (Figure 3.6 (b) and Figure 3.7) was designed considering the dielectric substrate Rogers RO4003C with thickness of 1.524 mm and with $\epsilon_r = 3.55$ and $\sigma = 0.0004$ S/m. As mentioned above the geometry is adapted from [73]. The antenna in [73] consists of single layer substrate with bowtie slot from one side and a microstrip transmission line (MTL) from the other side. The coaxial port connected to MTL is from one of the thin sides of the substrate (perpendicular to aperture) which is not an option in our MWT system (Figure 3.8) - the coupling of the wave from the MTL to the bowtie slot is capacitive using a circular metallic patch attached at the end of the MTL. The adapted antenna uses two layers of the above-mentioned substrate. It is plated with copper from all six outer sides and thus creating a metallic cavity. Towards the imaged area there is the bowtie slot, and the SMA connector is located on the opposite side. MTL is replaced here by a triplate transmission line, which is connected to the bowtie slot using two via holes. Furthermore, the cut-off frequency of a dominant mode of the cavity lies well above the working frequency.

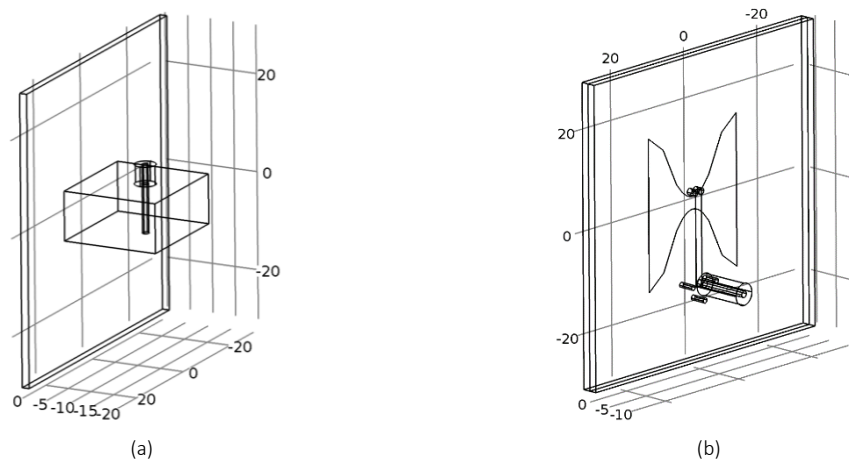


Figure 3.6, Geometries of rectangular waveguide-based (a) and bowtie slot (b) antenna elements.

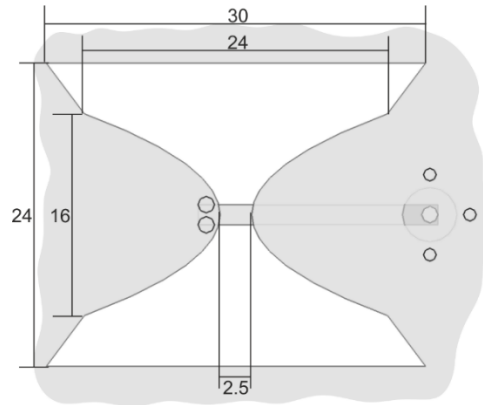


Figure 3.7, Dimensions of the bowtie slot antenna element.

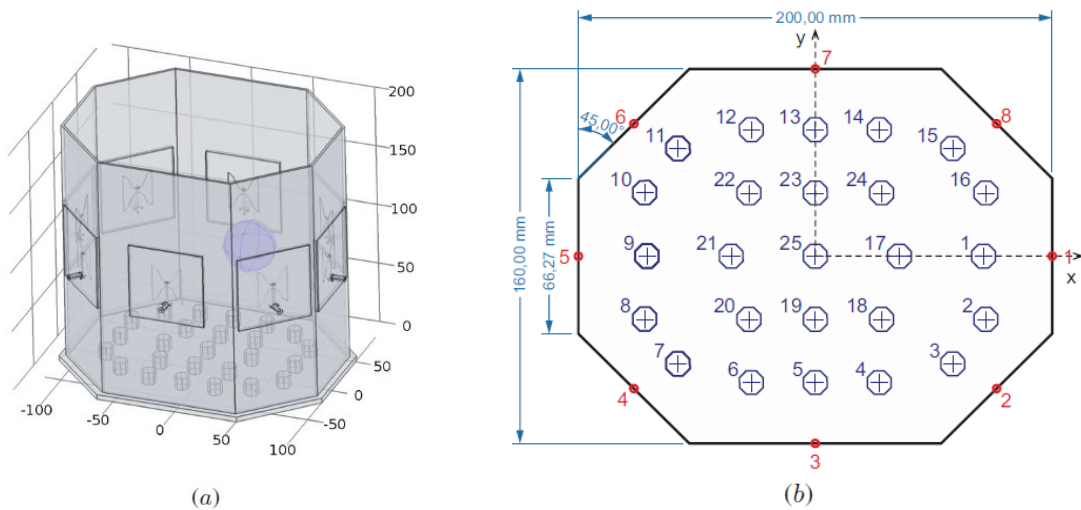


Figure 3.8, Layout of the main container for liquid head phantom. Red and blue circles represent different positions of antenna elements and different positions stroke phantoms, respectively. Height of the main container is 20 cm and the antenna plane lies in the middle of the height. (a) 3D view and (b) 2D section of the head phantom: antenna (red circles) and stroke admissible locations (blue crosses).

3.2.3 Numerical results and discussion

Numerical simulations were performed in the full-wave commercial simulation tool COMSOL Multiphysics and its RF module. First of all, a magnitude of the reflection coefficient S_{11} and of the transmission coefficient between the most distant antennas S_{51} were evaluated and are shown in Figure 3.9 (a) and (b), respectively. While the magnitude of S_{11} at 1 GHz is comparable for the two antenna elements, there are big differences in magnitude of S_{51} . The difference is about 13 dB. The differences in magnitude in all independent S-parameters at single frequency of 1 GHz is plotted in Figure 3.10. Since the same difference in the magnitude of all transmission coefficients is present it can be attributed to internal losses of the rectangular waveguide-based antenna (caused by the equivalent conductivity of the filling material). The undesired internal loss could be decreased by using some high permittivity and low loss material such as TiO_2 as it was done in [71], [72], but it would increase the production demands.

In Figure 3.11 normalized differences in transmission coefficients for the MWT system without inhomogeneity and with inhomogeneity ($\sigma = 0.6 \text{ S/m}$ and $\epsilon_r = 30$) show the system sensitivity on presence its presence. In this case the magnitudes are influenced by the presence of the spherical stroke phantom. It is clear that the system with bowtie slot antennas is more sensitive than the system using rectangular waveguide-based antennas. The symmetry in these graphs which is expected from symmetry of the simulated geometry confirms sufficiently high density of used mesh.

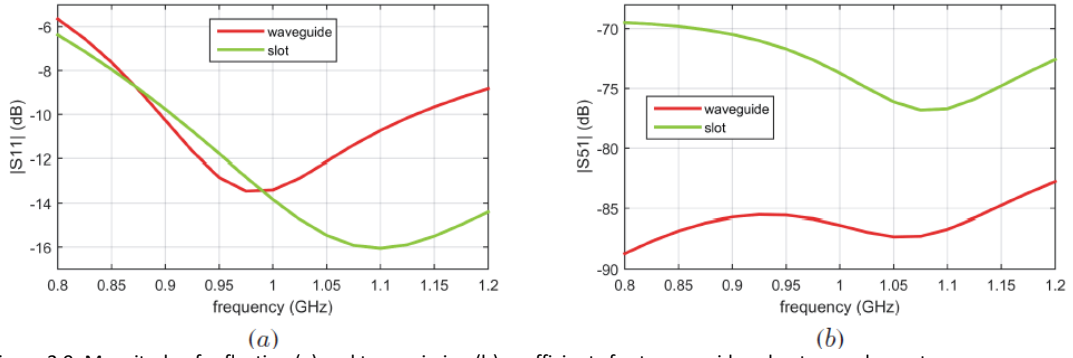


Figure 3.9, Magnitude of reflection (a) and transmission (b) coefficients for two considered antenna elements.

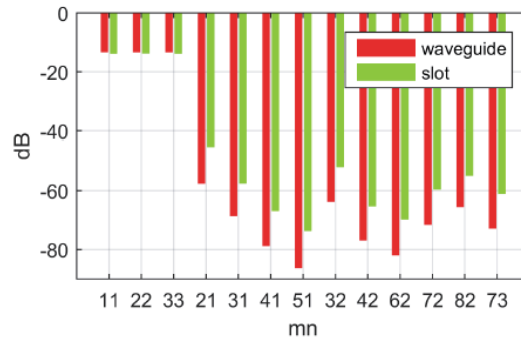


Figure 3.10, Magnitudes of all independent (due to the symmetry of the simulated geometry) S-parameters for both considered antenna elements. MN marks the antenna numbers.

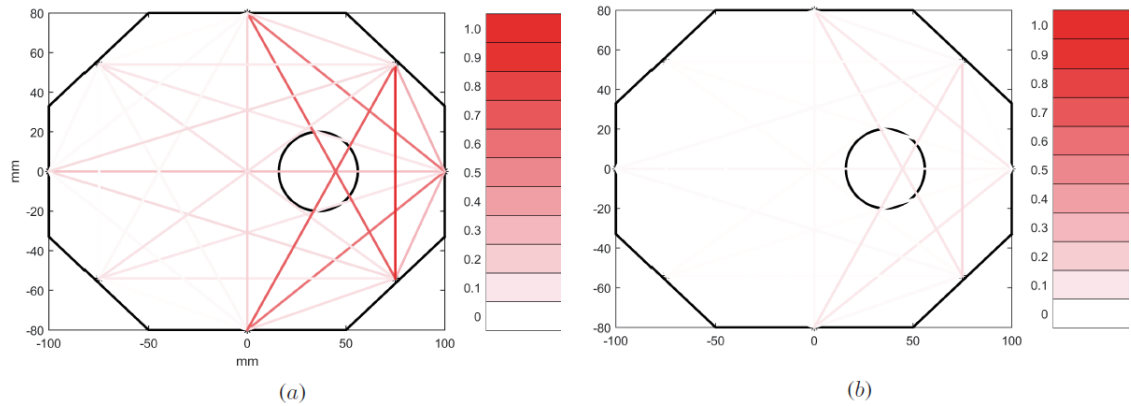


Figure 3.11, Normalized differences in transmission coefficients for the MWT system without inhomogeneity and with inhomogeneity ($\sigma = 0.6$ S/m and $\epsilon_r = 30$) - sensitivity of the system to the presence of non-homogeneity. Bowtie slot antenna (a) and rectangular waveguide-based antenna (b).

In Figure 3.12 (a) and (b) there are contours of magnitude of phasor of electric field intensity in xy - and xz - planes. This quantity should represent symmetry of radiation. The symmetry in xy -plane is expected for both antennas due to the fact that geometrically are in this plane symmetrical not only the slots/apertures of the both antennas but also the feeding circuits.

The asymmetrical feeding in the case of the bowtie slot antenna in xz -plane could have an effect on the radiation symmetry. Here the symmetry of the radiation element was studied and it has been shown that by using the two via holes (instead of one) at the end of the stripline has positive effect on the radiation symmetry. The reason for introducing the second via hole was motivated by broadening of current density in a similar way as it is broader on the grounding plane.

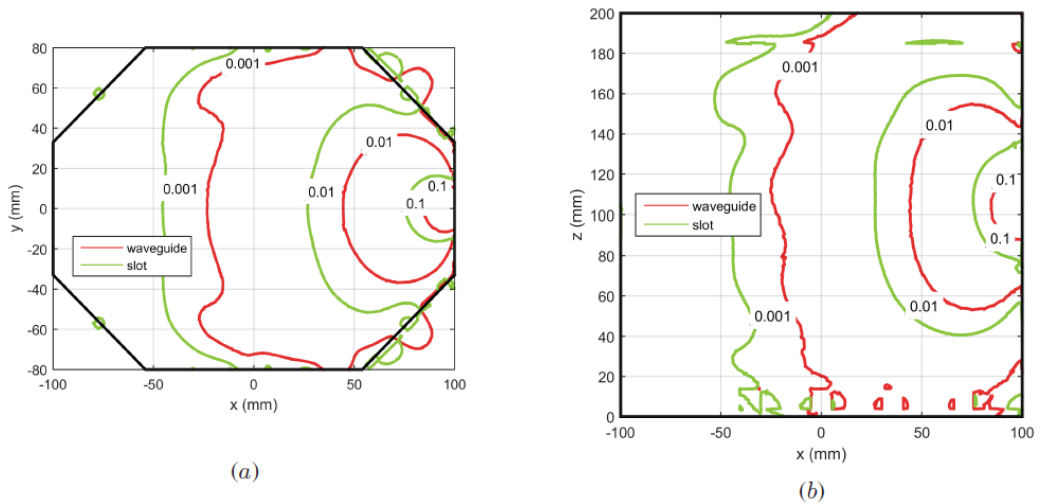


Figure 3.12, Isolines of the module of electric field intensity phasor in the planes xy (a) and xz (b). Isolines correspond to 10%, 1% and 0.1% of the maximum module of electric field intensity phasor at the aperture of the rectangular waveguide-based antenna.

3.2.4 Manufacturing reproducibility of bowtie slot antenna

The slot antenna was realized in 10 copies and their reflection coefficients were measured when attaching the antenna to a liquid medium having the average dielectric parameters of the human head. The realized antenna is shown in Figure 3.13 and the results of the measurement of the reflection coefficient confirming the high degree of reproducibility of this antenna are depicted in Figure 3.14.

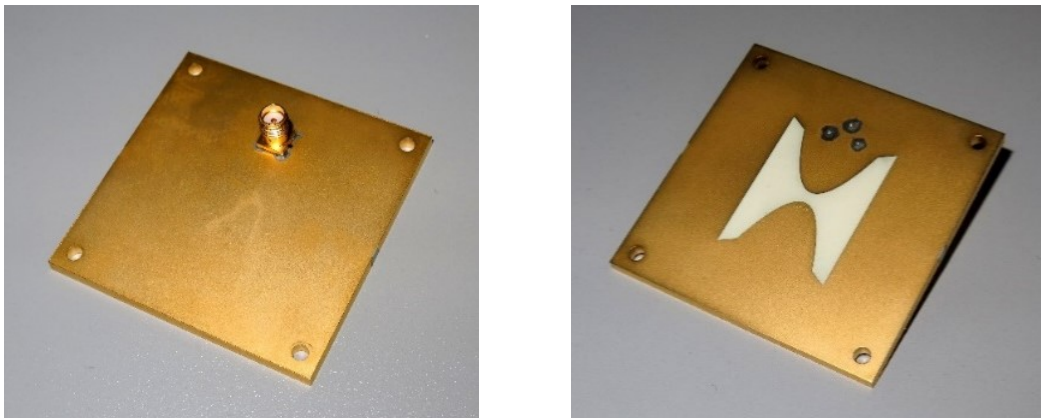


Figure 3.13, Photograph of manufactured bowtie slot antennas.

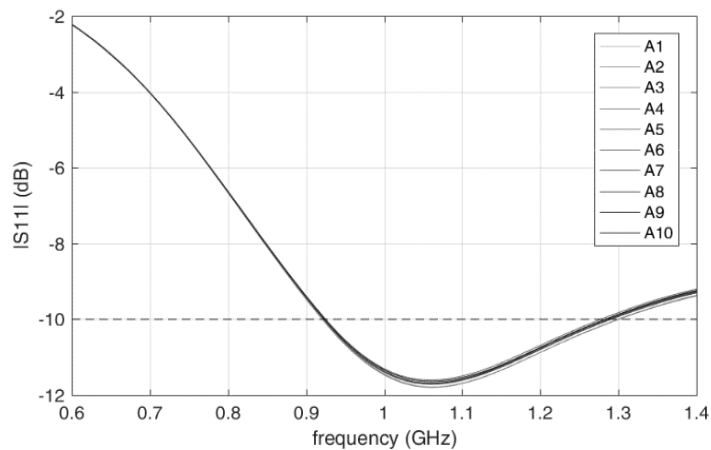


Figure 3.14., Measured reflection coefficients of manufactured bowtie slot antennas, respectively.

3.2.5 Conclusion of comparison of bowtie slot and waveguide based antenna elements

The waveguide antenna exhibits symmetrical radiation and low radiation outside of the imaged domain, and not only our group considers it the ideal radiating element for microwave imaging. However, the production of waveguide antenna is more demanding compared to planar ones. This chapter presents a bowtie slot antenna whose radiation symmetry and radiation outside the imaged domain are comparable to and lower than for waveguide based antenna, respectively. We consider the proposed antenna as a suitable alternative to the waveguide antenna. Manufacturing reproducibility was demonstrated by reflection coefficient measurements. Measurement in the MWT system with the bow-tie slot antenna numerically analyzed in above chapter is described in Chapter 9 of this work.

4. Laboratory Microwave Imaging System for Detection and Classification of Strokes

This chapter presents a prototype of a laboratory microwave imaging system for the detection and classification of strokes on phantoms, which was developed in the frame of this dissertation at the Czech Technical University in Prague. The prototype composes of a 3D printed measuring container with eight bowtie antennas, vector network analyser and a PC with appropriate software. The measuring container was filled with a liquid phantom of human brain grey matter. Two different phantoms of brain strokes were prepared (haemorrhagic and necrotic) and moved over 25 different positions in the measuring container and thereby covering almost all possible areas in the brain phantom. Gauss-Newton iterative reconstruction algorithm incorporating computation of EM field in a 3D numerical model of the imaged area in every iteration and adjoint method of computation of Jacobian was implemented and applied to measured S-parameters. Approximate position of strokes of both types can be observed from reconstructed images of distribution of conductivity based on synthetic as well as measured data even after first iteration of the algorithm. Since EM field for homogeneously filled measuring container can be computed in advance for the first iteration, those results can be obtained within few seconds. Furthermore, a tendency to rise or decrease in conductivity in the region of stroke can also be observed from these images, which is crucial information for stroke classification.

Chapters 7, 8 and 9 of this dissertation follow up on this chapter. These chapters are written on the basis of 3 articles published in scientific journals with IF. Some of the theoretical and experimental results from these articles were freely used to write this fourth chapter. Therefore, a few pictures appear repeatedly in these chapters. From the point of view of the reader's convenience and understanding of the text of individual chapters, we considered it better in this way.

The first section describes the collection of experimental data, consisting of measuring setup and procedure. The second part is devoted to the measured data analysis and achieved results.

4.1 Data acquisition

Measuring setup and measuring procedure will be described in this section.

4.1.1 Measuring setup

The measuring setup composes of the measuring container (described below), the microwave switching matrix (ZN-Z84-B42, Rhode&Schwarz, Germany), the vector network analyser (ZNB4-B32, Rhode&Schwarz, Germany) and a personal computer. Ports of the antennas placed in the container were connected to the switching matrix test ports by semi rigid coaxial cables (SMA male on both sides). Even though the isolation between all the test ports of the matrix should not be higher than -90 dB, 8 out of 24 ports of the switching matrix involved in the measurement were selected with respect to highest possible isolation between single channels, since the matrix is made of two 1x4 and four 2x6 switch modules. The fact, that the isolation of -90 dB should be sufficient, is supported by another group using custom made switching matrix with isolation of -80 dB between ports [48]. Two matrix VNA ports were connected to test ports of the VNA by the same type of coaxial cable (SMA male on the side of switch matrix, N male on the side of VNA). All high frequency connections were tightened by torque wrench to 0.9 Nm. Thanks to a selection of industrially used measuring devices, compatibility and communication of the VNA with the matrix was ensured by the manufacturer and USB cable was used to establish the physical connection. Finally, PC was connected to the VNA by Ethernet cable. After

installation of device drivers (National Instruments VISA), communication with VNA was established from Matlab (MathWorks, MA, USA). Setting and triggering of a measurement together with reading out of the data was done from this programming environment by using proper SCPI commands. Stream of the data going from the VNA is well defined and described in a manual of the VNA and can be easily segmented and converted to a form of S parameters matrix. The working frequency was decided to be 1 GHz. While keeping in mind value of isolation between the test ports of the matrix, the value of intermediate frequency bandwidth filter was established to 30 Hz. To increase signal to noise ratio, output power was set to maximal allowed value in this frequency band by the VNA manufacturer: 13 dBm. A photograph of the measuring setup together with the measuring container can be seen in Figure 4.1.

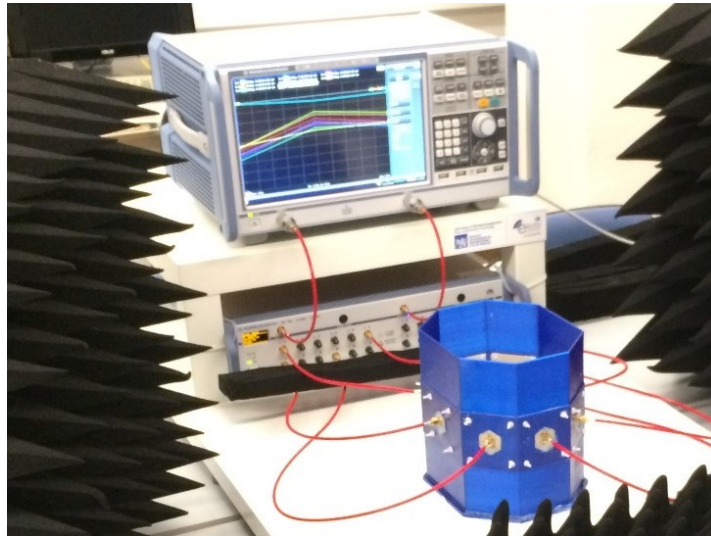


Figure 4.1, A photograph of the measuring setup.

4.1.2 Measuring container and antennas

Shape of the measuring container was mainly influenced by the imaging region and so octagonal container was chosen to be designed finally. Eight dipole bowtie antennas were placed on the walls of the container. The antennas were designed and numerically optimized in well-proven commercial numerical simulator COMSOL Multiphysics. The antenna (both arms and gap together) has overall length of 31.5 mm with 2 mm gap between the arms. Width of the arms equals to 25 mm. Rogers RO4003C material with thickness of 1.524 mm and 35 μm layer of copper was used as substrate for this antenna. The container was 3D printed in one piece from PETG material and has height of 200 mm (including the base – 4 mm) and wall thickness of 2 mm. Numerical model of proposed system is depicted in Figure 4.2. Twenty-five different positions were defined and marked on the bottom of the container (Figure 4.3). These marks have octagonal cross sections and height of 1 cm. The same inverted marks were created at the bottom of cylindrical stroke phantom holders, which were also 3D printed from the same material. These holders have inner diameter of 40 mm, height of 196 mm and wall thickness of 1 mm.

4.1.3 Calibration procedure

Calibration procedure took place before the measurement. Full port calibration was performed with the four port automatic calibration unit (ZN-Z153, Rhode&Schwarz, Germany). The VNA, the matrix and the automatic calibration unit were switched on 90 minutes prior the calibration. After initialization of the automatic full port calibration, cables going from the matrix were subsequently manually reconnected to the calibration unit according to the instructions on the

screen of the VNA - calibration of all used test ports was performed in three reconnection steps. Calibration data were saved and then reloaded before every measurement.

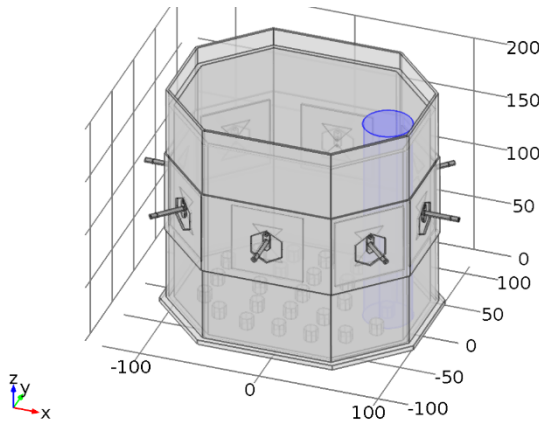


Figure 4.2, 3D model of measuring container with antennas and cylindrical sample holder – inhomogeneity.

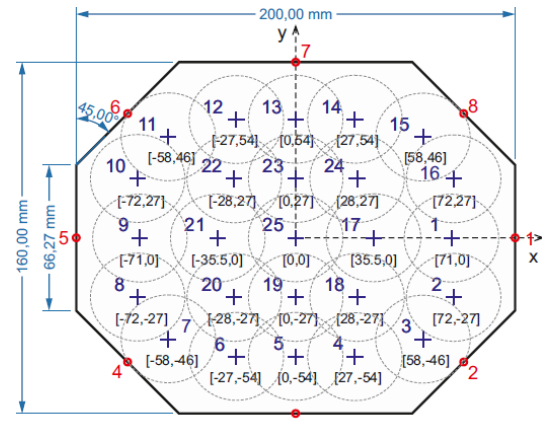


Figure 4.3, Dimensions of measuring container with marked positions of stroke phantom.

4.1.4 Liquid phantoms preparation

Three different liquid phantoms were prepared. Their dielectric properties correspond to healthy brain tissue (gray matter), necrotic brain tissue (ischemic stroke) and blood (hemorrhagic stroke). A list of all phantom components and their amounts can be found in Table 4.1. Dielectric properties of all phantoms were measured using commercial dielectric properties measurement system (DAK-12, Schmid & Partner Engineering AG, Switzerland) during the mixing procedure and just before the measurements with our MWT prototype. Measured relative permittivity and conductivity can also be found in the Table 4.1.

Table 4.1, Phantoms composition and measured dielectric parameters at 1 GHz. Compositions are in weight percent at 20 °C.

	Deionized water	NaCl	Isopropyl alcohol	σ (S/m)	ϵ_r (-)
Background	48.35	1.16	50.49	0.94	40.1
Ischemic	39.57	0.17	60.27	0.49	37.5
Hemorrhagic	55.19	1.43	43.37	1.35	50.3

4.1.5 Measuring procedure

Measuring container was firstly filled with liquid homogenous phantom of brain grey matter phantom material. Special attention was payed to elimination of bubbles which appeared on the surface of antennas during filling of the container. Finally, the container was enclosed by microwave pyramid absorbers. The absorbers helped to decrease noise level in measured signals caused by reflections of electromagnetic waves from surroundings and bring the boundary conditions closer to the boundary conditions used in numerical simulations. The measurement was composed from three main procedures: (1) measurement with grey matter phantom only, (2) measurement with phantom of haemorrhagic stroke and (3) measurement with phantom of necrotic stroke. Phantoms of strokes were subsequently positioned and measured in all marked spots (Figure 4.3). Whole S-parameter matrix was measured 10 times in series to cover fluctuations that can appear during the measurement for every configuration. One measurement of full S-parameter matrix takes about 7 s.

4.2 Results

Performance of our microwave system was evaluated both with synthetic and measured data. Synthetic data were obtained from numerical simulations of numerical model of our system in

Comsol Multiphysics. The data then underwent the image reconstruction procedure (positions 1, 2, 3, 4, 5, 17, 18, 19, 25 were selected for purpose of this chapter). Thanks to a symmetry of the system, these nine different positions cover all the possible configurations.

Reconstruction algorithm and procedure of getting image of relative permittivity and conductivity from measured S-parameters are described in Chapter 2.

4.2.1 Measured data

An example of measured S-parameters is shown in Figure 4.4. These data are for the case when the container was filled by grey matter phantom and when two different strokes were placed at position P1. Real and imaginary part of S-parameters are plotted separately on the graphs. Differences between data measured on container filled with phantom of grey matter and first and second type of stroke phantom were computed later and plotted together with standard deviations of repeated measurement in Figure 4.5. T-test ($\alpha = 0.01$) was applied to disprove a hypothesis, that the measured S-parameters are the same for state with and without inhomogeneity included. Very small standard deviations can be observed in repeatedly measured S parameters for both real and imaginary part of all S parameters. Arithmetic mean of repeatedly measured S parameters for every position (10 times) was therefore used in reconstruction procedure. Standard deviations computed from S parameters measured in all 25 positions of strokes were computed and compared with standard deviations of S parameters measured with container filled with grey mater phantom only. The results are shown in Figure 4.6.

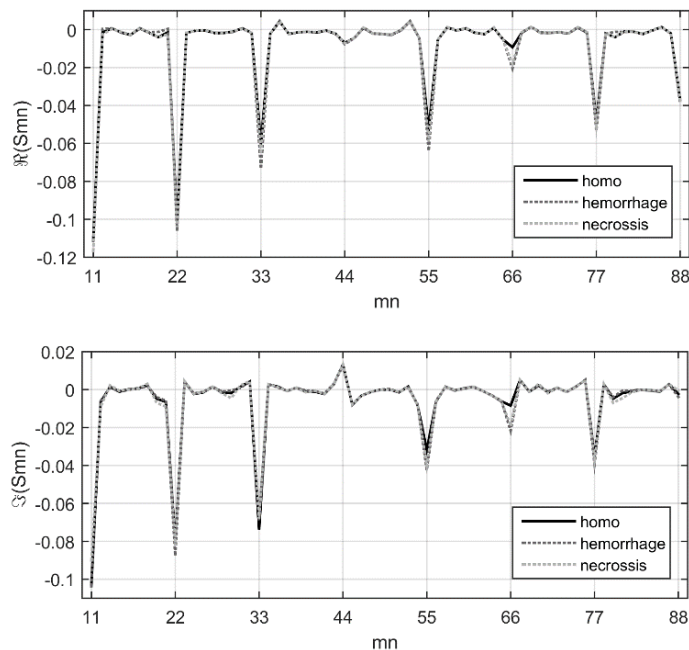


Figure 4.4, Example of measured data – real and imaginary part of measured S-parameter matrix when the measuring container was filled with homogenous phantom only and when the inhomogeneities were included subsequently.

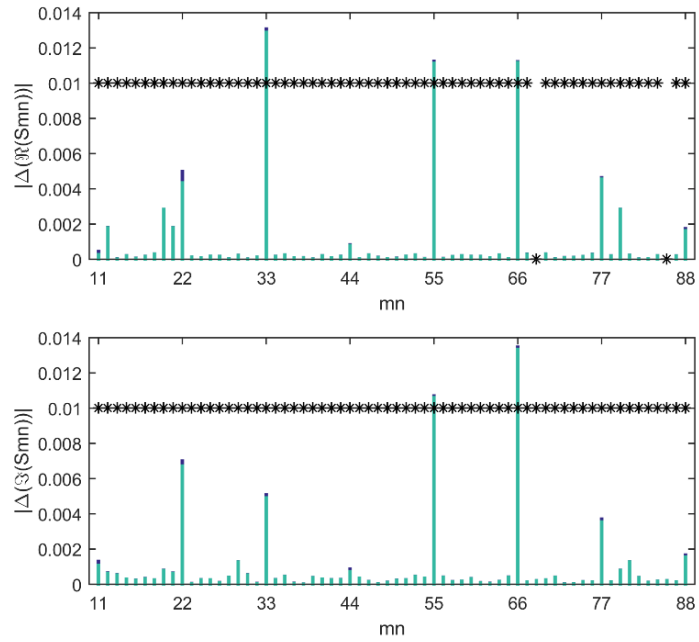


Figure 4.5, Differences in measured signals (haemorrhagic stroke phantom at position P1 vs. grey matter phantom) are represented by green bars, with standard deviations ($2 \cdot \text{stdHA} + 2 \cdot \text{stdEmpty}$) represented by blue bars on the top. Results of T-test at the significance level of 1 % are represented by black stars (0.01 – hypothesis was not supported, 0 hypothesis was supported).

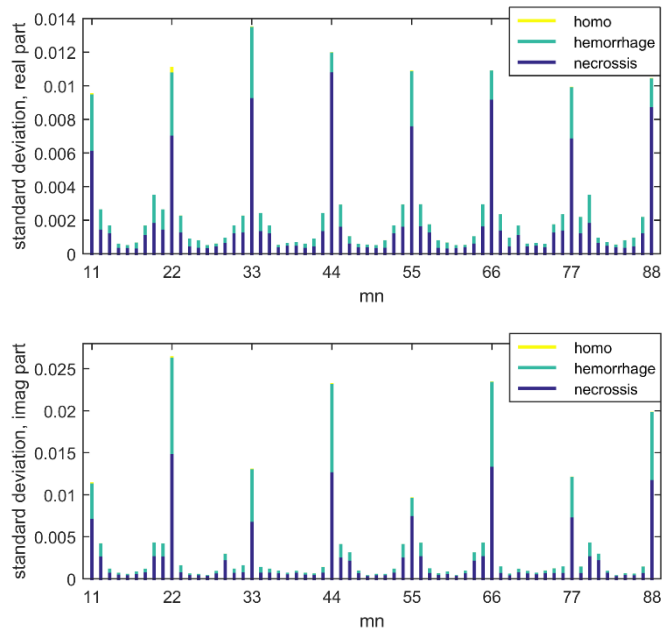


Figure 4.6, Standard deviation in measured S parameters for all positions of strokes together.

4.2.2 Detection of stroke and its position

Reconstructed images of dielectric parameters were processed in the following way, to show how well the strokes in different positions were detected after first iteration of the algorithm. Firstly, arithmetic mean in the resulting images was calculated. Secondly, positions of 400 extreme values (biggest Euclidian distance from the arithmetic mean) were detected in all the reconstructed images. The number of shown extremes was deduced from size of an area of one pixel of the reconstructed image and an area of cross section of the stroke phantom (circle with radius of 2 cm). Dots of specific colour represent detected extremes corresponding to a specific

position of the stroke phantom. Circles of the same colour represents actual position of the stroke phantom. The more dots of the same colour are inside of the circle with the same colour, the better are the results of the reconstruction (see Figure 4.7). In general, conductivity is much better reconstructed than relative permittivity. This is apparently caused by the fact, that there is for both cases much higher contrast between stroke and grey matter in conductivity (42 % increase for haemorrhagic and 47 % decrease for necrotic), than in permittivity (27 % increase for haemorrhagic and 6 % decrease for necrotic). There are also some locations in the reconstructed images, where extreme values were detected without any relationship to the actual position of stroke (dots of different colours overlap in those regions). This effect can be caused by insufficient quality of calibration of the system and repeatability of manufacturing procedure of antennas, where one antenna behaves differently from the remaining - it can be observed especially in the area close to the measuring container boundaries and antenna number 6. Even if the position of strokes is not detected perfectly for every position, we still could define which part of the head was affected. The stroke phantoms closer to the boundary of measuring container are also generally detected better. It is probably related to signal to noise ratio of measured signal and the fact, that EM waves traveling for longer distances in lossy dielectric phantom are naturally more attenuated.

4.3 Conclusion

A Prototype of a laboratory microwave imaging system developed at Czech Technical University in Prague (Faculty of Biomedical Engineering, Dept. of Biomedical Technology) was described in this chapter. The prototype was designed as our first attempt to develop a laboratory microwave imaging system for testing of various antenna elements, imaging and classification algorithms, and head phantoms for the early detection and classification of human brain strokes. Design of the system, measurement setup, measurement procedure and measured data are described in this chapter. Two different phantoms of human brain strokes (haemorrhagic and necrotic) were prepared and measured at 25 different positions in the measuring container filled by the phantom of human grey matter.

Measured S-parameters were inspected and then underwent the image reconstruction procedure. Possibility of the stroke detection and classification from the reconstructed images was evaluated. Finally, results of reconstruction achieved with measured data were compared to results achieved with synthetic data. These results support the statements of another groups working in this field, that the detection and differentiation of the strokes by means of microwave technique should be possible.

We decided to use dielectric image reconstruction algorithm previously used for detection of breast cancer to process the measured data. Although advantage of machine learning algorithms can be clearly seen in achieved results of several research groups (including ours), its ease of use and implementation, we believe that for medical doctors it will always be important to see what is actually happening inside of the examined region and what data is the recommended decision of machine learning algorithms based on. It will always be the specialist who must make the final decision, not the algorithm. On the other hand, images generated by reconstruction algorithms can be often very confusing despite the fact, that the measured data can contain enough information to make right decision. This led us to a concept of synergy of those two processing procedures of measured data: combining reconstructed images with decision recommended by machine learning algorithm.

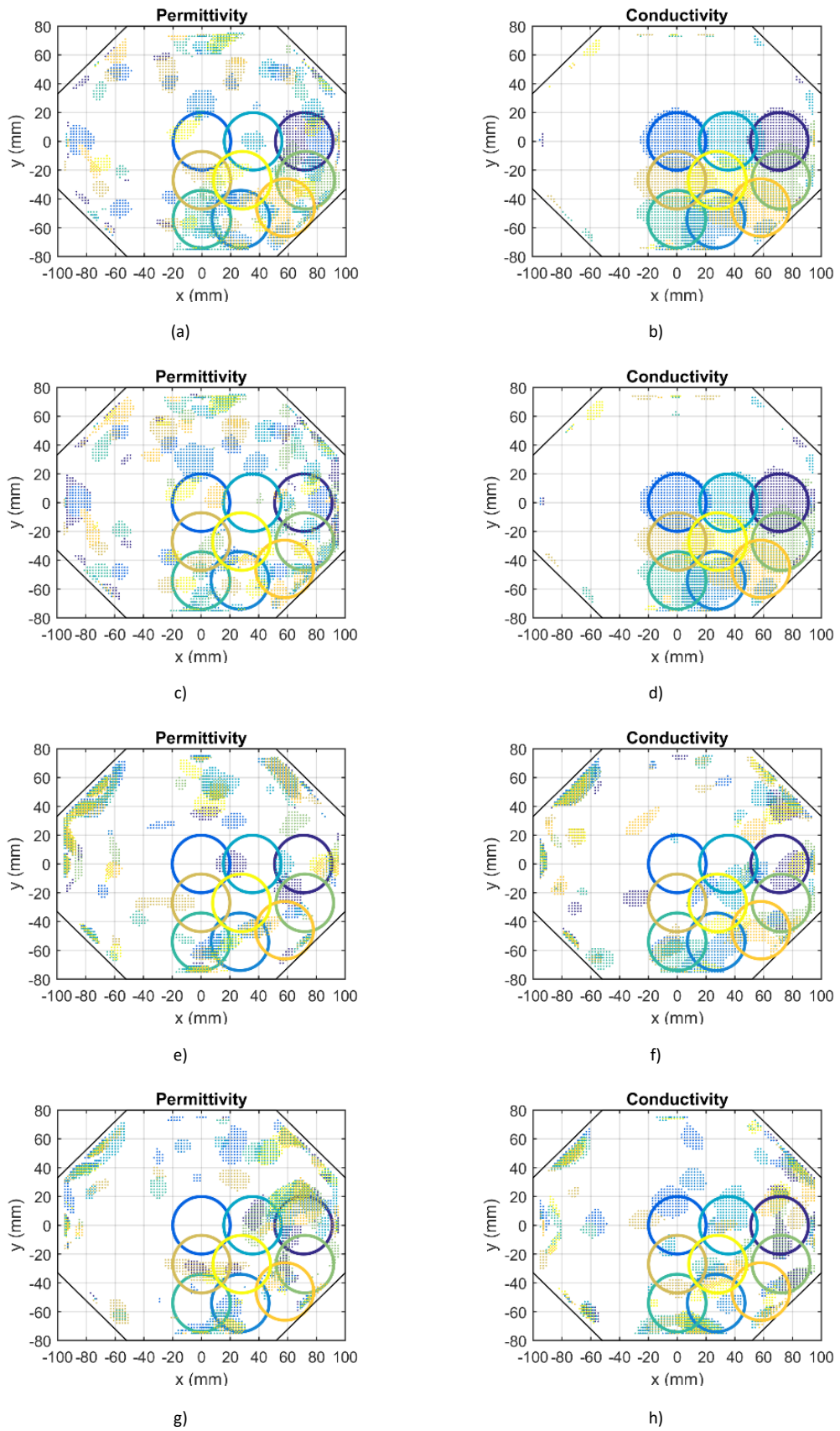


Figure 4.7, Cumulative images showing detection of strokes (every color represents one position – namely P1, P2, P3, P4, P5, P17, P18, P19, P25) a), b) – synthetic data, hemorrhage, c), d) – synthetic data necrosis, e), f) – measured data, hemorrhage, g), h) – measured data necrosis.

In our future work, we are going to improve our system in several ways to deal with some major known issues such as low sensitivity, spatial resolution, and sensitivity to noise. New antenna elements will be designed and more of them will be used in the container. Shape of the container will be modified to better fit on a real human head. We are also aware of simplified shapes of stroke phantoms and so study of strokes of different shapes and sizes must be conducted.

In chapter 9, evolved version of the system described here is thoroughly investigated.

5. Temperature Dependent Complex Permittivity Model of Agar Phantom for Microwave Temperature Distribution Monitoring During Microwave Hyperthermia Treatment

It is well known fact, that the dielectric parameters of materials are not only frequency but also temperature dependent. This fact leads to the idea using MWT for noninvasive monitoring of the temperature in human body during cancer treatment procedure called microwave hyperthermia. In order to allow testing of a MWT prototypes for this purpose, tissue simulating materials with known temperature dependency of its dielectric properties are needed. From that reason complex permittivity of agar phantom material was measured and the parameters of temperature dependent model were estimated in this chapter.

As the changes in complex permittivity due to a temperature change are very low, high precision and error free measurement is crucial and so our experiences with measurement with open ended coaxial probe at University of Galway, Ireland are described in chapter 6.

This chapter is thus dedicated to a measurement of complex permittivity of agar phantom at different temperatures and estimation of noise related with sensing volume of the method used for the measurement – in this case open ended coaxial probe. Aim of our work is to estimate temperature dependent parameters of mathematical model of this dielectric. The measuring procedure as well as data processing procedure is described and verified on distilled water. While measuring the agar phantom, the procedure becomes more challenging. Measured data contain more noise, the changes due to the change of the temperature are smaller and homogenous heating of the sample large enough to cover sensing volume of the probe is time consuming.

5.1 Introduction

The agar phantom [53] is used at our university for two main purposes. One of the applications is testing of newly designed microwave hyperthermia applicators. Temperature of the phantom can be increased from 20 °C to 40 °C during power measurement. The second application relates to non-invasive temperature monitoring by means of microwave radar or microwave tomography, where the exact temperature is estimated from absolute or relative change in complex permittivity in monitored region.

5.2 Measuring set up

The measuring setup is depicted in Figure 5.1. It composes from heating bath, thermometer, vector network analyser and measuring probe. Heating bath was filled with distilled water and allowed us to heat water int the bath in 1 °C steps. Although heating bath contains built in thermometer, temperature of water was also monitored by using external thermometer (Votcraft K204). Measuring coaxial probe (DAK 12, Speag AG) was fixed in laboratory stand and connected by coaxial cable to the network vector analyser (Keysight FieldFox N9923A). Personal computer with preinstalled software (delivered with probe kit) connected to the network vector analyser was used to operate with the analyser and to trigger a calibration procedure and the measurement. Calibration was performed with three calibration standards (short, open, distilled water) ahead of every measurement. The analyser was turned on 90 minutes prior the calibration and the first measurement.

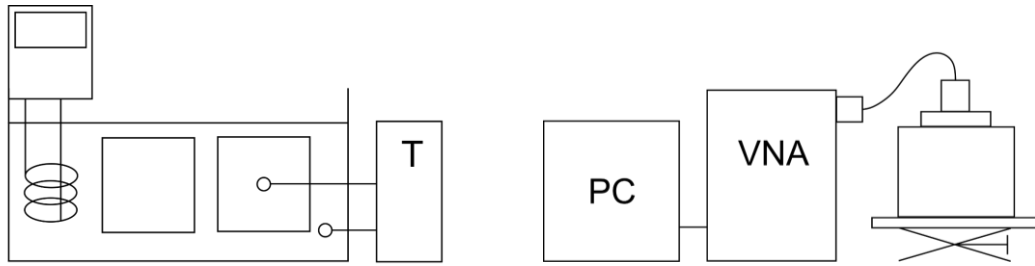


Figure 5.1, Measuring setup for measurement of complex permittivity of the agar phantom at different temperatures. (PC – personal computer, VNA – vector network analyser, T – thermometer and temperature stable water bath)

5.3 Measurement procedure

Firstly, complex permittivity of distilled water sample was measured. Container with volume of 1 dm^3 was filled with water sample and placed into the water bath. Temperature probe was inserted into the sample. Lowest temperature ($20 \text{ }^\circ\text{C}$) from wanted temperature range was set up at the water bath control panel. Temperature in the water bath and the sample was continuously monitored till the temperature equalization has appeared. Water in the sample container was occasionally mixed to speed up the temperature equalization process. After the calibration, sample container was taken out of the water bath and placed on the lifting table under the probe. Sample was lifted to immerse the probe into it and so any movement of coaxial cable and probe was avoided. Tip of the probe was observed for bubbles. Finally, complex permittivity was measured in 201 frequency points in frequency range going linearly from 50 MHz to 3 GHz.

Agar phantom complex permittivity measurement was very similar to water sample measurement, but two identical samples were used instead of one. Agar phantoms with shape of a cylinder (diameter of 11 cm, height of 6 cm) were prepared in two identical specimens according to the recipe published in [53]. Both specimens of the phantom were placed in the water bath. One temperature probe was placed in the middle of one of the phantoms, second was placed in the water bath. Second specimen of the phantom without the temperature probe was used for measurement of complex permittivity and so needs to stay undamaged (not penetrated by temperature probe). Then there was time for temperature equalization between water and the first phantom (temperature inside of the second phantom was expected to be the same). After temperature equalization, NVA was calibrated, phantom without temperature probe was placed on the lifting table and its complex permittivity was measured. The procedure is depicted in Figure 5.2.

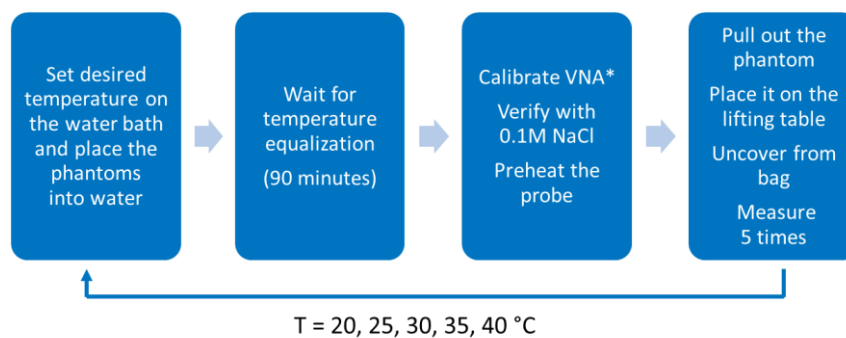


Figure 5.2, Procedure of complex permittivity measurement

5.4 Data processing

One pole Debye model (eq. 1) was fitted to measured data for every temperature by using genetic algorithm [55].

$$\hat{\varepsilon}(\omega, t) = \varepsilon_{\infty}(t) + \frac{\varepsilon_s(t) - \varepsilon_{\infty}(t)}{1 + j\omega\tau(t)} + \frac{\sigma_i(t)}{j\omega\varepsilon_{air}} \quad (1)$$

Thanks to it we got the parameters of Debye model for distilled water and agar phantom at every measured temperature. In the next step we were looking for functions which models the best the temperature dependent parameters. Another fitting procedure was performed to estimate the parameters of these functions. Finally, we established four equations defining dependency of Debye model parameters on temperature. The procedure is depicted in Figure 5.3.

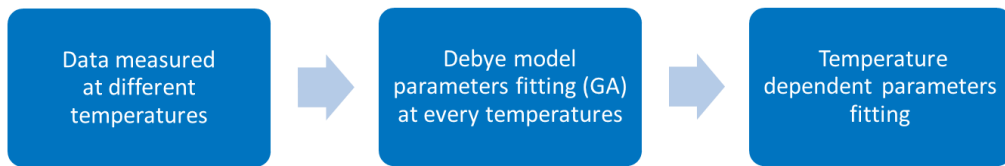


Figure 5.3, Data processing procedure.

5.5 Results

The data measured on distilled water together with fitted models are depicted on Figure 5.5. Despite the contamination of the traces with noise, temperature dependent parameters of one pole Debye model were estimated. Although we followed recommendations of the probe kit developer (1 dm³ container), this noise was probably connected with small size of the sample container. This can be quite easily verified by moving of the sample from middle axes of the probe to the edge of the container during continuous measurement of complex permittivity – changes in the amount of noise are proportional to probe position relative to the container. Therefore, we also carried out numerical analysis of this problem.

The data measured on the agar phantom were according to our assumptions even more noisy (Figure 5.5). Parameters of the model were estimated in the same manner as for the distilled water. Nevertheless, we are distrustful of the quality of the data and model and decided to repeat the measurement with a vision of better quality of the results. However, we believe that following statement can be made. Average change in relative permittivity equals to 0.3 per 1°C and 0.013 S/m per 1°C in conductivity (depending on frequency).

5.6 Conclusion - noise in measured data and sensing volume

The coaxial probe used for measurement was modelled in RF module of COMSOL Multiphysics. Precise dimensions and permittivity of dielectric bead material can be found in the documentation of the probe. Diameter of the flange equals to 48 mm, inner diameter of the outer conductor to 12 mm and diameter of the inner conductor to 3.18 mm (cross section of the probe can be seen on the top of the Figure 5.6. The probe was virtually facing into the cylinder filled with distilled water and the flange of the probe was covered from the top side by air. Scattering boundary conditions were applied on all boundaries of the computational domain. Numerical simulation of electromagnetic field was then calculated in declared working frequency band of the probe (10 MHz to 3 GHz with step of 200 MHz). Contours of 25 dB decrease in absolute value of E field were extracted from the results and are depicted in Figure

5.6. From the contours we can see that the E field expands the most in the frequency band from 1 GHz to 2.4 GHz. This could explain the biggest amount of noise occurring in all of our measurements, where the noisiest part can be found in the same frequency band. The smallest needed container size filled with distilled water can also be roughly estimated from our study. We can see that the diameter of the container must not be underestimated – it must be almost double of the height. Size of the sensing volume of the probe of this size is not as surprising, but must be kept in mind especially when previous experiences of an experimenter are with Performance or Slim Form probe (Keysight Technologies, Santa Rosa, CA, USA) whose are much smaller and so its sensing volume does not exceed a few millimeters only [56].

In order to get better results while keeping the size of the sample for calibration the same, liquid with higher conductivity can be used as load calibration standard. For our purpose we used 0.1M solution of NaCl. Results from the measurement on the same agar phantom are shown in Figure 5.7. There are three lines in every graph. The blue one corresponds to a measurement in the middle of the phantom, the red one corresponds to a measurement closer to the edge of the phantom. The amplitude of the ripples in the traces still increases from the middle to the edge of the phantom, but is much smaller when compared with the measurement, where distilled water was used as the third (load) calibration standard.

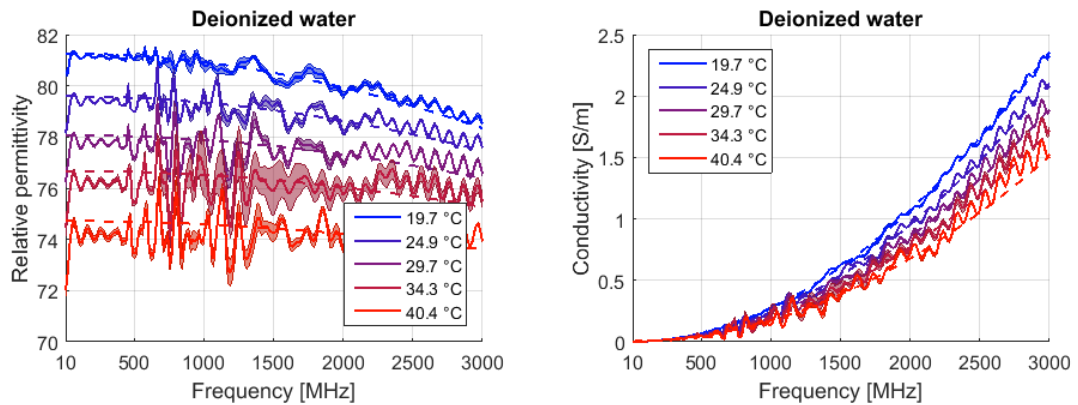


Figure 5.4, Measured complex permittivity of distilled water (solid lines) with standard uncertainty together with fitted model (dashed lines).

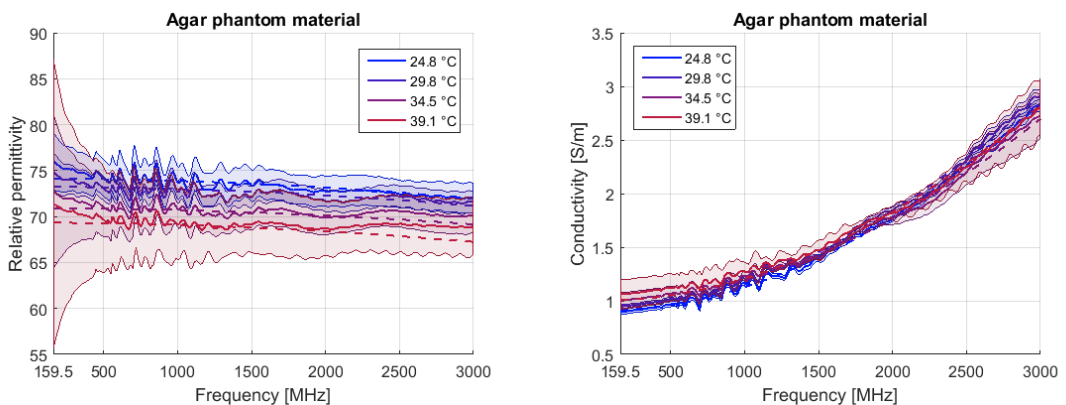


Figure 5.5, Measured complex permittivity of agar phantom (solid lines) with standard uncertainty together with fitted model (dashed lines).

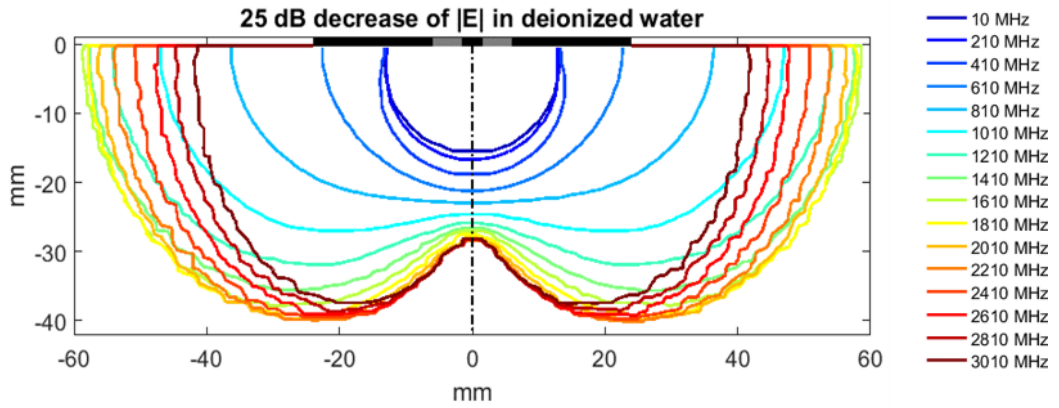


Figure 5.6, A 25 dB decrease in amplitude of E-field in deionized water for different frequencies.

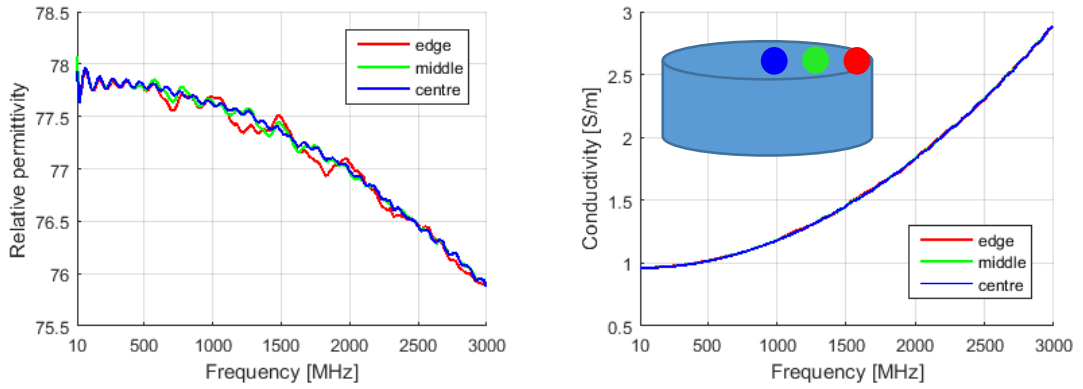


Figure 5.7, Measurement on the same agar phantom but after calibration with 0.1 M NaCl in the same container.

References for chapters 1 till 5

- [1] P. M. Meaney, "Microwave Imaging and Emerging Applications," *Int. J. Biomed. Imaging*, vol. 2012, 2012.
- [2] B. G. Nair, *Active Microwave Imaging for Mammography*. Saarbrücken, Deutschland: LAP LAMBERT, 2012.
- [3] M. Lazebnik *et al.*, "A large-scale study of the ultrawideband microwave dielectric properties of normal, benign and malignant breast tissues obtained from cancer surgeries," *Phys. Med. Biol.*, vol. 52, no. 20, pp. 6093–6115, Oct. 2007.
- [4] S. Semenov, "Microwave tomography: review of the progress towards clinical applications," *Philos. Transact. A Math. Phys. Eng. Sci.*, vol. 367, no. 1900, pp. 3021–3042, Aug. 2009.
- [5] S. Noghianian, "Microwave Tomography for Biomedical Quantitative Imaging," *J. Electr. Electron.*, vol. 01, no. 03, 2012.
- [6] "Cancer Facts and Statistics | American Cancer Society." [Online]. Available: <http://www.cancer.org/research/cancerfactsstatistics/index>. [Accessed: 27-Aug-2015].
- [7] S. S. Chaudhary, R. K. Mishra, A. Swarup, and J. M. Thomas, "Dielectric properties of normal & malignant human breast tissues at radiowave & microwave frequencies," *Indian J. Biochem. Biophys.*, vol. 21, no. 1, pp. 76–79, Feb. 1984.
- [8] S. Noghianian, A. Sabouni, T. Desell, and A. Ashtari, *Microwave Tomography: Global Optimization, Parallelization and Performance Evaluation*. Springer, 2014.
- [9] P. M. Meaney *et al.*, "Initial Clinical Experience with Microwave Breast Imaging in Women with Normal Mammography," *Acad. Radiol.*, vol. 14, no. 2, pp. 207–218, Feb. 2007.
- [10] M. Klemm, I. Craddock, J. Leendertz, A. Preece, and R. Benjamin, "Experimental and clinical results of breast cancer detection using UWB microwave radar," in *IEEE Antennas and Propagation Society International Symposium, 2008. AP-S 2008*, 2008, pp. 1–4.
- [11] J. Bourqui, J. M. Sill, and E. C. Fear, "A Prototype System for Measuring Microwave Frequency Reflections from the Breast," *Int. J. Biomed. Imaging*, vol. 2012, 2012.
- [12] A. Fhager, M. Gustafsson, and S. Nordebo, "Image Reconstruction in Microwave Tomography Using a Dielectric Debye Model," *IEEE Trans. Biomed. Eng.*, vol. 59, no. 1, pp. 156–166, Jan. 2012.
- [13] R. C. Conceicao, D. Byrne, J. A. Noble, and I. Craddock, "Microwave Imaging of the Breast: Investigating Tumour Response with Classification," presented at the Progress In Electromagnetics Research Symposium, Prague, vol. 2015.
- [14] M. Persson *et al.*, "Microwave based diagnostics and treatment in practice," in *Microwave Workshop Series on RF and Wireless Technologies for Biomedical and Healthcare Applications (IMWS-BIO)*, 2013 IEEE MTT-S International, 2013, pp. 1–3.
- [15] E. C. Fear, X. Li, S. C. Hagness, and M. A. Stuchly, "Confocal microwave imaging for breast cancer detection: localization of tumors in three dimensions," *IEEE Trans. Biomed. Eng.*, vol. 49, no. 8, pp. 812–822, Aug. 2002.
- [16] L. Guo and A. M. Abbosh, "Optimization-Based Confocal Microwave Imaging in Medical Applications," *IEEE Trans. Antennas Propag.*, vol. 63, no. 8, pp. 3531–3539, Aug. 2015.
- [17] M. A. Elahi, A. Shahzad, M. Glavin, E. Jones, and M. O'Halloran, "Hybrid Artifact Removal for Confocal Microwave Breast Imaging," *IEEE Antennas Wirel. Propag. Lett.*, vol. 13, pp. 149–152, 2014.
- [18] Hooi Been Lim, Nguyen Thi Tuyet Nhung, Er-Ping Li, and Nguyen Duc Thang, "Confocal Microwave Imaging for Breast Cancer Detection: Delay-Multiply-and-Sum Image Reconstruction Algorithm," *IEEE Trans. Biomed. Eng.*, vol. 55, no. 6, pp. 1697–1704, Jun. 2008.
- [19] M. Pastorino, *Microwave Imaging*, 1 edition. Hoboken, N.J: Wiley, 2010.
- [20] M. Pastorino, "Stochastic Optimization Methods Applied to Microwave Imaging: A Review," *IEEE Trans. Antennas Propag.*, vol. 55, no. 3, pp. 538–548, Mar. 2007.

- [21] P. M. Meaney *et al.*, "Microwave tomography in the context of complex breast cancer imaging," in *2010 Annual International Conference of the IEEE Engineering in Medicine and Biology Society (EMBC)*, 2010, pp. 3398–3401.
- [22] P. Rocca, M. Benedetti, M. Donelli, D. Franceschini, and A. Massa, "Evolutionary optimization as applied to inverse scattering problems," *Inverse Probl.*, vol. 25, no. 12, p. 123003, Dec. 2009.
- [23] A. Fhager, A. Voronov, C. Chen, and M. Persson, "Methods for Dielectric Reconstruction in Microwave Tomography," in *The Second European Conference on Antennas and Propagation, 2007. EuCAP 2007*, 2007, pp. 1–6.
- [24] M. Donelli and A. Massa, "Computational approach based on a particle swarm optimizer for microwave imaging of two-dimensional dielectric scatterers," *IEEE Trans. Microw. Theory Tech.*, vol. 53, no. 5, pp. 1761–1776, May 2005.
- [25] A. Sabouni, S. Noghianian, and S. Pistorius, "A global optimization technique for microwave imaging of the inhomogeneous and dispersive breast," *Can. J. Electr. Comput. Eng.*, vol. 35, no. 1, pp. 15–24, Winter 2010.
- [26] P. M. Meaney *et al.*, "Comparison of fibroglandular tissue distributions for microwave tomographic breast images with complementary MR T2 weighted images," 2004, vol. 3, pp. 1314–1316.
- [27] M. Pastorino, S. Caorsi, and A. Massa, "A global optimization technique for microwave nondestructive evaluation," *IEEE Trans. Instrum. Meas.*, vol. 51, no. 4, pp. 666–673, Aug. 2002.
- [28] X. Chen, D. Liang, and K. Huang, "Microwave Imaging 3-D Buried Objects Using Parallel Genetic Algorithm Combined With FDTD Technique.," *J. Electromagn. Waves Appl.*, vol. 20, no. 13, pp. 1761–1774, Nov. 2006.
- [29] S. Caorsi, A. Costa, and M. Pastorino, "Microwave imaging within the second-order Born approximation: stochastic optimization by a genetic algorithm," *IEEE Trans. Antennas Propag.*, vol. 49, no. 1, pp. 22–31, Jan. 2001.
- [30] A. Sabouni, A. Ahtari, S. Noghianian, G. Thomas, and S. Pistorius, "Hybrid Binary-Real GA Optimization Approach for Breast Microwave Tomography," *Appl. Comput. Electromagn. Soc. J.*, vol. 28, no. 11, pp. 1005–1016, Nov. 2013.
- [31] B. Mhamdi, K. Grayaa, and T. Aguilii, "Microwave imaging of dielectric cylinders from experimental scattering data based on the genetic algorithms, neural networks and a hybrid micro genetic algorithm with conjugate gradient," *AEU - Int. J. Electron. Commun.*, vol. 65, no. 2, pp. 140–147, Feb. 2011.
- [32] A. Ashtari, S. Noghianian, A. Sabouni, J. Aronsson, G. Thomas, and S. Pistorius, "Using a priori Information for Regularization in Breast Microwave Image Reconstruction," *IEEE Trans. Biomed. Eng.*, vol. 57, no. 9, pp. 2197–2208, Sep. 2010.
- [33] A. Semnani, M. Kamyab, and I. T. Rekanos, "Reconstruction of One-Dimensional Dielectric Scatterers Using Differential Evolution and Particle Swarm Optimization," *IEEE Geosci. Remote Sens. Lett.*, vol. 6, no. 4, pp. 671–675, Oct. 2009.
- [34] M. Brignone, G. Bozza, A. Randazzo, M. Piana, and M. Pastorino, "A Hybrid Approach to 3D Microwave Imaging by Using Linear Sampling and ACO," *IEEE Trans. Antennas Propag.*, vol. 56, no. 10, pp. 3224–3232, Oct. 2008.
- [35] P. M. Meaney *et al.*, "Integration of microwave tomography with magnetic resonance for improved breast imaging," *Med. Phys.*, vol. 40, no. 10, p. 103101, Oct. 2013.
- [36] M. O'Halloran, R. C. Conceicao, D. Byrne, M. Glavin, and E. Jones, "FDTD MODELING OF THE BREAST: A REVIEW," *Prog. Electromagn. Res. B*, vol. 18, pp. 1–24, 2009.
- [37] C.-T. Tai, *Dyadic Green Functions in Electromagnetic Theory*. IEEE Press, 1994.
- [38] P. M. Morse and H. Feshbach, *Methods of theoretical physics*. McGraw-Hill, 1953.
- [39] R. F. Harrington, *Time-harmonic electromagnetic fields*. McGraw-Hill, 1961.

- [40] N. Joachimowicz, C. Pichot, and J. P. Hugonin, "Inverse scattering: an iterative numerical method for electromagnetic imaging," *IEEE Trans. Antennas Propag.*, vol. 39, no. 12, pp. 1742–1753, Dec. 1991.
- [41] Q. Fang, P. M. Meaney, S. D. Geimer, A. V. Streltsov, and K. D. Paulsen, "Microwave image reconstruction from 3-D fields coupled to 2-D parameter estimation," *IEEE Trans. Med. Imaging*, vol. 23, no. 4, pp. 475–484, Apr. 2004.
- [42] R. C. Conceição, J. J. Mohr, and M. O'Halloran, *An Introduction to Microwave Imaging for Breast Cancer Detection*. Springer, 2016.
- [43] P. M. Meaney, M. W. Fanning, D. Li, S. P. Poplack, and K. D. Paulsen, "A clinical prototype for active microwave imaging of the breast," *IEEE Trans. Microw. Theory Tech.*, vol. 48, no. 11, pp. 1841–1853, Nov. 2000.
- [44] M. Haynes, J. Stang, and M. Moghaddam, "Real-time Microwave Imaging of Differential Temperature for Thermal Therapy Monitoring," *IEEE Trans. Biomed. Eng.*, vol. 61, no. 6, pp. 1787–1797, Jun. 2014.
- [45] S. Semenov *et al.*, "Microwave tomography of extremities: 1) Dedicated 2D system and physiological signatures," *Phys. Med. Biol.*, vol. 56, no. 7, pp. 2005–2017, Apr. 2011.
- [46] A. Fhager, P. Hashemzadeh, and M. Persson, "Reconstruction Quality and Spectral Content of an Electromagnetic Time-Domain Inversion Algorithm," *IEEE Trans. Biomed. Eng.*, vol. 53, no. 8, pp. 1594–1604, Aug. 2006.
- [47] W. Haddad and J. Trebes, "Microwave hemorrhagic stroke detector," US20030018244 A1, 23-Jan-2003.
- [48] M. Persson *et al.*, "Microwave-Based Stroke Diagnosis Making Global Prehospital Thrombolytic Treatment Possible," *IEEE Trans. Biomed. Eng.*, vol. 61, no. 11, pp. 2806–2817, Nov. 2014.
- [49] M. Persson, A. Fhager, and P. Hashemzadeh, "Solution for internal monitoring of body," US20100174179 A1, 08-Jul-2010.
- [50] M. Persson, M. Alikhorshidi, T. Mckelvey, H. Yousefimesri, and M. K. Najafabadi, "Classification of microwave scattering data," US20120190977 A1, 26-Jul-2012.
- [51] A. Abbosh, "Microwave systems for head imaging: Challenges and recent developments," in 2013 IEEE MTT-S International Microwave Workshop Series on RF and Wireless Technologies for Biomedical and Healthcare Applications (IMWS-BIO), 2013, pp. 1–3.
- [52] D. Ireland, K. Bialkowski, and A. Abbosh, "Microwave imaging for brain stroke detection using Born iterative method," *Antennas Propag. IET Microw.*, vol. 7, no. 11, pp. 909–915, Aug. 2013.
- [53] H. Kato, M. Hiraoka, and T. Ishida, "An agar phantom for hyperthermia," *Med. Phys.*, vol. 13, no. 3, pp. 396–398, Jun. 1986.
- [54] Title: "Dielectric Property Measurements of Biological Tissues: Basis for the development of a refined standard," A. La Gioia, E. Porter, I. Merunka, M. Jones, and M. O'Halloran, "Dielectric Property Measurements of Biological Tissues: Basis for the development of a refined standard."
- [55] J. Clegg and M. P. Robinson, "A genetic algorithm used to fit Debye functions to the dielectric properties of tissues," in 2010 IEEE Congress on Evolutionary Computation (CEC), 2010, pp. 1–8.
- [56] P. M. Meaney, A. Gregory, N. Epstein, and K. D. Paulsen, "Microwave open-ended coaxial dielectric probe: interpretation of the sensing volume re-visited," *BMC Med Phys*, vol. 14, no. 1, p. 3, 2014.
- [57] C. Gilmore *et al.*, "A Wideband Microwave Tomography System With a Novel Frequency Selection Procedure," *IEEE Trans. Biomed. Eng.*, vol. 57, no. 4, pp. 894–904, 2010.
- [58] M. Guardiola, L. Jofre, S. Capdevila, S. Blanch, and J. Romeu, "3D UWB magnitude-combined tomographic imaging for biomedical applications. algorithm validation," *Radioengineering*, vol. 20, no. 2, pp. 366–372, 2011.

- [59] M. A. Hernandez-Lopez, M. Quintillan-Gonzalez, S. Gonzalez Garcia, A. Rubio Bretones, and R. Gomez Martin, "A rotating array of antennas for confocal microwave breast imaging," *Microw. Opt. Technol. Lett.*, vol. 39, no. 4, pp. 307–311, Nov. 2003.
- [60] J. Vrba, C. Franconi, F. Montecchia, and I. Vannucci, "Evanescent-mode applicators (EMA) for superficial and subcutaneous hyperthermia," *IEEE Trans. Biomed. Eng.*, vol. 40, no. 5, pp. 397–407, May 1993.
- [61] B. Vrbova and J. Vrba, "Microwave Thermotherapy in Cancer Treatment: Evaluation of Homogeneity of SAR Distribution," *Prog. Electromagn. Res.*, vol. 129, pp. 181–195, 2012.
- [62] M. Persson, A. Fhager, H. D. Trefna, and X. Zeng, "Broadband microwave based diagnostics and treatment," in *2009 3rd European Conference on Antennas and Propagation*, 2009, pp. 1873–1876.
- [63] M. Persson, A. Fhager, H. D. Trefna, and T. McKelvey, "Microwave based diagnostics and treatment," in *2013 7th European Conference on Antennas and Propagation (EuCAP)*, 2013, pp. 3118–3119.
- [64] J. Bourqui, M. Okoniewski, and E. C. Fear, "Balanced Antipodal Vivaldi Antenna With Dielectric Director for Near-Field Microwave Imaging," *IEEE Trans. Antennas Propag.*, vol. 58, no. 7, pp. 2318–2326, 2010.
- [65] SPEAG AG, "SEMCAD X Reference Guide." [Online]. Available: <http://download.speag.com/releases/semcad/14-8-5/documentation/SEMCAD-X-Manual.pdf>.
- [66] S. K. Davis, H. Tandradinata, S. C. Hagness, and B. D. V. Veen, "Ultrawideband microwave breast cancer detection: a detection-theoretic approach using the generalized likelihood ratio test," *IEEE Trans. Biomed. Eng.*, vol. 52, no. 7, pp. 1237–1250, Jul. 2005.
- [67] X. Li and S. C. Hagness, "A confocal microwave imaging algorithm for breast cancer detection," *IEEE Microw. Wirel. Compon. Lett.*, vol. 11, no. 3, pp. 130–132, Mar. 2001.
- [68] "Dielectric Properties of Body Tissues: Home page." [Online]. Available: <http://niremf.ifac.cnr.it/tissprop/>. [Accessed: 31-Oct-2017].
- [69] P. Hasgall *et al.*, "IT'IS database for thermal and electromagnetic parameters of biological tissues," Jan-2015. [Online]. Available: www.itis.ethz.ch/database.
- [70] C. Boutelier, L. Bougues, and J. Timbal, "Experimental study of convective heat transfer coefficient for the human body in water," *Journal of applied physiology: respiratory, environmental and exercise physiology*, vol. 42, no. 1, pp. 93–100, Jan. 1977.
- [71] S. Semenov, J. Kellam, Y. Sizov, A. Nazarov, T. Williams, B. Nair, A. Pavlovsky, V. Posukh, and M. Quinn, "Microwavetomography of extremities: 1) Dedicated 2d system and physiological signatures," *Physics in medicine and biology*, vol. 56, no. 7, pp. 2005–2017, Apr. 2011. [Online]. Available: <http://www.ncbi.nlm.nih.gov/pmc/articles/PMC3140418/>
- [72] F. S. d. Clemente, M. Helbig, J. Sachs, U. Schwarz, R. Stephan, and M. A. Hein, "Permittivity-matched compact ceramic ultra-wideband horn antennas for biomedical diagnostics," in *Proceedings of the 5th European Conference on Antennas and Propagation (EuCAP)*, Apr. 2011, pp. 2386–2390.
- [73] X. Li, *Body Matched Antennas for Microwave Medical Applications*, 2013. [Online]. Available: <https://publikationen.bibliothek.kit.edu/1000037615>

6. Dielectric Measurement of Biological Tissues: Challenges and Common Practices

This chapter is based on following published paper:

Alessandra La Gioia, Emily Porter, Ilja Merunka, Atif Shahzad, Saqib Salahuddin, Marggie Jones and Martin O'Halloran:

"Open-Ended Coaxial Probe Technique for Dielectric Measurement of Biological Tissues: Challenges and Common Practices",

***Diagnostics*, 2018, 8, 40;**

(2018: Q2, IF = 2,49, 2019: Q1, IF = 3,11, 24 citations w/o selfcitations)

doi: [10.3390/diagnostics8020040](https://doi.org/10.3390/diagnostics8020040), www.mdpi.com/journal/diagnostics ,

Technique for Dielectric Measurement of Biological Tissues: Challenges and Common Practices

Abstract: Electromagnetic (EM) medical technologies are rapidly expanding worldwide for both diagnostics and therapeutics. As these technologies are low-cost and minimally invasive, they have been the focus of significant research efforts in recent years. Such technologies are often based on the assumption that there is a contrast in the dielectric properties of different tissue types or that the properties of particular tissues fall within a defined range. Thus, accurate knowledge of the dielectric properties of biological tissues is fundamental to EM medical technologies. Over the past decades, numerous studies were conducted to expand the dielectric repository of biological tissues. However, dielectric data is not yet available for every tissue type and at every temperature and frequency. For this reason, dielectric measurements may be performed by researchers who are not specialists in the acquisition of tissue dielectric properties. To this end, this paper reviews the tissue dielectric measurement process performed with an open-ended coaxial probe. Given the high number of factors, including equipment- and tissue-related confounders, that can increase the measurement uncertainty or introduce errors into the tissue dielectric data, this work discusses each step of the coaxial probe measurement procedure, highlighting common practices, challenges, and techniques for controlling and compensating for confounders.

Keywords: dielectric measurements; biological tissues; open-ended coaxial probe; equipment-related confounders; tissue-related confounders

6.1 Introduction

The interaction of electromagnetic (EM) fields with the human body is dependent on the inherent dielectric properties of each tissue. Based on these properties, electromagnetic waves are transmitted, absorbed, and reflected by biological tissues in different ratios. Accurate knowledge of these properties is crucial for dosimetry (safety) calculations and for medical diagnostic, monitoring, and therapeutic technologies.

The dielectric properties of tissues can be incorporated into highly accurate computational and physical models, and the generated preliminary data can be used to assess the technical risk, efficacy, and safety of the medical device or treatment. For instance, numerical models based on tissue dielectric parameters are used to calculate the specific absorption rate (SAR) in biological tissues. SAR levels are regularly calculated to validate the safety of many medical technologies, including magnetic resonance imaging (MRI) and implantable devices. Since SAR is a complex function of the dielectric properties of tissue, accurate knowledge of these properties are the foundation upon which SAR safety analysis is built [1,2]. Furthermore, accurate knowledge of the dielectric properties of biological tissue have prompted the development of a wide range of novel diagnostic and therapeutic technologies.

EM imaging ranges from the low-frequency Electrical Impedance Tomography (EIT) to higher-frequency Microwave Imaging (MWI). Both of these techniques rely on dielectric contrasts between organs or on contrasts between healthy and diseased, or inflamed, tissue. These imaging methods have gained significant academic and commercial interest, since both EIT and MWI are non-invasive and low-cost techniques [3–7]. While EIT is now established commercially for lung-function monitoring applications [8, 9], MWI, similarly, has made considerable progress toward clinical usage in the past two decades as tissue dielectric properties enable the differentiation of benign and malignant tissues in breast cancer imaging [10–14], the monitoring

of bladder volume in the treatment of enuresis and urinary incontinence [15,16], and the detection of stroke in intracranial imaging [17–20].

From a therapeutic perspective, knowledge of the relevant dielectric properties is used in the design and optimisation of hyperthermia (HT) [21–23], radiofrequency ablation (RFA) [24–26], and microwave ablation (MWA) systems [27–31]. Hyperthermia consists of elevating the temperature of a diseased tissue to just above a normal physiological level in order to sensitise tumour cells, making the cancerous tissue more susceptible to chemotherapy and radiotherapy [32]. Targeted HT has been demonstrated to be particularly effective in the treatment of cervical cancer, breast cancer, cancers of the head and neck, and sarcoma in adults [21] and germ cell tumours in young children [23]. In EM-based hyperthermia systems, heating is achieved by coherently adding signals at the tumour location. In order to achieve coherent summing of the waves at the appropriate location, knowledge of the wave propagation speed is required, which depends on the dielectric properties of the tissues in the region. Similarly, radiofrequency ablation (RFA) and microwave ablation (MWA) are two treatments for liver, kidney, and lung cancer [33,34]. Both methods cause the direct necrosis of disease, and the relative high frequencies allow for good selectivity in terms of targeting the cancerous tissue, while protecting the surrounding healthy tissue [35]. Knowledge of the dielectric properties of tissues in the ablation region are factored into the design of ablation probes, where they are used to optimise the probe antenna efficiency and directivity, along with the size and shape of the ablation zone [36].

Thus, an accurate knowledge of the tissue dielectric properties not only has the potential to improve SAR estimates and reduce undesired tissue heating, particularly in newly developed RF-induction powered implantable sensors, but is also of key importance for the design of novel EM-based imaging and therapeutic technologies.

Due to the fast-paced development of novel, low-cost medical technologies and wearable devices, knowledge of new dielectric tissue data may be required. Thus, dielectric data may be acquired by researchers who are not specialists in the measurement of dielectric properties. For this reason, this paper reviews the most common measurement techniques for the acquisition of dielectric properties of biological tissues and references the most relevant dielectric studies in the literature.

There are several methods to measure the dielectric properties of biological tissues, including: The transmission line, cavity, tetrapolar (or multi electrode) probe, and open-ended coaxial probe techniques. Amongst these methods, the coaxial probe technique is the most commonly used [11,29,30,37–44]. Although the dielectric measurement process with an open-ended coaxial probe appears straightforward, different confounders can result in two types of errors in the measured data: Equipment-related (or system) and tissue-related errors. System errors relate to measurement equipment choice, measurement uncertainties, and measurement calibration and validation. Tissue-related errors are due to factors including: Temperature, probe-sample contact, probe-sample pressure, sample handling procedure, in vivo versus ex vivo experiments, tissue sample properties, and heterogeneity. Historically, equipment-related errors have been reduced with the development of a standard error correction calibration and good benchmarks have been defined to reduce or compensate for tissue-related errors. However, many tissue-related errors have yet to be investigated in detail. Both equipment- and tissue-related errors are addressed in this work. In particular, this paper focuses on the most common methods and best practices used to reduce or compensate for confounders affecting each step of the open-ended coaxial probe measurement process. Confounders are

defined, here, as factors that affect the outcome (i.e., the measured dielectric properties) other than the intended cause (the actual tissue properties).

The remainder of the paper is organised as follows: Section 2 introduces the physical principles of the dielectric properties of biological tissues and summarises the most relevant works in the literature, highlighting the different aspects to consider in the process of tissue dielectric measurement. Section 3 describes the techniques used for dielectric measurement of biological tissues, and highlights why the open-ended coaxial probe method has, historically, been the most widely used for tissue measurements. In the following sections, the steps involved in an open-ended coaxial measurement are detailed. In Section 4, the standard calibration method is described and, in Section 5, the typical system validation procedure and the measurement uncertainty estimation are discussed. Tissue-related confounders are analysed in Sections 6 and 7. Lastly, the paper concludes in Section 8, with a discussion proposing methods to refine the dielectric characterisation of human tissues and improve the interpretation of both historical and new dielectric datasets. It is hoped that this paper will be a useful reference text for those who are not experts in the field of dielectric data acquisition, but who are interested in using the resulting dielectric data or EM-based medical technologies that rely on this data.

6.2 Tissue Dielectric Properties: Background and Relevant Works

This section provides the necessary theoretical background for understanding dielectric properties and their measurement. Firstly, dielectric properties are defined and their characteristics described. Then, a concise historical review of dielectric property measurements of tissues is detailed, highlighting the progress in the dielectric measurement of biological tissues to date.

6.2.1 Basics of Dielectric Properties

The dielectric properties of biological tissues (and polar materials) are defined by the complex permittivity, $\varepsilon(\omega)^*$, which describes the interaction of the tissue with an external electric field. When an electric field is applied, a charge displacement in the tissue causes dielectric polarisation. The real and the imaginary terms of the complex permittivity are related by:

$$\varepsilon(\omega)^* = \varepsilon'(\omega) - j\varepsilon''(\omega) = \varepsilon'(\omega) - j\frac{\sigma(\omega)}{\omega\varepsilon_0}, \quad (1)$$

where ω is the angular frequency. The real part of the complex permittivity, ε' , also called the “dielectric constant” or “relative permittivity”, expresses the ability of the tissue to store energy from an external electric field. The imaginary part of permittivity, ε'' , reflects the dissipative nature of the tissue, which absorbs the energy and partially converts it to heat. The conductivity, $\sigma(\omega)$, is linked to the imaginary part of the complex permittivity by the relationship defined in Equation (1).

Equation (1) expresses the dependence of complex permittivity on the frequency of the applied external electric field. In particular, at specific frequencies, polarisation occurs and contributes to the tissue dielectric behaviour [45,46]. The dielectric spectrum of a tissue is characterized by three main dispersion regions, α , β , and γ , along with other minor dispersions, including the δ dispersion. These dispersion regions reflect the mechanisms occurring in various components of the biological material. Details regarding these biophysical mechanisms are thoroughly reported in [45,46].

Mathematical functions have been developed to model the dielectric behaviour of biological tissues and polar materials. These models are generally used to fit dielectric data, thus, reducing measurement data points to closed form equations and convenient graphical representations

[11]. Dielectric models allow the calculation of the relative permittivity and conductivity values at any desired frequency within the range for which the relaxation equation is valid [47,48]. Importantly, these models allow for the dielectric properties of biological tissues to be easily incorporated into sophisticated computational models.

The most common models used to describe the electrical behaviour of either aqueous electrolytic solutions or tissues are the: Debye, Cole-Cole, and Cole-Davidson models [49]. In general, the Debye, Cole-Cole, and Cole-Davidson models can be represented collectively by the Havriliak–Negami relaxation, which is an empirical modification of the Debye relaxation model, accounting for the asymmetry and broadness of the dielectric dispersion curve:

$$\varepsilon(\omega)^* = \varepsilon_{\infty} + \frac{\varepsilon_s - \varepsilon_{\infty}}{[1 + (j\omega\tau)^{1-\alpha}]^{\beta}} + \frac{\sigma_s}{j\omega\varepsilon_0} \quad (2)$$

where ω is the angular frequency, ε_{∞} is the permittivity at infinite frequencies due to electronic polarizability, ε_s is the static (low frequency) permittivity, σ_s is the static conductivity linked to charge movements, ε_0 is the permittivity of the vacuum, α and β are empirical variables that account for the distribution of the relaxation time and the asymmetry of the relaxation time distribution, respectively, and τ is the characteristic relaxation time of the medium, which is the time necessary for the material molecules or dipoles to return to the relaxation state that was perturbed by the application of the electric field. When $\alpha = 0$ and $\beta = 1$, Equation (2) corresponds to the Debye model. For $0 < \alpha < 1$ and $\beta = 1$, Equation (2) results in the Cole-Cole equation, which accounts for the distribution of the relaxation time. Lastly, for $\alpha = 0$ and $0 < \beta < 1$, Equation (2) corresponds to the Cole-Davidson equation, which is characterised by an asymmetrically broadened distribution of relaxation times [49]. While all of these models are used for fitting polar aqueous solutions, biological tissue data is generally fitted with the Debye and Cole-Cole models.

Equation (2) describes a single relaxation; however, if the dielectric behaviour of a material is analysed across a wide frequency range, all dielectric relaxations occurring over that frequency range must be taken into account and more poles (corresponding to the different relaxation times of the material) should be introduced to adequately describe the material. Biological tissues are generally described in terms of multiple Cole-Cole poles, which is a physics-based compact representation of wideband frequency-dependent dielectric properties [47].

6.2.2 Dielectric Property Studies in the Literature

Since the late 1940s, researchers have examined the dielectric properties of human and animal tissues across different frequency ranges, often using varied measurement procedures [50–53]. In the 1980s, the dielectric relaxation processes of biological tissues were further examined and modelled [45,46], and, increasingly, the open-ended coaxial line became the most common sensor for the acquisition of the dielectric properties of animal and human tissues [38–41,54–58]. The open-ended coaxial measurement technique was preferred to the transmission line, cavity perturbation, and tetrapolar probe methods, since the open-ended coaxial technique is non-destructive and allows for ex vivo and in vivo broadband measurements [39,59–61].

In the same decade, considerable progress was made on the measurement system and procedure, and several dielectric studies were conducted. Along with the dielectric characterisation of animal and human tissues [39,54,62,63], the tissue dielectric properties were analysed as a function of their physiological properties [45,55,64]. For instance, the dependence of the dielectric properties on tissue water content at microwave frequencies was analysed [56,65], the in vivo and ex vivo dielectric properties were compared [40], the difference

between healthy and malignant tissues were examined [64,65], and the change in tissue dielectric properties post-mortem were reported [55].

A decade later, in 1996, Gabriel et al. published a comprehensive literature review reporting animal and human dielectric data across ten frequency decades, from 10 Hz to 20 GHz [66]. Dielectric data from a wide literature search was gathered and compared. Some inconsistencies were noted due to the use of different equipment and samples, and, therefore, Gabriel et al. sought to supplement these datasets with newly acquired data. Gabriel et al. completed *in vivo* and *ex vivo* animal and human tissue studies over a frequency range from 10 Hz to 20 GHz [42,47,67]. With this work, Gabriel et al. bridged gaps in the literature and consolidated the available dielectric data into one large dielectric repository. The experimental measurements were performed using three different techniques, depending on the acquisition frequency. To ensure quality, wherever possible, *in vivo* measurements on human patients were selected in preference to *ex vivo* or animal measurements. Where *ex vivo/in vitro* tissue was used, measurements were acquired as soon as possible after death. The data collected and measured by Gabriel et al. quickly became the generally accepted standard for dielectric properties of human tissues. This work was made publicly available on, firstly, the Federal Communications Commission (FCC) website [68] and on the Italian National Research Council (CNR) website, subsequently [69]. This broad availability allowed widespread use of the data among the scientific community and contributed to its diffusion.

In the subsequent years, dielectric measurement instrumentation and procedures were further improved. Specifically, the volume of the sample interrogated by the probe was investigated to accurately assign the acquired dielectric data to the actual tissue contributing to the dielectric measurement [70–72]. Based on the analysis of the probe sensing volume, precision probes were manufactured for localised dielectric spectroscopy of both low and high permittivity tissues [73].

In 2005, following an extensive measurement programme to measure the dielectric properties of several animal tissues, Peyman et al. described many measurement challenges related to the dielectric properties of biological tissues and corresponding methods to deal with them [43]. In 2006, Gabriel and Peyman reviewed tissue dielectric properties, with the aim of examining measurement uncertainties and their effect on existing dielectric measurements. The uncertainties were divided into random (“Type A”) and systematic (“Type B”), according to the guidelines defined by the National Institute of Standard and Technology (NIST) in 1994 [74,75].

In 2007, Lazebnik et al. examined the dielectric properties of breast tissue, with the aim of assessing the viability of using microwave imaging to detect early-stage breast cancer [11,76]. Through careful histological categorisation of each breast tissue sample, Lazebnik et al. found the breast to be dielectrically heterogeneous, and the dielectric contrast between fibroglandular tissue and cancerous tissue to be as little as 1.1:1 in the range between 0.5 GHz and 20 GHz. These findings were in conflict with almost all existing datasets, which had predicted considerably higher dielectric contrast (some as large as 10:1) [77,78]. The findings of Lazebnik et al. had a very significant impact in the community of researchers developing microwave breast imaging systems, since the data suggested that the dielectric contrast between healthy and cancerous tissue may be too low to clinically detect cancer using this technology. More recent works characterising healthy and cancerous breast tissue found a high variability in the properties across each tissue type and across patients, which complicates the dielectric differentiation between healthy and malignant tissue [12,58,79]. However, in Martellosio et al., a contrast in relative permittivity ranging from 1.1 to 5 was found between healthy and cancerous

breast tissue across the range of 0.5–20 GHz [79], which is in broad agreement with the results of Lazebnik et al. [11,76].

In 2014, Sugitani et al. suggested that the inconsistency in the reported dielectric properties of breast tissue may be at least partially attributed to variations in the number of cells of each tissue type (e.g., fat or tumour) within a dielectric sample [12]. The findings in Sugitani et al. underscored the need to take into consideration tissue heterogeneity and histopathology within the sensing volume when completing dielectric studies.

In order to define the sensing volume to account for histological analysis of heterogeneous biological tissues, Meaney et al. and Porter et al. examined the sensing volume of the common commercial dielectric probes and evaluated the dependence of the measured dielectric properties on the sample tissue composition [80–83].

Recently, numerous studies investigating the contrast in dielectric properties between healthy and malignant tissues have been conducted in order to improve the design of existing medical devices or

to expand the clinical application of both imaging and therapeutic devices [10,37,84–86]. In particular, a number of works investigated the dependence of the dielectric properties of biological tissues on temperature for the optimisation of therapeutic technologies, such as RF/MW ablation [26–31,35].

To summarise, over the last three decades, notable progress has been made in the improvement of dielectric measurement equipment and in the refinement of the measurement protocol, aimed at further improving existing dielectric repositories. However, today, there is still a need for additional dielectric data to cover all tissue types, temperatures, and frequency ranges. This data provides the foundation for safety studies involving electromagnetic fields and for the design or optimisation of novel medical technologies. Therefore, in the next sections, the dielectric measurement procedure is discussed in detail and, along with each step of the procedure, the corresponding confounders that can introduce error into the results are discussed. Compensation techniques for mitigating the impact of confounders are also provided.

6.3 Measurement Approaches

Different techniques have been used to measure the dielectric properties of tissue, including the transmission line and waveguide; open-ended coaxial probe; tetrapolar (or multi electrode) impedance; and perturbation cavity methods. In this section, an overview of each technique is provided, along with the known advantages and drawbacks of each. Then, the focus is on the most common method, the open-ended coaxial probe technique. This section underscores why the coaxial probe technique is the most used approach for dielectric tissue measurements. The state-of-the-art in modern open-ended coaxial probe measurement equipment is also presented.

6.3.1 Overview of Measurement Techniques

Among the measurement techniques used in previous dielectric studies, the most common methods are presented and briefly discussed in this subsection.

6.3.1.1 *Transmission Line*

In transmission line measurement methods, a sample is placed in a coaxial line or, in the case of anisotropic tissue, in a rectangular waveguide so that the field polarisation may be varied. The transmission line is connected to two ports of a Vector Network Analyser (VNA) in order to

acquire the scattering parameters (S_{11} and S_{21}) [62,87], which are then converted into the complex permittivity (dielectric properties) of the tissue. The two most commonly used conversion methods are the Nicolson-Ross-Weir (NRW) method [88,89] and the NIST iterative conversion method [90,91]. The NRW method provides a direct calculation of permittivity from the complex reflection coefficient and the complex transmission coefficient obtained from the S-parameters [88,89,91,92]. Other common conversion methods are iterative and receive the initial guess from the NRW method or users' input. The algorithm developed to implement the NIST iterative conversion method is reported in detail in Baker-Jarvis et al. [90].

The transmission line method allows measurement over a large frequency range, but only at low temperatures [87,93,94]. Waveguides are suitable for measuring larger samples (i.e., samples the size of the waveguide) at frequencies of up to 2.45 GHz, which is the frequency point normally used in microwave ablation. Smaller samples can be measured in the coaxial line, although this method also requires careful sample preparation in order to shape the sample to fit the line, and the method generally assumes that there are no air gaps in or around the sample and that the sample has smooth flat faces [95]. Thus, the transmission line method can be suitable for the measurements of biological fluids, but is unsuitable for in vivo measurements and not recommended for ex vivo measurements of semisolid or solid biological samples.

6.3.1.2 *Cavity Perturbation*

The cavity perturbation method consists of a resonant cavity that resonates at specific frequencies. The tissue samples are inserted into the cavity and analysed by measuring the resonant frequency

(f) and quality factor (Q), which are altered by inserting the tissue sample [94–98]. The tissue dielectric properties are then computed using the frequency, the Q -factor, and the sample volume. Details regarding the mathematical formulation to obtain the permittivity of the sample are reported by Campbell et al. [99]. However, the resonant frequency and quality factor are generally computed with a VNA. Since the maximum change in resonant frequency is achieved when a small perturbation occurs at the maximum intensity of the cavity mode, the cavity perturbation method requires a small sample [94,97]. Dielectric measurements performed using the cavity perturbation method can be accurate, but only provide dielectric data at a single frequency (in the upper microwave frequency range of 1–50 GHz). While the equipment needed for cavity perturbation measurements is readily available and cost-effective, the sample preparation is relatively complicated, requiring an excised tissue sample to be cut and moulded to a precise size and shape to fit into the cavity [95,97]. This process may introduce air pockets within the sample or between the sample and the cavity, loss of fluid in the tissue (which would affect its properties), and an increase in density from pushing the tissue into the cavity (which could also affect its properties) [97]. Due to the required sample size and, thus, sample preparation, biological tissue measurements with the cavity perturbation method are highly challenging.

6.3.1.3 *Tetrapolar Impedance*

Unlike the previous two techniques, the tetrapolar (or multi electrode) impedance method is non-destructive and allows for in vivo tissue measurements. The tetrapolar probe is composed of four electrodes: Two of the electrodes are driven with a current source and the other two electrodes are used for voltage measurements. The two electrode pairs are used for impedance measurements, avoiding interference from effects related to the electrode-tissue interface [100,101]. The tissue dielectric properties are easily evaluated from the measured impedance with knowledge of the sample dimensions. Although the tetrapolar probe method does not

require tissue processing and is very sensitive to tissue anisotropies [19,101], it is only suitable for specific low frequencies (in the range of 10^{-6} –100 MHz) [101]. For the tetrapolar probe technique, the electrode configuration should vary according to the interrogated tissue. In order to increase the number of applications, tetrapolar probes may be replaced by spring-loaded multi electrode probes [102]. The multiple surface electrodes permits the setting of a current pattern so that the resulting measured voltage is more sensitive to a local area and less sensitive to other regions. Multi electrode probes can provide improved bioimpedance and anisotropy measurements [102].

6.3.1.4 Open-ended Coaxial Probe

The coaxial probe technique does not suffer from many of the disadvantages associated with the techniques described above. The open-ended coaxial probe consists of a truncated section of a transmission line. The electromagnetic field propagates along the coaxial line and reflection occurs when the electromagnetic field encounters an impedance mismatch between the probe and the tissue sample. The open-ended coaxial probe measurement set-up and the probe cross-section are schematised in Figure 6.1. The reflected signals at different frequencies are measured and then converted into complex permittivity values.

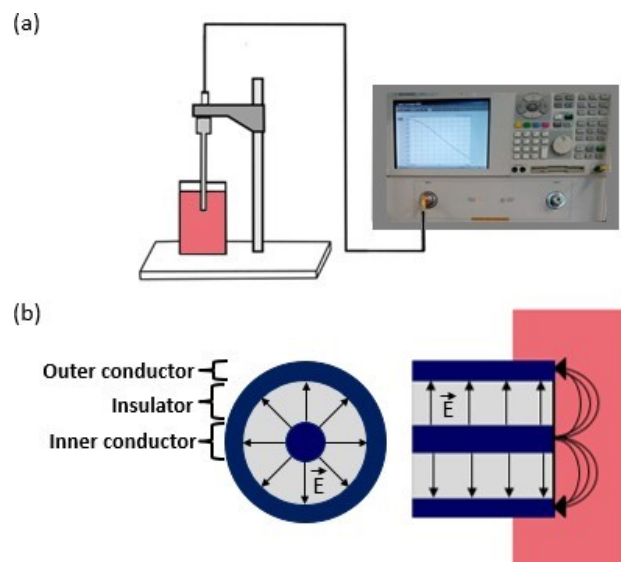


Figure 6.1, Open-ended coaxial probe technique: (a) Schematised measurement set-up, including the Vector Network Analyser (on the right), the cable connecting one port of the VNA to the coaxial probe, the probe bracket, and the liquid sample being measured; (b) top and side cross-sections of the coaxial probe, with electric field orientation indicated.

Different methods have been developed to convert the measured reflection coefficient to permittivity [60,103–107]. However, today, this process is generally done automatically by software embedded in the VNA [108]. Therefore, details on the various methods are not discussed in detail here, but more information can be found in [103–107,109–111].

The open-ended coaxial probe has become the most commonly used method to measure the dielectric properties of tissues for several reasons: The method is simple; sample handling is minimal and non-destructive; and both *ex vivo* and *in vivo* measurements over a broad frequency range are possible [39,42,43,72,94]. However, the open-ended coaxial method

assumes a homogeneous sample that is in good contact with the probe; therefore, air bubbles and uneven sample surfaces can result in inaccurate measurements [95], and heterogeneous samples present a particular challenge. There are also limits to the magnitudes of material properties that can be measured reliably [95]. The limits of what can be measured depend on a number of factors, including the probe design and materials (and, therefore, its impedance), precision of the probe fabrication procedure, calibration procedure (standards used), and the capabilities of the measurement device (i.e., the VNA). Furthermore, what is classified as a “reliable measurement” depends on the experiment and the required accuracy. Although theoretical limits of the measurement set up can be estimated analytically, they are generally estimated experimentally by measuring materials (usually liquids) with different extreme values of relative permittivity and conductivity. Then, the accuracy of the measurement can be estimated in different ranges of complex permittivity and it can be determined if the accuracy is appropriate for the experiment of interest.

Overall, many challenges associated with tissue dielectric property measurements may arise in each of the above measurement techniques, for example, issues related to temperature change and tissue heterogeneity. Since the coaxial probe technique is by far the most commonly used method for tissue measurements [10–12,39–42,44,59,60,62,112,113], it will be examined in more detail in the subsequent sections.

6.3.2 Evolution of the Coaxial Probe Design and Fabrication

In the 1980s and 1990s, researchers conducting studies on dielectric measurements of biological tissues focused on probe design and fabrication, system development, and systemic error correction techniques [39,40,60–62,73]. The majority of the custom probes were fabricated from 50 Ω semi-rigid coaxial cables [39,40,60–62,94]. Probes were customised depending on the type and size of the tissue sample to be investigated and on the desired frequency range of the dielectric properties study.

Several custom-made probes were made of metal and Teflon [39,40,61,62]. Burdette et al. used a 2.1 mm diameter probe to perform *in vivo* and *ex vivo* measurement on animal tissue over the frequency range 0.1–10 GHz. This probe had a flange (i.e., a ground plane) to contain the electromagnetic field at the tip [39]. Kraszewski et al. performed *in vivo* animal measurements over the frequencies 0.1–12 GHz using a Teflon-filled metal probe with a 3.2 mm external diameter [40]. Gabriel et al. used two Teflon-filled metal probes for *in vivo* and *ex vivo* animal studies in order to acquire tissue dielectric properties at both low and high frequencies [42]. The probe used in the low frequency range (10^{-4} –200 MHz) had an external diameter of about 10 mm and the smaller probe, used for dielectric measurements at the frequency range between (0.2–20 GHz), had an external diameter of 2.9 mm [109]. Larger probes require a larger sample size due to the increased sensing volume (i.e., the region of the tissue that is interrogated by the electric field of the probe). In both Burdette et al. and Gabriel et al., the probe tips of the inner and outer conductors were plated with an inert metal, such as gold and platinum, to modify the effect of electrode polarisation, which is a manifestation of chemical reactions between the probe and the electrolytes (water molecules and hydrated ions) in the tissue [39,42]. Specifically, this plating process shifts the electrode polarisation, normally occurring at low frequencies, to even lower frequencies [39,46,109]. Popovic et al. reported that Teflon-filled copper probes, usually used for broadband reflection coefficient measurements, can cause inaccurate measurements because the probe aperture deteriorates easily and mechanical flaws can occur. The effects of small mechanical imperfections at the probe tip were quantified by the measured reflection coefficient and it was found that mechanical flaws at the probe tip can

impact measurements by altering the reflection coefficient by up to 30% [114]. Notably, Teflon-filled copper probes do not meet bio-compatibility requirements nor can they be autoclaved (steam sterilised), both of which are required for safe in vivo measurements on human patients [73].

More recently, borosilicate glass-filled, stainless-steel, open-ended coaxial probes were designed and fabricated [73,115]. The use of thermally constant and matched, inert, refractory materials made the probe biocompatible and suitable for high-temperature sterilisation [73].

Over the last decade, a growing number of dielectric studies have been conducted using commercial probes [10,44,84,86]. Modern commercial probes are accurate [115], yet require specific sample dimensions and characteristics. In particular, Keysight probes, including the slim form probe, the performance probe, and the high temperature probe, have been used in most of the recent tissue dielectric studies [12,44,79,86,116]. Out of these, the slim form probe is a common choice for tissue measurements due to its small diameter and the fact that it can be steam-sterilised and, thus, used in vivo. The tissue dielectric measurements performed using these commercial probes are summarised in Table 6.1.

As the open-ended coaxial probe has been demonstrated to be the most applicable to measuring the dielectric properties of biological tissues, the remainder of this work will focus on the dielectric measurement process using this probe, from system calibration to biological sample preparation and analysis. In the next section, the calibration procedure for open-ended coaxial probes is discussed.

Table 6.1. Use of the commercial probe in recent works. Studies involving breast tissues are shaded in grey. The others involve liver tissues, apart from the porcine skin study in Karacolak et al. [116]. In the column “Relative permittivity range”, the extreme values in relative permittivity are reported from lower to higher frequencies.

Recent Works	Probe	Frequency [GHz]	Tissue Type	Sample Size	Relative Permittivity Range	Conductivity Range [S/m]
Halter et al. (2009) [10]	Slim form with 2.2 mm diameter (in vivo) High temperature with 19 mm flange (ex vivo)	0.1–8.5	Ex vivo and in vivo Breast tumour (human)	5 mm thick	In vivo breast tissue: 95–45 Ex vivo breast tissue: 50–35	In vivo breast tissue: 0.1–10 Ex vivo breast tissue: 0.1–8
Karacolak et al. (2012) [116]	High temperature with 19 mm flange	0.3–3	Ex vivo skin (porcine)	45 × 45 × 4 mm ³	50–36	0.4–2.2
Lopresto et al. (2012) [29]	Slim form with 2.2 mm diameter	2.45	Ex vivo liver tissue (bovine)	20 × 20 × 50 mm ³	44.98–26.11 (temperature incremented from 15 °C to 98.9 °C, then decremented to 39.6 °C)	1.79–1.19 (temperature incremented from 15 °C to 98.9 °C, then decremented to 39.6 °C)
Sabouni et al. (2013) [86]	Performance with 9.5 mm diameter	0.5–20	Ex vivo breast tissue (human)	N/A	Breast tissue: 63–35 Fibroglandular breast tissue: 40–20	Breast tissue: 0.2–32 Fibroglandular breast tissue: 0.2–16.3
Abdilla et al. (2013) [44]	Slim form with 2.2 mm diameter	0.5–50	Ex vivo muscle and liver (bovine, porcine)	60 × 60 × 40 mm ³	Muscle tissue: 58–18 Liver tissue: 51–15	N/A (Loss factor for muscle/liver tissue: 32–10)
Sugitani et al. (2014) [12]	Slim form with 2.2 mm diameter	0.5–20	Ex vivo breast tumour (human)	50–300 mm diameter	Breast tumour tissue: 65–22 Breast fibroglandular tissue: 40–18 Breast fat tissue: 12–6	Breast tumour tissue: 0.1–25 Breast fibroglandular tissue: 0.1–12 Breast fat tissue: 0.1–3
Peyman et al. (2015) [84]	Slim form with 2.2 mm diameter	0.1–5	Ex vivo liver tissue (human)	20 mm thick	Liver normal tissue: 68–43 Liver tumour tissue: 68–32	Liver normal/tumour tissue: 0.7–5
Martellosio et al. (2017) [79]	Slim form with 2.2 mm diameter	0.5–50	Ex vivo breast tumour (human)	6 mm thick volume between 700 mm ³ and 1500 mm ³	Breast normal tissue: 64–3 Breast tumour tissue: 69–9	N/A (Breast normal tissue imaginary part: 41–0.1; Breast tumour tissue imaginary part: 45–4)

6.4 Calibration and Confounders


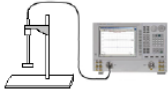

A standard calibration procedure, involving both the coaxial probe and the VNA, must be performed before recording dielectric measurements [40,60,62,117]. In this section, a description of the calibration process is provided, followed by an in-depth analysis of the related confounders.

6.4.1 Standard Calibration

In general, coaxial probe measurements use a three load standard calibration procedure for one-port error correction. Any three different standard materials can be used for calibration, as long as the dielectric properties of those standards are well known [117–119]. The choice of standard materials to use may be based on ease of use, availability, or similarity to the materials under test [94,117]. The three most common standards used for coaxial probe calibration are: Open circuit, short circuit, and a broadband load [114,115]. We note that the use of the term

“broadband load” here does not indicate a perfectly matched load, but rather, the broadband load can be any liquid with known dielectric properties. The calibration is performed at the reference plane of the probe, while the probe is connected to the VNA. The probe may be connected directly to the VNA or through a phase-stable cable. The calibration procedure aims to find a relation between the measured complex reflection coefficient and the expected one. This procedure allows for all post-calibration measurement data to be corrected [120]. If performed correctly, a good calibration procedure results in reliable measurements. The quality of the calibration depends on the accuracy in the measurements of the three standards and on the level of control over the factors that can affect the process. In the following subsection a list of the calibration steps required to reduce the confounders is reported. In addition, the confounders and methods for their compensation are summarised in Table 6.2.

Table 6.2, The standard calibration process: Common errors or confounders that occur for each step in the calibration process, along with the possible correction or compensation techniques. The open circuit, short circuit, and a liquid load material are shown as the three calibration standards.

Calibration Steps	Error or Confounder	Action for Correction or Compensation
Equipment set-up	<ul style="list-style-type: none"> • Environmental parameter change [95] • Probe contamination [27,37,39,121] • Imperfect connection [39] • Cable movement [43,76,80,115] 	<ul style="list-style-type: none"> • Control environmental parameters [113,122] • Inspect and clean probe [29,41–43] • Check connections [39] • Fixing cable position (if not phase-stable) [29,44,86]
 Open	<ul style="list-style-type: none"> • Particles on probe tip [95] 	<ul style="list-style-type: none"> • Cleaning probe [29,41–43] • Checking the Smith Chart [123] to ensure open-circuit impedance is being measured
 Short	<ul style="list-style-type: none"> • Poor probe-short block contact [95] 	<ul style="list-style-type: none"> • Cleaning short block and probe [95] • Reposition or re-contact short block with probe [95] • Checking the Smith chart [123] to ensure short-circuit impedance is being measured
 Load	<ul style="list-style-type: none"> • Accuracy of liquid model [94,117] • Liquid temperature [43,94,124,125] • Air bubbles [48,71,126] • Liquid contamination [43] • Probe position in liquid [71] 	<ul style="list-style-type: none"> • Deionised water model has best accuracy [117] • Monitor or control temperature [29,43,44,95,121] • Re-immers probe in liquid [95] • Limit exposure to air [43] • Place probe distant from beaker sides [71]

6.4.2 Calibration Procedure and Confounders

6.4.2.1 Equipment Set-Up and Confounders

Before performing the calibration, environmental parameters, such as temperature, pressure, and humidity, should be controlled or monitored [122,127] because environmental changes may impact measurement results [74]. Furthermore, system components should be checked [39], the probe tip cleaned and verified by visual inspection [29,41–43], and the cable (if not phase-stable) fixed in place [29,44,86] as imperfect connections [39], probe contamination [27,37,39,121], and cable movement [10,27,43,44,76,80,86, 95,115] can all result in a poor calibration and, thus, unreliable measurements.

6.4.2.2 Signal Settings and Confounders

Prior to calibration, the frequency range needs to be selected based on the planned experiment. Subsequently, the number of acquisition frequency points must be defined. Frequency points may be equidistant according to a linear or a logarithmic scale. The use of a logarithmic scale can be advantageous when data is acquired over a larger frequency range as there will be more points taken at the frequency points where the largest change in dielectric properties occurs (due to dispersions) [128]. The signal power and measurement bandwidth must also be selected in the VNA software. The number of points and bandwidth requires a trade-off between the measurement accuracy and speed of data collection.

6.4.2.3 *Measurement of the Three Standards and Confounders*

Once the measurement settings are selected, the calibration measurements of the open-circuit, short-circuit, and broadband load can be performed. The common errors and confounders likely to occur during the calibration process are highlighted in Table 6.2, along with the recommended correction and compensation techniques. As noted in the table, while performing calibration, (when using modern VNAs) visualisation of the complex impedance on the VNA Smith chart is key to identifying the unwanted presence of particles at the probe tip and confirming the quality of the open or short circuit [56,95]. In particular, having a good quality short circuit is vital to a successful calibration [94]. Therefore, proper contact between the short and the probe must be ensured prior to completing the calibration. Other than this, the open and short measurements are relatively straightforward and do not require any additional consideration. In the case that the VNA does not allow visualisation of the Smith chart during calibration, the quality of the calibration can then be verified by performing the validation procedure, as described in Section 5.

Conversely, several confounders can introduce error into the load measurement. Different liquids have been examined as potential load materials. The permittivity of the standard liquid should be selected such that the complex impedance of the load is considerably different from the other two standards [129]. The most typical liquid used as a load is deionised (DI) water [12,27,80,86,116,130]. Polar liquids (for example, ethanol, methanol, and saline) also meet the requirements [129] and exhibit high conductivity and permittivity as a function of frequency. Nyshadham et al. examined the effect of the uncertainty of the models of different standard materials on the uncertainty of the measured permittivity [117]. In this study, different liquids (having different models) were used for calibration and it was verified that DI water has smaller uncertainties in the Debye model than that of other standard liquids (in other words, the dielectric properties of deionised water are the most well-known and well-characterised) [117]. Indeed, the accuracy of the model represents one of the confounders affecting the calibration procedure and the uncertainty of the measured permittivity. Specifically, a quantitative analysis that examined the impact of errors in the model of one of the calibration standards (in this case, acetone) found that model errors of 2% induced a similar magnitude of error into the measured relative permittivity [131]. However, despite the impact of model uncertainties, the best calibration material depends on the measurement scenario as the uncertainty will be lower for materials measured with properties similar to those of the calibration material.

Temperature of the Liquid

During the calibration process, the temperature of the load liquid needs to be maintained and monitored, since dielectric parameters are temperature-dependent [43,94,124,125]. The permittivity of liquids vary by up to 2.2% per degree Celsius [125]. The measurement of deionised water, or any standard liquid, as a calibration load may be performed at room temperature or at any fixed temperature. In the first case, the liquid temperature can be monitored using a thermometer [95]. In the second case, the temperature may be maintained using a water bath [29,43,44,121]. In addition, if the temperature of the liquid is different from the temperature of the probe, it is recommended to wait for the temperature to stabilise before proceeding with the measurement. We note that this information on the liquid temperature also applies to the liquid used in the validation step.

Other Confounders in the Liquid Measurement

Aside from the liquid temperature and model accuracy, other confounders, such as liquid contamination [43], air bubbles between the probe and the liquid [48,71,95,126], and probe position in the liquid-filled beaker [71], have been investigated. These confounders affect the load liquid used during calibration and the liquid used in the validation step equally—indeed, the same types of reference liquids can be used either for calibration or for validation.

In order to avoid any impurity in the water, the beaker filled with liquid should be kept closed [43]. The presence of air bubbles between the probe tip and the standard liquid can result in deviations in the dielectric measurement data by up to 20% due to the fact that the material within the sensing region is then a mixture of air and liquid [126]. A transparent beaker is recommended so that air bubbles can clearly be seen. If bubbles are present, they need to be removed prior to measurement. This may be completed by gently tapping the probe tip on the bottom of the beaker, or lowering the beaker away from the liquid and then re-immersing it on an angle [95]. A soft brush (non-metallic, to avoid scratches) may also be used to remove any bubbles without having to move the probe or the beaker. In addition, the probe should be immersed in the liquid and positioned in the beaker such that the liquid is the only material within the probe sensing volume. Accurate positioning avoids undesirable reflections from the beaker walls. Hagl et al. provided a process for finding the minimum distance between the probe and the beaker sides according to the probe size; these distances also depend on the properties of the liquid material in the beaker and the frequency range of interest [71].

6.4.3 Confounders Introduced in the System after Calibration

Following the calibration procedure, two additional system confounders can introduce errors in dielectric measurements: VNA drift over time and cable movement, although the movement of a phase-stable cable should not compromise the performance of the system [10,27,43,44,76,80,86,115]. The system drift should be characterised and taken into account in the measured dielectric data [43,44]. This factor can be quantified by taking several measurements on a standard liquid at defined time instants in the period after calibration [43]. When a cable that is not phase-stable is moved, given the difficulty in precisely characterising the systematic error introduced by the cable movement, a new calibration is required. However, low loss and phase-stable cables should be used to minimise the impact of the error of the cable stability on the results [71,76,94]. In some works, the cable was fixed in place (using adhesive tape) to limit the effect of the cable movement in the dielectric data [29,44,86]. An alternative approach may be to replace the cable with a right-angle connector, when the rigid set-up does not overly restrict dielectric data acquisition [128].

After each calibration, it is good practice to first confirm proper calibration by re-measuring one of the calibration standards, commonly the short [44]. Note that re-measuring the properties of materials used during calibration does not guarantee that the system is functioning error-free, it just indicates that the calibration error-correction algorithms were successfully applied. Thus, a measurement of a known liquid, other than the one used in calibration, is also required in order to validate the accuracy of the calibration. Details about the validation procedure and the measurement uncertainty calculation are discussed in the next section.

6.5 Validation and Measurement Uncertainty

The validation procedure consists of measuring the dielectric properties of a known reference liquid. To ensure that the measurements are accurate in materials with different properties, the validation material should not be the one used during the calibration (i.e., typically not deionized water). Validation enables determination of the quality of the calibration and the monitoring

of systematic errors [43,44,75], such as VNA drift and noise due to cable movement [43]. Thus, it is good practice to perform validation immediately following calibration [39,43,71,121,132] and after acquiring a set of tissue dielectric data [76]. The validation should also be completed whenever anomalies are observed in the dielectric data of the investigated material in order to isolate the source of error. For instance, if the same anomalies are observed in the reference liquid dielectric trace, the error is due to changes in the system and a new calibration is needed; if the anomalies are not evident in the liquid trace, the error is sample-related and further investigation is needed to identify the source of the error.

During the validation procedure, monitoring or controlling the temperature of the liquid during the validation process is required, since the dielectric properties of reference liquids are temperature- and frequency-dependent [43,44,132].

Although system validation is a simple procedure, several confounders can introduce errors in the process. The factors that affect the validation quality are similar to those present in the load measurement during the calibration procedure. Thus, details regarding confounders in the liquid dielectric measurement and how they are addressed can be found in the previous section.

In this section, after describing the most common validation liquids, the role of the validation procedure in the calculation of the uncertainty of dielectric data is detailed.

6.5.1 Validation Liquids: Models, and Their Advantages and Disadvantages

Alcohols and saline are the most common polar reference liquids [39,71,75,76,125,133]. Polar solutions are particularly suitable as validation liquids because they have comparatively high relative permittivity and high dielectric loss at radio and microwave frequencies. Both the relative permittivity and conductivity have a strong frequency dependence, which is a feature of the pronounced molecular dielectric relaxation behaviour [94]. Liquids, in general, are selected for validation purposes as they are homogeneous and are free of many of the confounders affecting solids or semi-solids (e.g., incorrect probe-sample contact, inconsistent probe-sample pressure).

6.5.1.1 Alcohols

Methanol, ethanol, ethanediol, and butanol are the types of alcohols generally used to characterise the system and calculate the uncertainty in the dielectric measurements [44,71,72,76,117,125,132] prior to tissue measurements. Methanol, ethanol, and butanol, in particular, are used as standard liquids because they represent the high, intermediate, and low dielectric property values, respectively, within the range of those expected for human breast tissues at microwave frequencies [71,72,76,132]. They also have well-established permittivity models [72,76,125,132]. Ethanediol, which has also been modelled in the microwave frequency range [44,132–134], has a static permittivity about half that of pure water [134]. Standard methods for obtaining the known dielectric property values for each of these alcohols have been detailed thoroughly [132].

Although alcohols present properties similar to those of biological tissues at microwave frequencies (0.5–20 GHz), there are some constraints that must be taken into account when using them as reference liquids. For instance, the alcohol models are accurate in restricted frequency ranges and at discrete temperatures only [117,124,132,134,135]. Furthermore, the dielectric properties of alcohols can change during storage and handling. For example, methanol has very low vapour pressure and evaporates rapidly. This can contribute to a decrease in the liquid temperature and, consequently, to a dielectric property change over the course of just a few minutes when exposed to air [72,132]. In order to minimise these effects, the dielectric

properties of methanol should be measured almost immediately after it is poured into the measurement beaker [72] and the temperature should be kept constant and monitored. Lastly, since alcohols are inflammable and have an acute inhalation toxicity, working with these liquids requires a safety protocol, such as the use of special fire-proof storage cabinets and handling under a fumehood [132].

6.5.1.2 *Saline*

The dielectric properties of different concentrations of NaCl (saline) solutions at various temperatures have been modelled in the microwave frequency range [49,75,136–138]. Specifically, Stogryn provided models in the gigahertz range for computing the complex permittivity of saline as a function of temperature and concentration (between 0.25 M and 0.5 M) in order to allow these liquids to be used as references [136]. More recent models, based on extended experimental data, are now available for solutions having concentrations between 0.001 mol/L and 5 mol/L in the frequency range of 0.10–40 GHz, for any temperature between 0 °C and 60 °C [49,130,133,137,138]. Although alcohol models are, generally, more accurate than saline models, saline solutions are the most convenient reference liquids used [133].

Among all of the saline solutions, 0.1 M NaCl solution is the most commonly used reference liquid to assess the uncertainty in measuring the dielectric properties of biological materials, since it has similar dielectric properties to those of biological tissues [43,44,133]. Furthermore, 0.1 M NaCl is stable in temperature and electrical properties during storage and handling. At room temperature, saline does not evaporate quickly like alcohols. Saline solutions are also straightforward to prepare (hence, commercially-bought solutions are cost-effective) [133] and to use. Saline solutions are also less dangerous than alcohols and, thus, they do not require the use of fire-proof storage cabinets or handling under a fumehood. For 0.1 M NaCl, models that cover relatively wide frequency and temperature ranges are available [133]. However, saline may not be the best choice as a validation liquid when DI water is used as calibration, since these two liquids have very similar dielectric properties in the microwave range. Furthermore, due to poor traceability of the data used to obtain the models in [133] (since the data was acquired with only a single measurement system and a single measurement technique, and then compared to reference data measured under unknown conditions), the saline models are likely not as accurate as the models for alcohols.

To this extent, future studies aimed at improving the reliability and accuracy of saline models have the potential to support dielectric data validation and uncertainty calculations.

6.5.1.3 *Other Liquids*

Several other liquids, such as formamide [75,84,134,137], DI water [94,124,132], dimethyl sulphoxide (DMSO) [94,132,139], and acetone [94,132,140], have been used as reference liquids.

Formamide is a polar organic solvent, which has a relative permittivity of approximately 110 at low frequencies that drops down to a high-frequency value of around 7 [134] (when handled at room temperature). The temperature-dependent model for characterising the dielectric properties of formamide across the microwave frequency range was developed by Jordan et al. and, more recently, by Barthel et al. using waveguide interferometry [75,134,135]. The parameters of different models were found at discrete temperatures in the frequency range between 0.2 GHz and 89 GHz. The reliability of the model in Jordan et al. is affected by the limited discrete frequency points used in the dielectric measurements from which the model has been obtained [134]. In both Jordan et al. and Barthel et al., the dielectric models are available only for

limited discrete temperatures [134,135]. Also, since formamide is toxic, a custom handling protocol is required.

Table 6.3, Reference liquid properties, available models, and storage and handling procedures (where f = frequency, T = temperature).

Liquid	Models	Storage and Handling
Methanol (alcohol with intermediate permittivity values similar to breast tissue)	Debye model [132]: <ul style="list-style-type: none"> f = 0.1–5 GHz T = [10 °C, 50 °C], 5 °C increments 	Inflammable and acute inhalation toxicity. Fire-proof storage cabinets required. Handling in fumehood required.
	Cole-Cole model [134]: <ul style="list-style-type: none"> f = 0.01–70 GHz T = [10 °C, 40 °C], 10 °C increments 	Rapid evaporation may occur and should be avoided.
Ethanediol (alcohol with high permittivity values similar to breast glandular tissue)	Cole-Davidson model [132]: <ul style="list-style-type: none"> f = 0.1–5 GHz T = [10 °C, 50 °C], 5 °C increments 	Inflammable and acute inhalation toxicity. Fire-proof storage cabinets required. Handling in fumehood required. Ethanediol is hygroscopic and when it evaporates the liquid temperature increases, causing an increase in relative permittivity [132].
Ethanol (alcohol with intermediate permittivity values similar to breast tissue)	Debye-Γ model [132]: <ul style="list-style-type: none"> f = 0.1–5 GHz T = [10 °C, 50 °C], 5 °C increments 	Inflammable and acute inhalation toxicity. Fire-proof storage cabinets required. Handling in fumehood required.
Butanol (alcohol with low permittivity values similar to fat tissue)	Double Debye model [132]: <ul style="list-style-type: none"> f = 0.1–5 GHz T = [10 °C, 40 °C], 5 °C increments 	Inflammable and acute inhalation toxicity. Fire-proof storage cabinets required. Handling in fumehood required.
	Cole-Cole model [133]: <ul style="list-style-type: none"> Concentrations = [0.001 mol/l, 5 mol/l] f = 0.13–20 GHz T = [5 °C, 35 °C] (any intermediate T) 	
Saline (NaCl) (polar liquid having dielectric properties similar to biological tissues)	Cole-Davidson model [49]: <ul style="list-style-type: none"> Concentrations = [0.001 mol/l, 1 mol/l] f = 0.1–40 GHz T = 17 temperatures in the interval [10 °C, 60 °C]: 10 °C, 20 °C, increments of 2 °C in [24 °C, 50 °C], and 60 °C. 	Storage in sealed containers. No special handling required.
Formamide (polar organic solvent having wide permittivity spectrum at microwave frequencies)	Cole-Davidson model [135]: <ul style="list-style-type: none"> f = 0.2–89 GHz T = [10 °C, 25 °C], 5 °C increments T = [25 °C, 65 °C], 10 °C increments 	Toxic through inhalation, oral, or skin exposure. Fire-proof storage cabinets required. Handling in fumehood required.
DI water (polar liquid having well-known modelled properties)	Debye model [124]: <ul style="list-style-type: none"> f = 1.1–57 GHz T = [−4.1 °C, 60 °C] (any intermediate T) 	Storage in sealed containers. No special handling required.
Dimethyl sulphoxide (DMSO) (highly polar organic reagent having high permittivity)	Debye model [132]: <ul style="list-style-type: none"> f = 0.1–5 GHz T = [10 °C, 50 °C], 5 °C increments 	DMSO is exceptionally hygroscopic and needs to be measured as soon as the container is opened [132].
	Cole-Davidson model [139]: <ul style="list-style-type: none"> f = 0.001–40 GHz T = 25 °C 	
Acetone (polar organic solvent having intermediate permittivity values)	Static permittivity (since acetone has very high relaxation frequency) [132]: <ul style="list-style-type: none"> f = 0.1–5 GHz T = [10 °C, 50 °C], 5 °C increments 	Acetone boiling point is at 56 °C [132].
	Budo model/confined rotator models [140]: <ul style="list-style-type: none"> f = 50–310 GHz T = 20 °C 	

When it is not used as the broadband load in the calibration procedure, DI water represents an advantageous validation liquid [117,124]. In fact, DI water has dispersive properties similar to those of biological tissues and has been accurately modelled in the microwave frequency range for any temperature between −4.1 °C and 60 °C [124]. DI water also has the advantage of being a liquid and does not require special handling.

Dimethyl sulphoxide (DMSO) is a highly polar organic reagent that has a high relaxation frequency. DMSO has relative permittivity values similar to those of muscle tissues. Dielectric models for DMSO have been developed that cover a wide frequency range [139] and different temperatures [132]. DMSO is hygroscopic [94,132] and when it evaporates the liquid temperature increases, causing an increase in relative permittivity values [132]. Therefore, like with many alcohols, care should be taken to keep the liquid in a closed container as much as possible.

Acetone is a polar organic solvent that has intermediate permittivity values, which have been modelled only in the upper microwave frequency range [140]. Acetone requires special handling because it has a boiling point of 56 °C and has the potential to soften some plastics [94,132].

Liquid properties and information about available models and storage/handling procedure related to the most common categories of reference liquids are reported in Table 6.3. The column “Models” contains the most referenced models, i.e., those which cover the widest frequency range and largest, most continuous temperature interval.

6.5.2 Uncertainty Calculation

It is always good practice to report uncertainty along with measured values. However, in dielectric measurement studies, the definitions used for uncertainty, including how they are calculated and reported, have varied widely.

Today, the uncertainty of measurements is generally calculated according to the guidelines defined by the National Institute of Standard and Technology (NIST) [43,44,75]. Multiple measurements performed on the same material of known dielectric properties enables determination of uncertainty of the measurement system in terms of the repeatability and accuracy. Considering the definition of uncertainty reported in [43,75], the repeatability of the measurement may be expressed quantitatively in terms of the characteristics (e.g., standard deviation) of data repeatedly acquired under the same measurement condition, as defined also in [74]; while the accuracy may be defined as the average percentage difference between the dielectric properties of the acquired data and those of the model [43,44]. These definitions represent practical methods of calculating these parameters. In this way, the repeatability varies between measurements and gives the extent of random errors, while the accuracy is constant across measurements.

The uncertainties in repeatability and accuracy both contribute to the total uncertainty in the dielectric measurements [43,44,74,75]. For example, the combined standard uncertainty may be calculated as the root sum squared of the standard uncertainties [43,75]. In Peyman et al., the standard uncertainties associated with Type A errors (repeatability), Type B errors (in the calibration and measurement of the reference liquids), VNA drift, and cable variations, were estimated and included in the combined standard uncertainty calculation [43]. These uncertainties were determined for 0.1 M NaCl and, undoubtedly, tissue measurements will be impacted by more and/or different uncertainties. Alternatively, in Gregory et al., uncertainties associated with specific input parameters were thoroughly evaluated by means of Monte Carlo modelling [141]. Notably, this modelling technique also enables estimation of uncertainties in measurement scenarios when there are no suitable reference materials available (e.g., with similar material properties or frequency range) [141].

According to the NIST guidelines, the best practice for expressing uncertainty is to report the mean measured value along with a confidence interval (CI) of 95% [74]. For dielectric measurements,

one may wish to present these parameters separately for both the real and imaginary parts of permittivity.

In the next section, techniques related to minimisation or compensation of tissue-related confounders are described.

6.6 Tissue Sample Preparation and Measurement Procedure

Tissue-related confounders may be the major cause of measurement uncertainty, since the total combined uncertainty for measurements on liquids is relatively small compared to that of tissue measurements [43]. Uncertainties associated with measuring tissue properties seem to be primarily related to the complex structure of biological tissues [39,43,122].

In order to reduce tissue-related confounders, it is useful to plan each set of measurements according to the experimental goal. The first step involves the choice of the target animals (since their age or weight could affect the dielectric properties [43,122,142]) and the sample tissue type. Aside from the source species, the number of samples should be chosen based on the scientific question. The following steps include the analysis of the various tissue-related confounders and the evaluation of different methods that aim to reduce or compensate for these confounders.

In the next subsection, the confounders related to probe choice, sample preparation, and handling are first described. Then, a discussion of the confounders that need to be considered during the measurement procedure is provided.

6.6.1 Probe Selection Considerations

Open-ended coaxial probes are suitable for use with materials that are liquid or semi-solid [95], homogeneous [95], have flat surfaces [66,95], and have a semi-infinite thickness [39,43,95]. Tissues are generally semi-solid (with the exception of bone), but they are not always homogeneous or have flat surfaces, and tissue samples that are much thicker and larger than the probe tip are not always easy to prepare. Hence, probe selection is affected by three main biological factors: Sample size, heterogeneity, and tissue surface. The desired frequency range of the measurement may also impact the choice of the probe.

6.6.1.1 *Sample Size, Sensing Volume, and Heterogeneity*

Dielectric spectroscopy techniques permit the acquisition of the average complex permittivity of the interrogated volume. Thus, the probe should be selected such that the sensing volume only contains the tissue sample of interest and no other material. Since probes with a small diameter have smaller sensing volumes compared to large flanged probes, the sample size has to be taken into account and compared to the sensing volume of the probe [71,72,76].

The sensing volume may be evaluated by performing preliminary experiments with different combinations of materials. To this end, Meaney et al. analysed the dielectric property change in two-layer materials, consisting of saline or DI water with Teflon or acrylic, by varying the thickness of the liquid layer to determine the influence of materials at different depths on the measurement. The experimental results suggested that the dielectric properties are dominantly influenced by the material present within only the first 200–400 microns from the probe tip, and that this depth did not vary significantly across frequency or material properties [80]. This was a key finding as previous studies had assumed a much larger region on the order of several millimetres [11]. While Meaney et al. and Hagl et al. both investigated the depth into a tissue that contributes to the dielectric measurement, they defined the depth parameter differently [71,80]. More recently, Porter et al. demonstrated how different definitions of the sensing depth can

impact the determined sensing depth value and highlighted that, for some definitions, the value does depend on the frequency and dielectric properties of the tissues occupying the sensing volume [83]. The work of Porter et al. also confirmed the findings of Meaney et al., in that the experimental results demonstrated that the tissue in contact with the probe has a greater impact on the measured dielectric properties than deeper tissues [82]. Nevertheless, because the sensing volume may be affected by the intrinsic dielectric properties of the investigated sample, further experiments involving the analysis of materials with more complex structures across both radial and axial directions are needed in order to define the sensing volume accurately for complex tissue samples.

Heterogeneity of biological samples is a further factor to consider when choosing a probe, since it is challenging to determine the tissue-specific dielectric properties in an extended heterogeneous volume interrogated by the probe [39,43,76]. To date, the impact of tissue heterogeneity with only simplified configurations has been thoroughly modelled. For example, in Chen et al., it was demonstrated that, for bilayer materials, the permittivity of either layer can be calculated from the reflection coefficient without the need for information on the thickness of the first layer or the probe capacitances [143]. Models for the effective dielectric properties of bilayer materials, in general and in particular for coaxial probes, have also been presented in [107]. These results were also extended to a general multilayer material scenario [107]. Furthermore, Huclova et al. used a numerical three layer skin model to examine how variations in the layer properties (including thickness and permittivity), impact the dielectric measurement across frequency [144]. More complex heterogeneities have yet to be thoroughly investigated or quantified. Specific challenges associated with heterogeneous tissues (aside from their impact on probe selection) are discussed in Section 7.

6.6.1.2 Tissue Surface Characteristics

In addition to the sample size and heterogeneity, the quality of the tissue surface is another consideration when selecting the appropriate probe to use. Surface irregularities may contribute to inadequate probe-tissue contact and poor repeatability of dielectric measurements [42,43,60]. Characterisation of the tissue surface permits the identification of the tissue area or points that are most suitable for the acquisition of dielectric information [145]. For instance, thick samples and even surfaces are preferable to thin and uneven surfaces in order to ensure good probe contact with the tissue sample [42,60,95]. From the authors' experience, the use of a smaller probe on uneven tissue surfaces results in more reliable measurements, especially if these areas are limited or spatially restricted. Lower uncertainty in the measurements from smaller probes on uneven surfaces may be attributed to smaller forces being applied on smaller surfaces. Indeed, large uneven surfaces require the application of higher forces (and, consequently, higher pressures) to prevent the presence of air gaps between the probe and the tissue. An increased probe-sample pressure may cause fluid accumulation at the probe tip [39,43] or tissue damage [95], both of which can affect the tissue dielectric properties and lead to inaccurate data.

In summary, the probe should be selected not only on the basis of the probe characteristics and specifications (i.e., frequency range, permittivity range, temperature range, mechanical resistance) discussed in Section 3, but also based on the properties of the tissue under investigation. The size of the selected probe has to be consistent with the sample surface, size, and heterogeneity in order to achieve good probe-tissue contact and accurate measurements in a homogeneous region.

After selecting the probe, but before measuring the dielectric properties, it is recommended to carefully plan the tissue preparation and handling procedures in order to reduce tissue-related confounders, such as sample cooling, dehydration, and damage.

6.6.2 Tissue Preparation and Handling

Tissue measurements can be performed *in vivo* or *ex vivo*; the tissue preparation and handling will be different in each case. Often, for reasons of convenience (i.e., patient safety, ethics) or due to difficulties in establishing a good probe-sample contact with *in vivo* tissues, dielectric measurements of animal and human tissues are performed *ex vivo*.

6.6.2.1 *In Vivo vs. Ex Vivo Measurements*

Several authors have reported on whether or not differences exist in tissue dielectric properties acquired *in vivo* and *ex vivo*. These works will be discussed here in chronological order. Initially, Burdette et al. performed *in vivo* measurements on canine muscle, kidney cortical tissue, and fat tissue, and differences were found between acquired *in vivo* data and reported *ex vivo* data [39]. In particular, for *in vivo* canine fat tissue, the measured permittivity values were a factor of approximately 1.5 to 3 times larger than the *in vitro* permittivity values acquired previously by other authors [39,52,146]. This difference in dielectric properties was most likely due to differences in water content, in temperature, or actual physiological differences between living and non-living tissues [39]. Next, Kraszewski et al. performed both *in vivo* and *ex vivo* dielectric measurements on rat and cat tissues, finding only dielectric changes less than the uncertainty at frequencies between 100 MHz and 8 GHz [40]. Schwartz observed that the permittivity and conductivity of frog heart, in the frequency range 0.2–8 GHz, were higher *in vivo* than *ex vivo*, with the difference being attributed to blood perfusion changes [41]. More recently, a variation between *in vivo* and *ex vivo* dielectric properties was found by Gabriel et al. and Peyman et al. in skin, spinal cord, skull, long bone, and bone marrow in the microwave frequency range [42,43,66,142]. Similar differences were not observed in other tissues, but might indicate unavoidable contamination of tissues with blood or other body fluids [43]. From the analysis of normal and malignant human liver tissues, O'Rourke et al. found a statistically significant difference between *in vivo* and *ex vivo* normal liver tissue, but not between *in vivo* and *ex vivo* malignant liver tissue [37]. Furthermore, Halter et al. evaluated the changes of breast cancer dielectric properties between *in vivo* and *ex vivo* measurements and found about a 30% drop in the magnitude of the permittivity in tissues analysed 300 min after excision [10]. More recently, Shahzad et al. found that over the 210 min following excision, the relative permittivity of liver tissue, as measured on the surface of the sample, decreased by 32 points [147]. However, this decrease was attributed fully to dehydration of the surface of the tissue sample as dielectric measurements conducted on the interior of the sample did not change considerably over the same time period [147]. The exact magnitude of the change in dielectric properties from time of excision to time of measurement, caused by dehydration and temperature effects, will vary based on the tissue type, the environment that the tissue is stored in, and the tissue handling conditions.

As is clear from the varied results of these studies, there is no consensus on: (i) Whether a difference in the dielectric properties of *in vivo* and *ex vivo* tissues exists over the microwave frequency range; and (ii) if a difference does exist, the magnitude and direction of it. Despite these results, the difference between *in vivo* and *ex vivo* data in the microwave frequency range is, generally, attributed to the temperature change and tissue dehydration [10,30,39,43,86], and recent studies following best practice in dealing with these confounders suggest no significant difference in the dielectric properties measured from *in vivo* and *ex vivo* measurements [84,148].

Therefore, following best measurement practice, it is advantageous to keep the temperature constant during dielectric measurement using a temperature controlled container or a water bath [29,40,43,44,122,127,142] and to minimise dehydration by limiting the time between excision and measurement to a few hours [27,30,40,42,43,62,65,76,78,86,127,142,149–151]. At frequencies lower than 100 MHz, a larger variation between in vivo and ex vivo properties is found. This difference is attributed to physiological parameters, such as blood flow in vessels [27,39,65,86,151], ischemia [10,86,150,151], heart rate [43], arterial pressure [43,86,150], respiration rate [43], and air content in lungs [149], which can affect the permittivity and conductivity values at these frequencies.

In the following subsections, the best-practice steps involved in both in vivo and ex vivo measurements are described: From surgical intervention, to sample access and excision, transportation, handling, and processing. In each step, all potential tissue-related confounders, as well as the different methods used in previous works to compensate for them, are reported.

6.6.2.2 Surgical Intervention, Sample Access, and Excision

The first step in defining a sample handling procedure involves identifying the surgical methods to be used for tissue access and excision. It is necessary to define a surgical protocol that minimises tissue property modification. The main factors interfering with the dielectric acquisition concern the use of chemicals [39,127], which alter the body physiological condition, the use of tools or techniques [10], which may damage tissues, and the tissue exposure and cooling during the surgical operation [39–41,43,152].

It is useful to test for, and take into account, the effect of anaesthesia or other pharmaceuticals, which are used on animal/human tissues and physiological parameters. For instance, Burdette et al. observed a decrease in body temperature due to anaesthesia [39].

During the surgery, contact with the tissue should be minimised in order to avoid any damage or contamination. For human in vivo studies, the measurement tools need to be sterilised prior to surgery. Normally, steam sterilisation is performed prior to calibration [10,37] and a calibration refresh could be performed in the sterile environment before the in vivo measurements [10]. Furthermore, for in vivo measurements, the temperature tolerance of the probe (that depends on the probe fabrication materials) needs to be taken into account when selecting the sterilisation (or autoclave) procedure. For instance, steam sterilisation is, generally, performed at temperatures within 125 °C, while dry heat sterilization can be conducted at temperatures up to 190 °C.

Other important confounders to take into consideration in the operating room during in vivo measurements are those related to the tissue exposure to air. Specifically, air contributes to tissue cooling (from body temperature to room temperature) and to tissue dehydration. Different techniques have been adopted in in vivo measurements to prevent tissue cooling and dehydration. For example, Ranck and BeMent performed experiments within a few minutes from the surgical cut used to expose the interior tissues, and used warm saline to wet the measurement region [152]. Schwartz et al. rinsed the tissues and kept them moist with frog physiological solution [41]. Hart and Dunfee applied Ringer's solution with a medicine dropper to the muscle to prevent drying between the measurements [153]. However, these methods to reduce dehydration can impact the dielectric property measurement, since the solutions used have their own dielectric properties that will then contribute to the dielectric measurement of the tissue. Thus, the use of solutions, especially saline, should be avoided. More commonly, tissue dehydration during an in vivo measurement is minimised by reducing the time between the

surgical cut performed to expose the tissue and the dielectric measurement, and covering the area of interest with another tissue between measurement times [39,40,43]. This technique does not alter the tissue properties and also minimises tissue cooling. The tissue temperature should be measured frequently, so that any temperature change is taken into account during data analysis.

In previous works, the *in vivo* tissue temperature was monitored using thermocouple probes [27,29,62] and, more recently, fibre-optic thermometers [29,30]. Infrared thermometers may also be used for tissue temperature monitoring, since they are portable and do not require sample contact [79]. The same sensors can also be used in *ex vivo* measurements. A further crucial point in *in vivo* measurements concerns the probe positioning. Typically, in *ex vivo* scenarios, the probe–tissue contact can be verified by visual inspection; however, this approach can be challenging in a surgical setting. The probe positioning cannot be accurately planned prior to surgery; thus, it is normally decided in the surgical theatre.

6.6.2.3 Tissue Transportation

When *ex vivo* measurements are performed, the excised sample may be transported from the operating theatre to a secondary location for measurement, characterisation, or histology (details on histological analysis are presented in Section 7). The time between excision and *ex vivo* measurements is minimised to prevent tissue dehydration [27,30,40,42,43,62,78,86]. Aside from water content change, care should be taken during tissue transportation to avoid changes in the sample temperature. Since the temperature has a systematic impact on the measured dielectric spectrum of biological tissues, it is usually necessary to transport the tissue in hermetically-sealed, temperature-controlled containers [29,44,76,142].

6.6.2.4 Tissue Handling

In order to prevent tissue contamination, dehydration, and damage, sample handling prior to the *ex vivo* measurements should be minimised [39,71,76,142]. The sample temperature can be kept constant during the measurements using a water bath [29,40,43,122,142]. As the temperature setting of the water bath may not be equivalent to the tissue temperature, the tissue temperature should still be verified using an infrared or fibre-optic thermometer [29,30]. In this way, the tissue temperature variation can be taken into account during data analysis. Details on how tissue temperature affects the measured dielectric properties are reported in Section 6.3.3.

If the tissue sample is to be analysed histologically, the measurement points should be marked. Sample marking is necessary to ensure that the histological analysis involves the portion of tissue corresponding to the volume interrogated by the probe. Thus, a good correspondence between the tissue histological and dielectric properties can be found. Further details about the histological characterisation of tissue samples are reported in Section 7. In previous works, acrylic ink [76,79] or pins [10] have been used as sample markers. When *ex vivo* measurements are performed at the same locations where *in vivo* measurements were taken, it would be wise to test the effect of the marker on tissue dielectric properties before experimental implementation in order to prevent tissue modification

or damage by the marker. Lastly, in order to maintain the integrity of the tissue, the use of additive and preservatives should be avoided until the measurement is completed [127].

Having presented the confounders that should be considered during the planning of the tissue measurement procedure, in the next subsection the actual measurement procedure and the key confounders that affect tissue dielectric property measurements are discussed.

6.6.3 Procedure for Tissue Measurements

After the equipment set-up, calibration, and validation, the measurements on in vivo or excised tissues can be performed. It is important to note that some confounders cannot be minimised even with careful preplanning. These confounders need to be controlled, monitored, or compensated for during the measurement phase. In order to minimise the effects of the environmental parameters on tissue dielectric properties, it is advantageous to perform measurements in a climate (temperature, pressure, and humidity) controlled room [43,127].

In the following paragraphs the main confounders occurring during the measurement phase, such as measurement region choice, probe-tissue contact, and pressure, as well as tissue sample temperature, are discussed.

6.6.3.1 Measurement Region Choice Confounders

The confounders mentioned in Section 6.1 (i.e., probe sensing volume, tissue thickness, tissue surface, and sample heterogeneity) need not only be considered in the planning phase, but also need to be controlled and managed in relation to the choice of the measurement region. Additional considerations may also be needed, for instance, in order to prevent undesirable reflections negatively affecting the measured data, Abdilla et al. placed a shorting block under the sample to check for any reflections from the sample boundaries [44].

Confounders intrinsic to the tissue type include: Fibre orientation in anisotropic tissues, presence of blood vessels, and high heterogeneity. It was observed that anisotropic tissues, such as muscles, present different dielectric properties according to the measurement directions along or across the fibre. Specifically, it has been found that in the microwave frequency range (from 200 MHz to 20 GHz) the permittivity values between the two sets of measurements are not substantially different. On the other hand, at lower frequencies (10^{-5} –1 MHz) the fibre direction can change the relative permittivity by

100% [42]. Blood vessels are non-uniformly distributed in tissues and may make up roughly 30% of their volume [144], so the probe position relative to that of blood vessels should be checked by visual inspection [65,151]. In highly heterogeneous and mechanically stiff tissues the uncertainty is generally higher and, in order to minimise the random errors arising from tissue heterogeneity and complexity, it is useful to repeat the measurements at multiple points [43,44,75]. For instance, Peyman et al. stated that as many measurements as possible should be taken on each sample tissue and, in her study conducted in 2005, at least six measurements were taken on each tissue [43]. In most other dielectric studies, three to five measurement locations were, generally, selected on each tissue sample [27,40,44].

6.6.3.2 Probe-Tissue Contact

Having selected the most suitable measurement region, the probe is placed in contact with the sample. From the authors' experience, in order to reduce the uncertainty due to probe and cable movement, in both ex vivo and in vivo measurements (in in vivo measurements only when the animal size is relatively small), it is convenient to move the sample towards the probe using a lift table until the entire probe aperture makes firm contact with the tissue sample as opposed to moving the probe during the measurement procedure.

Measured reflection coefficient data is extremely sensitive to the probe positioning relative to the sample surface. A high variability in the dielectric properties can be attributed to variability in probe-tissue contact. Thus, a firm contact between the probe and the tissue [76,93] is key. A good quality contact reduces the impact of confounders that increase the measurement

uncertainty, such as pressure differences [39,43,80,97,149], air gaps [70,93,95,126], and biological fluid accumulation at the probe tip [39,43]. In most works, these factors have been monitored by a close visual inspection [29,41,43,76,95]. In order to keep the applied pressure constant in ex vivo measurements, weighing scales or force sensors can be placed underneath the sample holder [79]. In fact, the application of a steady pressure contributes to more repeatable measurements [39]. However, in the literature to date, there is no work that quantifies the error in the measured data in terms of the variation of the applied pressure. The authors have performed a number of experiments to quantify the error introduced by probe pressure variations, but observed that the outcome found for one measurement point could not be extended to all the measurement points across the sample. For instance, within the same tissue sample, there can be some differences in terms of sample thickness, tissue mechanical properties, water content, and surface irregularities, which may require the application of different probe pressures on the same sample. Thus, no specific, fixed pressure can be reported for all samples. However, a technique that may be used to obtain a good quality contact is as follows. First, a low pressure is applied to the probe to contact the sample. This low pressure, if too low, can lead to data inconsistencies when repeated measurements are taken at the same point (due to air gaps). If this occurs, a pressure adjustment can be undertaken until measurements at the same location are repeatable. Conversely, the application of high pressure, if too high, can cause tissue compression and can prompt fluid from within the tissue to rise to the tissue surface, or worse, can cause tissue damage [127,149]. In previous works, sample contamination by biological fluids has been reduced by using cotton wipes/swabs [43,99,127,142,152] or suction [43]. However, it should be noted that the suction method is more invasive and has the potential to dehydrate the sample.

6.6.3.3 Temperature Effects

During dielectric measurements, as discussed in Section 6.2.1, the temperature needs to be controlled and monitored. While different techniques used to monitor or control the temperature have been discussed in earlier sections, in this subsection the effect of temperature on tissue dielectric properties is examined.

In previous studies, the dielectric properties of biological tissues at discrete frequencies and temperatures were measured and, for small temperature variations, they were presented in terms of linear temperature coefficients, which are defined as the percent change in either permittivity or conductivity per degree Celsius [53]. The provided linear temperature coefficients are limited to a number of specific discrete frequencies and temperatures [27,30,62]. Outside of these frequencies and temperatures the impact of temperature on the dielectric properties may no longer be linear [30]. A brief summary of the previously published temperature-dependent dielectric properties data is presented in Lazebnik et al. [30]. In the microwave frequency range, the change in relative permittivity is, at most, 2% per degree Celsius and the change in conductivity is between 1% and 2% per degree Celsius, depending on the tissue and on the frequency and temperature range considered. Generally, the relative permittivity and conductivity trends with temperature differ over frequency. However, the magnitude change in both permittivity and conductivity per degree Celsius tends to be higher at lower frequencies in most biological tissues [27,30,62]. Lazebnik et al. developed a model to characterise the temperature-dependence of liver tissue dielectric properties over the microwave frequency range [30]. In particular, from the liver dielectric measurements, Lazebnik et al. identified different “cross-over” points in the trends of both relative permittivity and conductivity with temperature. In relative permittivity, the cross-over point was found at about 4 GHz. Below the cross-over point, the permittivity decreases slowly as temperature increases

and, above the cross-over point, the permittivity increases with temperature. For conductivity, two cross-over points were found: One near 2–3 GHz and the other near 16 GHz. Below the first cross-over point, the conductivity increases slowly as temperature increases. Between the two cross-over points, the trend reverses, and above the second cross-over point, the conductivity again increases as temperature increases. The same trends were also found for water [30].

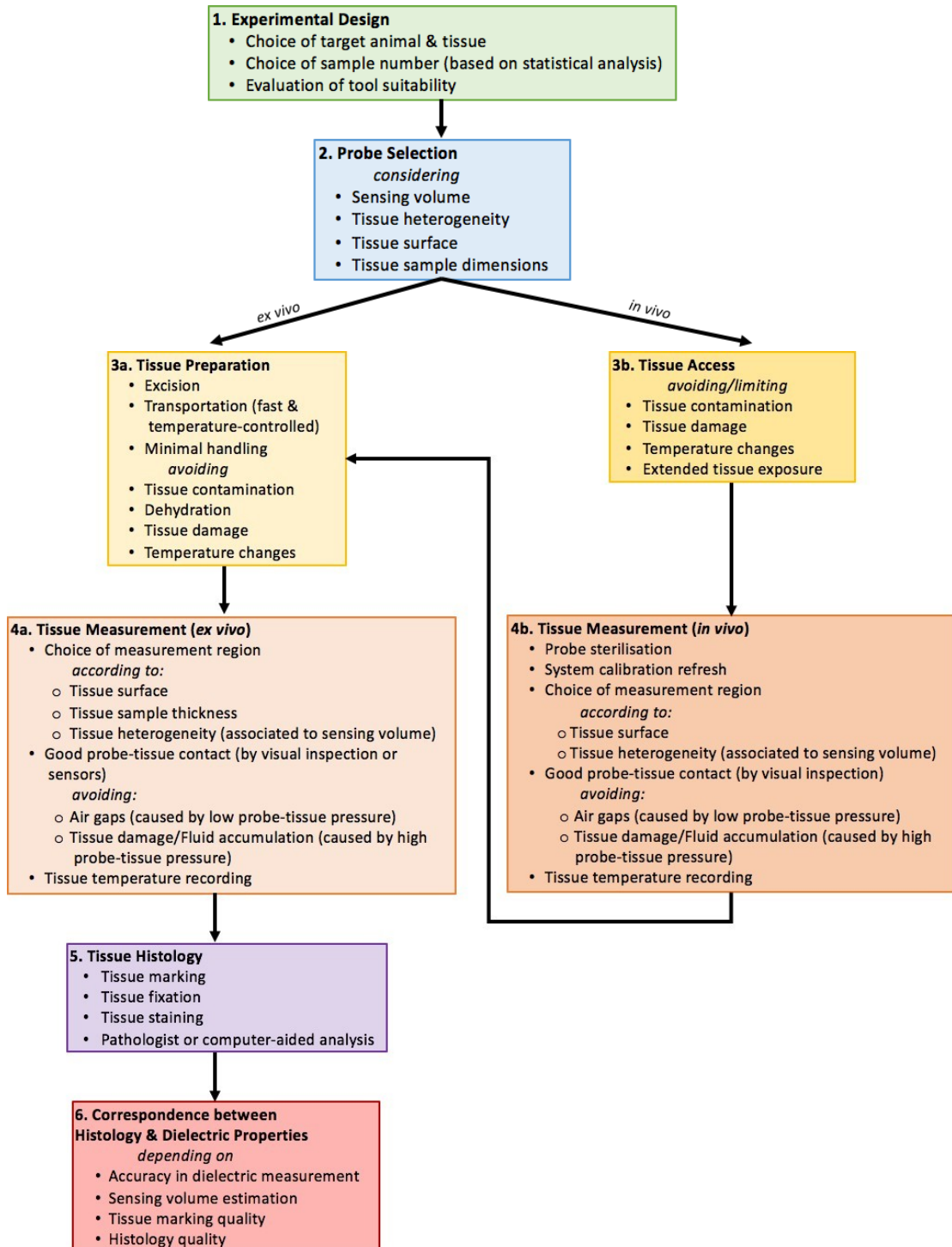


Figure 6.2, Flow chart of the common steps to minimise tissue-related errors in in vivo and ex-vivo measurements.

More recently, temperature coefficients were provided for a wider temperature range (upto 100°C) at the discrete frequencies of 915 MHz and 2.45 GHz, which are of interest for microwave liver

tissue ablation [31,154]. Brace et al. found that linear temperature coefficients across the 5–50 °C range agreed well with the results of Lazebnik et al., with coefficients of –0.22 and –0.18 in relative permittivity for the two frequency points, respectively, and coefficients of 1.29 and –0.2 for conductivity [31]. From 50 °C to 100 °C, both relative permittivity and conductivity were found to decrease by as much as 50%, due to both irreversible damage of the tissues and tissue dehydration [31]. In summary, the temperature coefficients for both permittivity and conductivity depend on tissue-type, on frequency, and on the considered temperature range. Knowledge of these temperature coefficients can be used to compensate for the effect of the temperature change during tissue dielectric measurements.

In this section, the importance of preplanning the measurement procedure was highlighted, the measurement process overviewed, and the main confounders involved in the measurement were described. The most common practices adopted to minimise tissue-related errors are summarised in Figure 6.2. In the next section, histological analysis of tissue samples is discussed as a method to reduce the confounders related to the intrinsic heterogeneity of biological tissues.

6.7 Tissue Sample Histological Analysis

Histology is the study of the microscopic structure of cells and tissues; while histopathology refers to the same, but with diseased tissue [155,156]. There are multiple steps involved in the histological analysis of a tissue sample: The sample must be fixed, embedded in wax, sliced, mount on slides, stained, and then imaged [157]. Following these steps, the slices are ready to be analysed by a pathologist. The pathologist is able to examine the images and determine: (i) The types of tissues present; (ii) if diseased tissue is present, the disease grade and other characteristics (for example, with breast cancer, the hormone receptor status) [156]; and (iii) the distribution of the tissue types within the sample. Histological analysis is, especially, required after the acquisition of the dielectric properties of a heterogeneous tissue sample in order to determine the tissue types present in the sample and their relative spatial distribution. This is important because the dielectric properties of a sample are determined by those of its constituent tissue types; thus, the histological analysis enables the attribution of measured dielectric properties to the appropriate tissue type.

Many studies performed in the literature involve only homogeneous (or assumed homogeneous) tissues and, thus, the samples do not undergo histological analysis (for example, liver tissue [27,44]). In this section, the focus is on heterogeneous tissue samples. Measuring the dielectric properties of heterogeneous tissues is inherently challenging as spectroscopy has the effect of averaging the dielectric properties throughout the sensing volume that is illuminated by the electromagnetic field [11]. Thus, in the next subsection, confounders that can contribute to any histological analysis are detailed, along with ones that are of specific concern for dielectric measurements of heterogeneous tissues. Finally, histological analysis methods used for attributing dielectric properties to heterogeneous tissues from the literature are overviewed, and the best practice techniques that are known are highlighted.

6.7.1 Factors Impacting Histological Analysis

The procedures involved with histological preparation of the tissue are applied by pathologists thousands, if not millions, of times per year. In fact, there are more than 14 pathology tests examined per person in the UK each year, and pathological analysis is a part of 70% of all diagnoses [158]. However, the methods are not without flaws. In particular, poor fixation of the sample can lead to changes in the tissue structure [11,157] and uneven levels of staining

can result in images that are incomplete or out of focus [157]. Slide digitation can have variations in lighting conditions and magnification that can affect interpretation of the results, particularly when comparing across slices [157]. Each of these issues increases the challenge of interpreting the dielectric measurement of heterogeneous samples based on the histology of tissues samples and makes it especially difficult to compare between studies. Furthermore, the histological interpretation of a slice itself is subjective and variability in results between pathologists are possible [159–161]. Computer-aided diagnosis (CAD) and prognosis (CAP) methods are currently being investigated to create a fully automated analysis that is faster and more consistent than a human-based analysis [157]. An excellent review of challenges associated with histopathological analysis can be found in Veta et al. [157].

6.7.2 The Link between Heterogeneity, Histology, and Sensing Volume

When performing histology to support interpretation of the tissue content contributing to a dielectric measurement, it is important to include in the histological analysis all of the tissues that are within the sensing volume. However, at the same time, the histological analysis should not include any tissues that are outside of the sensing volume. In this way, only, and exactly, the tissues that have contributed to the measurement are analysed.

As an example, Figure 6.3 demonstrates the importance of matching the sensing depth with the number and thickness of slices taken into consideration in the histological analysis. If only Slice 1 is analysed, the tissue is found to be composed entirely of homogeneous glandular tissue. If the sensing depth is equal to the thickness of Slice 1, then the measured dielectric properties will be entirely the result of this layer of homogeneous gland tissue. Alternatively, if the sensing depth is equal to, say, the combined thickness of Slices 1 and 2, then the total sensing depth region is occupied by 25% fat tissue and 75% glandular tissue (as Slice 1 is 100% gland, and Slice 2 is 50% gland and 50% fat). Both of these tissue types will contribute to the measured dielectric properties. However, the contribution is not proportional to the tissue type representation (i.e., 25% fat and 75% gland) as the layer closest to the probe has the dominant effect [11,80,81]. Furthermore, not all of a given tissue is occupied fully by cells of that tissue type [12], thus, an additional layer of complication comes into the example based on how to determine what regions are actually “fat” and which are “gland”. Obviously, as more slices are involved in the analysis and the tissue becomes more heterogeneous, the more challenging it becomes to conclusively determine the tissue composition breakdown. It is also important to re-emphasise here that the sensing volume is dependent on the tissue content (namely, the tissue dielectric properties), so, ideally, the change in the sensing volume should be taken into account on a sample-to-sample basis.

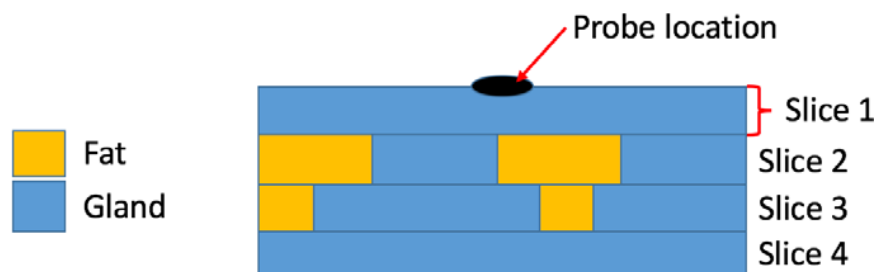


Figure 6.3, Diagram of sample composition by tissue type (fat—orange, gland—blue). A side view of the sample is shown, with slices marked. The dielectric probe measurement location is denoted with a black oval on the top of Slice

6.7.3 Histological Analysis Techniques in Dielectric Studies

A limited number of works involving histological analysis for attributing the measured dielectric properties of heterogeneous tissues have been presented in the literature. Of these, some use pathology to categorise tissue samples by type [79,86], while a select few process the tissue for microscopic analysis [10–12,76]. In general, histology for dielectric characterisation is an area that requires further investigation [43]. The most common strategy is to obtain an average estimate of the tissue types present in the sample below the probe [10,11,76]. However, most recently a more quantitative method of counting each cell and corresponding the proportion of tissue with the measured properties has been proposed [12]. These techniques are described and compared in this section. For dielectric property measurements of heterogeneous tissue, breast tissues are by far the most common that have been analysed due to the need for these properties in medical microwave imaging of the breast. As a result, all pathology techniques discussed in this section have all been performed on breast tissues.

In Lazebnik et al., several hundred dielectric measurements were taken from normal and malignant excised breast tissue samples using an open-ended coaxial probe [11,76]. The measurement sites were marked on the tissue samples using a spot of black ink. The authors conducted a histological analysis of each sample based on the tissue composition inside the region of the sensing volume of the probe (3 mm deep \times 7 mm across, for this measurement scenario, as determined in Hagl et al. [71]). In this way, a cross-section of each tissue sample was taken directly below the measurement location (i.e., the ink spot). Digital microscopy images were obtained and visually inspected. The tissue composition within the sensing volume was quantified based on the percentage of each tissue type residing within the slice under consideration. The two-dimensional cross-section was used to obtain an estimate of the tissue composition in the full three-dimensional sensing volume. The percentages of each tissue type (adipose (fat), glandular and fibroconnective tissue, along with benign and malignant tissue) were estimated visually by qualified pathologists [11,76]. A Kappa statistic was used to confirm consistency in the analysis between different pathologists. Several exclusion criteria were applied during the histological process. In particular, samples were eliminated from further consideration if the ink spot was not visible, if the ink had leaked into the tissue, or if the cross-sectional slice was deformed. In this study, nearly half of all samples (49.8%) were excluded based on difficulties during the histological procedure [76]. Following the studies by Lazebnik et al., Halter et al. performed a study that also examined the region under the probe using histological analysis. In Halter et al., the dielectric properties of in vivo and ex vivo breast tissues were measured in the microwave frequency range with open-ended coaxial probes [10]. After the in vivo tissue measurement was recorded, a biopsy clip was embedded in the tissue at the measurement location. The tissue was then excised and sectioned into 5 mm thick pieces. The excised samples were measured again (at the same site as for in vivo, as identified by the clip). Initially, the pathologist examined a 1 cm \times 1 cm square area around the measurement location and, thus, the tissue types were estimated based on a large area. Later, the strategy was improved by inserting two pins covered in ink into the tissue on either side of the depression left by the probe in order to mark the measurement location. The tissue sample was fixed with formalin, stained, and then slides were prepared. The pin holes were then used during the analysis to determine the probed region in which the tissue types were estimated by the pathologist. In this study, details were not provided regarding whether or not samples had to be excluded from consideration due to histological challenges.

The pathologist examined the tissue histology within the \sim 1 cm \times 1 cm region, which was a horizontal slice relative to the probe position (i.e., perpendicular to the plane of the probe axis),

unlike the vertical (or parallel) slice used in Lazebnik et al. However, in both cases, the full tissue composition within the sensing volume was estimated based on the given slice. Furthermore, as only one pathologist was involved in the study, a Kappa analysis similar to that in the study by Lazebnik et al. was not needed. Most recently, in Sugitani et al., excised breast tissue samples were obtained and their complex permittivities measured using an open-ended coaxial probe [12]. The samples contained a combination of tumour tissue, normal fat tissue, and normal stroma (connective) tissue. The work aimed to calculate the effective permittivity of the tumour tissue based on the idea that each sample is an inhomogeneous mixture of cells with different permittivities. It was proposed, and confirmed, that, since the “tumour” tissue is composed of cancer cells mixed in with normal cells, the volume fraction of cancer cells in a sample affects the dielectric properties. In particular, the sample was treated with a hematoxylin-eosin stain and then digital images of each slice of the sample were taken. The slide images were analysed by counting the number of pixels of cancer cells and cells of other tissue types presented. The ratios of each type of tissue cell, relative to all of the cells in the slice, were calculated. The three-dimensional fractional volume of each cell type was calculated based on the two-dimensional slice using Bruggeman’s effective medium approximation theory [162]. This method has the advantage of being highly quantifiable—each cell is counted—however, the process is tedious and time-consuming. The work does not mention if any samples had to be discarded or were contaminated during the histological procedures. Furthermore, the sample analysis was not restricted to a specific sensing depth region (sample sizes ranged from 5 cm to 30 cm). A similar study on various types of malignancies was presented in Sugitani et al. [85], for which the pathological procedures were the same as those in Sugitani et al. [12].

Overall, there is no consensus in the literature to date on the best practice for conducting histology in relation to dielectric measurements. Furthermore, there has been no reported comparison of the different histology techniques used in the above-mentioned works, therefore, it is not known if some methods are more accurate than others. However, it is likely that some features from each of the studies lend themselves to obtaining more accurate data, for example, involving multiple pathologists and using Kappa analysis to verify consistency between them (as in the study by Lazebnik et al.) could only add to the study quality.

6.8 Discussion and Conclusions

Although notable progress has been made in achieving accurate dielectric data, the coaxial probe design still represents a limit for certain types of dielectric experiments. An improved probe design that could allow measurements over a wider spectrum of frequencies and across multiple tissue samples would be useful for future studies. Moreover, during the measurement procedure, the use of appropriate force and position sensors could considerably increase the stability of the measurement system and reduce tissue-related confounders that are strictly dependent on the expertise of the operator conducting the dielectric measurement (i.e., probe-tissue contact and probe-tissue pressure). Furthermore, interpretation of dielectric data acquired with the open-ended coaxial probe can be improved by quantitatively examining and compensating for tissue-related confounders that cannot be fully eliminated during the measurement procedure. To this extent, dielectric studies have modelled the effect of temperature, tissue dehydration, and animal age on the dielectric measurement of tissues. The quantitative characterisation of tissue-related confounders improves the interpretation of the acquired data and could support the interpretation of dielectric data from historic studies that did not provide information on all confounders. In order to clarify how such a characterisation could be done, a series of examples demonstrating how to determine the total uncertainty in a dielectric measurement are provided below.

This example scenario considers the case of dielectric measurement of mouse liver in the microwave frequency range, as the effect of the time from excision, temperature, and age of the mouse have all been quantified on liver tissue at these frequencies. In this example, it is assumed that the confounders of time from excision (TFE), temperature (T), and age (A), are the only ones impacting the dielectric data. The uncertainties introduced by these confounders are denoted as μ_{TFE} , μ_T , and μ_A , respectively. The relative permittivity of liver has been acquired at room temperature, 3.5 h from excision from a 70 day old mouse. From the literature it is known that at the frequency of 900 MHz, the relative permittivity changes by 0.13% per degree Celsius [30], decreases by about 25% after 3.5 h from excision [147], and decreases by approximately 15% within 70 days of life [142]. This quantitative information needs to be taken into account for the calculation of the combined standard uncertainty according to the NIST guidelines [74,75], which provides μ , the total uncertainty added to dielectric data. A series of hypothetical studies are listed in Table 6.4, along with the resulting uncertainty. The technique of calculating combined standard uncertainty to achieve a total estimate on the uncertainty introduced in dielectric measurement studies due to tissue-related confounders can and should be applied to all datasets, which lack quantitative information on confounders.

Table 6.4, Example calculations of total uncertainty in dielectric data resulting from tissue-related confounders under different measurement scenarios: Uncertainty due to time from excision (μ_{TFE}), due to temperature (μ_T), and due to age (μ_A). μ is the total uncertainty added to dielectric data, calculated as combined standard uncertainty. Uncertainty data is for the relative permittivity of mouse liver at 900 MHz, obtained from the literature. Note that 0.91% is $0.13\%/^{\circ}\text{C} \cdot 7^{\circ}\text{C}$.

Case Scenarios	μ_T	μ_{TFE}	μ_A	μ
Known TFE, Known age, Unknown T (between 18 °C and 25 °C)	0.91%	N/A	N/A	0.91%
Known T, Known age, Unknown TFE (within 3.5 h)	N/A	25%	N/A	25%
Known T, Known TFE, Unknown age (within 70 days old)	N/A	N/A	15%	15%
Known T, Unknown TFE (within 3.5 h), Unknown age (within 70 days old)	N/A	25%	15%	29.15%
Known TFE, Unknown age (within 70 days old), Unknown T (between 18 °C and 25 °C)	0.91%	N/A	15%	15.02%
Unknown TFE (within 3.5 h), Unknown age (within 70 days old), Unknown T (between 18 °C and 25 °C)	0.91%	25%	15%	29.17%

Given the importance of modelling the effect of the confounders for the interpretation and comparison of existing dielectric datasets, further investigation is needed to quantitatively examine the main tissue-related confounders (i.e., temperature, dehydration) on other tissue types and to analyse confounders not yet quantified (i.e., heterogeneity, probe pressure). Such quantitative analysis will not only improve the analysis of new dielectric data, but will also support the interpretation of historical dielectric datasets.

In conclusion, this work has presented the dielectric measurement process with an open-ended coaxial probe and reviewed the most relevant works, with a critical discussion of known equipment- and tissue-related confounders. This work supports the aim of achieving accurate

dielectric measurements of biological tissues. As these properties are fundamental to electromagnetic safety studies and medical technology design and improvement, an understanding of the measurement process is of interest to a wide ranging community of scientists and medical professionals.

Author Contributions: Conceptualization, M.O.; Methodology, E.P.; Investigation, A.L.G., I.M., E.P., A.S. and S.S.; Writing-Original Draft Preparation, A.L.G.; Writing-Review & Editing, E.P., I.M., M.O. and M.J.; Supervision, M.O. and E.P.; Project Administration, M.O.; Funding Acquisition, M.O.

Funding: The research leading to these results has received funding from the European Research Council, under the ERC Grant Agreement BioElecPro No. 637780, and Science Foundation Ireland (SFI), under the Grant 15/ERCS/3276. This work was also supported by the Hardiman Research Scholarship.

Acknowledgments: This work has been developed in the framework of COST Action MiMed (TD1301).

References:

1. Formica, D.; Silvestri, S. Biological Effects of Exposure to Magnetic Resonance Imaging: An Overview. *Biomed. Eng. Online* **2004**, *3*, 11. [[CrossRef](#)] [[PubMed](#)]
2. Martellosio, A.; Pasian, M.; Bozzi, M.; Perregrini, L.; Mazzanti, A. Exposure Limits and Dielectric Contrast for Breast Cancer Tissues: Experimental Results up to 50 GHz. In Proceedings of the 11th European Conference on Antennas and Propagation (EUCAP), Paris, France, 19–24 March 2017; pp. 667–671.
3. Nikolova, N.K. Microwave Imaging for Breast Cancer. *IEEE Microw. Mag.* **2011**, *12*, 78–94. [[CrossRef](#)]
4. Pastorino, M. *Microwave Imaging*; John Wiley & Sons: Hoboken, NJ, USA, 2010.
5. Noghianian, S. *Introduction to Microwave Imaging*; Springer: New York, NY, USA, 2014.
6. Zou, Y.; Guo, Z. A Review of Electrical Impedance Techniques for Breast Cancer Detection. *Med. Eng. Phys.* **2003**, *25*, 79–90. [[CrossRef](#)]
7. Brown, B. Electrical Impedance Tomography (EIT): A Review. *J. Med. Eng. Technol.* **2003**, *27*, 97–108. [[CrossRef](#)] [[PubMed](#)]
8. Waldmann, A.D.; Ortola, C.F.; Martinez, M.M.; Vidal, A.; Santos, A.; Marquez, M.P.; Roka, P.L.; Bohm, S.H.; Suarez-Sipmann, F. Position-Dependent Distribution of Lung Ventilation—A Feasibility Study. In Proceedings of the 2015 IEEE Sensors Applications Symposium (SAS), Zadar, Croatia, 13–15 April 2015.
9. Avery, J.; Dowrick, T.; Faulkner, M.; Goren, N.; Holder, D. A Versatile and Reproducible Multi-Frequency Electrical Impedance Tomography System. *Sensors* **2017**, *17*, 280. [[CrossRef](#)] [[PubMed](#)]
10. Halter, R.J.; Zhou, T.; Meaney, P.M.; Hartov, A.; Barth, R.J.; Rosenkranz, K.M.; Wells, W.A.; Kogel, C.A.; Borsic, A.; Rizzo, E.J.; et al. The Correlation of in Vivo and Ex Vivo Tissue Dielectric Properties to Validate Electromagnetic Breast Imaging: Initial Clinical Experience. *Physiol. Meas.* **2009**, *30*, S121–S136. [[CrossRef](#)] [[PubMed](#)]
11. Lazebnik, M.; McCartney, L.; Popovic, D.; Watkins, C.B.; Lindstrom, M.J.; Harter, J.; Sewall, S.; Magliocco, A.; Booske, J.H.; Okoniewski, M.; et al. A Large-Scale Study of the Ultrawideband Microwave Dielectric Properties of Normal Breast Tissue Obtained from Reduction Surgeries. *Phys. Med. Biol.* **2007**, *52*, 2637–2656. [[CrossRef](#)] [[PubMed](#)]
12. Sugitani, T.; Kubota, S.; Kuroki, S.; Sogo, K.; Arihiro, K.; Okada, M.; Kadoya, T.; Hide, M.; Oda, M.; Kikkawa, T. Complex Permittivities of Breast Tumor Tissues Obtained from Cancer Surgeries. *Appl. Phys. Lett.* **2014**, *104*, 253702. [[CrossRef](#)]

14. Porter, E.; Kirshin, E.; Santorelli, A.; Coates, M.; Popović, M. Time-Domain Multistatic Radar System for Microwave Breast Screening. *IEEE Antennas Wirel. Propag. Lett.* **2013**, *12*, 229–232. [[CrossRef](#)]
15. Scapaticci, R.; Bellizzi, G.; Catapano, I.; Crocco, L.; Bucci, O.M. An Effective Procedure for MNP-Enhanced Breast Cancer Microwave Imaging. *IEEE Trans. Biomed. Eng.* **2014**, *61*, 1071–1079. [[CrossRef](#)] [[PubMed](#)]
16. O'Halloran, M.; Morgan, F.; Flores-Tapia, D.; Byrne, D.; Glavin, M.; Jones, E. Prototype Ultra Wideband Radar System for Bladder Monitoring Applications. *Prog. Electromagn. Res. C* **2012**, *33*, 17–28. [[CrossRef](#)]
17. Arunachalam, K.; MacCarini, P.; De Luca, V.; Tognolatti, P.; Bardati, F.; Snow, B.; Stauffer, P. Detection of Vesicoureteral Reflux Using Microwave Radiometry System Characterization with Tissue Phantoms. *IEEE Trans. Biomed. Eng.* **2011**, *58*, 1629–1636. [[CrossRef](#)] [[PubMed](#)]
18. Ireland, D.; Bialkowski, M.E. Microwave Head Imaging for Stroke Detection. *Prog. Electromagn. Res. M* **2011**, *21*, 163–175. [[CrossRef](#)]
20. Persson, M.; Fhager, A.; Trefna, H.D.; Yu, Y.; McKelvey, T.; Pegenius, G.; Karlsson, J.E.; Elam, M. Microwave-Based Stroke Diagnosis Making Global Prehospital Thrombolytic Treatment Possible. *IEEE Trans. Biomed. Eng.* **2014**, *61*, 2806–2817. [[CrossRef](#)] [[PubMed](#)]
21. Dowrick, T.; Blochet, C.; Holder, D. In Vivo Bioimpedance Measurement of Healthy and Ischaemic Rat Brain: Implications for Stroke Imaging Using Electrical Impedance Tomography. *Physiol. Meas.* **2015**, *36*, 1273–1282. [[CrossRef](#)] [[PubMed](#)]
22. Scapaticci, R.; Bucci, O.M.; Catapano, I.; Crocco, L. Differential Microwave Imaging for Brain Stroke Followup. *Int. J. Antennas Propag.* **2014**. [[CrossRef](#)]
24. Datta, N.R.; Ordóñez, S.G.; Gaip, U.S.; Paulides, M.M.; Crezee, H.; Gellermann, J.; Marder, D.; Puric, E.; Bodis, S. Local Hyperthermia Combined with Radiotherapy And/or Chemotherapy: Recent Advances and Promises for the Future. *Cancer Treat. Rev.* **2015**, *41*, 742–753. [[CrossRef](#)] [[PubMed](#)]
25. Issels, R.D.; Lindner, L.H.; Ghadjar, P.; Reichardt, P.; Hohenberger, P.; Verweij, J.; Abdel-Rahman, S.; Daugaard, S.; Salat, C.; Vujaskovic, Z.; et al. 13LBA Improved Overall Survival by Adding Regional Hyperthermia to Neo-Adjuvant Chemotherapy in Patients with Localized High-Risk Soft Tissue Sarcoma (HR-STs): Long-Term Outcomes of the EORTC 62961/ESHO Randomized Phase III Study. *Eur. J. Cancer* **2015**, *51*, S716. [[CrossRef](#)]
26. Wessalowski, R.; Schneider, D.T.; Mils, O.; Friemann, V.; Kyrillopoulou, O.; Schaper, J.; Matuschek, C.; Rothe, K.; Leuschner, I.; Willers, R.; et al. Regional Deep Hyperthermia for Salvage Treatment of Children and Adolescents with Refractory or Recurrent Non-Testicular Malignant Germ-Cell Tumours: An Open-Label, Non-Randomised, Single-Institution, Phase 2 Study. *Lancet Oncol.* **2013**, *14*, 843–852. [[CrossRef](#)]
27. Ekstrand, V.; Wiksell, H.; Schultz, I.; Sandstedt, B.; Rotstein, S.; Eriksson, A. Influence of Electrical and Thermal Properties on RF Ablation of Breast Cancer: Is the Tumour Preferentially Heated? *Biomed. Eng. Online* **2005**, *4*. [[CrossRef](#)] [[PubMed](#)]
28. Bargellini, I.; Bozzi, E.; Cioni, R.; Parentini, B.; Bartolozzi, C. Radiofrequency Ablation of Lung Tumours. *Insights Imaging* **2011**, *2*, 567–576. [[CrossRef](#)] [[PubMed](#)]
30. Curley, S.A.; Marra, P.; Beaty, K.; Ellis, L.M.; Vauthey, J.N.; Abdalla, E.K.; Scaife, C.; Raut, C.; Wolff, R.; Choi, H.; et al. Early and Late Complications after Radiofrequency Ablation of Malignant Liver Tumors in 608 Patients. *Ann. Surg.* **2004**, *239*, 450–458. [[CrossRef](#)] [[PubMed](#)]
31. Stauffer, P.R.; Rossetto, F.; Prakash, M.; Neuman, D.G.; Lee, T. Phantom and Animal Tissues for Modelling the Electrical Properties of Human Liver. *Int. J. Hyperth.* **2003**, *19*, 89–101. [[CrossRef](#)]

32. Yang, D.; Converse, M.; Mahvi, D.; Webster, J. Measurement and Analysis of Tissue Temperature during Microwave Liver Ablation. *IEEE Trans. Biomed. Eng.* **2007**, *54*, 150–155. [[CrossRef](#)] [[PubMed](#)]
33. Lopresto, V.; Pinto, R.; Lovisolo, G.; Cavagnaro, M. Changes in the Dielectric Properties of Ex Vivo Bovine Liver during Microwave Thermal Ablation at 2.45 GHz. *Phys. Med. Biol.* **2012**, *57*, 2309–2327. [[CrossRef](#)] [[PubMed](#)]
34. Lazebnik, M.; Converse, M.; Booske, J.H.; Hagness, S.C. Ultrawideband Temperature-Dependent Dielectric Properties of Animal Liver Tissue in the Microwave Frequency Range. *Phys. Med. Biol.* **2006**, *51*, 1941–1955. [[CrossRef](#)] [[PubMed](#)]
35. Brace, C.L. Temperature-Dependent Dielectric Properties of Liver Tissue Measured during Thermal Ablation: Toward an Improved Numerical Model. In Proceedings of the IEEE Engineering in Medicine and Biology Society, Vancouver, BC, Canada, 20–25 August 2008; pp. 230–233.
36. Wust, P.; Hildebrandt, B.; Sreenivasa, G.; Rau, B.; Gellermann, J.; Riess, H.; Felix, R.; Schlag, P.M. Hyperthermia in Combined Treatment of Cancer. *Lancet Oncol.* **2002**, *3*, 487–497. [[CrossRef](#)]
37. Ahmed, M.; Brace, C.L.; Lee, F.T.; Goldberg, S.N. Principles of and Advances in Percutaneous Ablation.
38. *Radiology* **2011**, *258*, 351–369. [[CrossRef](#)] [[PubMed](#)]
39. Dupuy, D.E. Image-Guided Thermal Ablation of Lung Malignancies. *Radiology* **2011**, *260*, 633–655. [[CrossRef](#)] [[PubMed](#)]
40. Ji, Z.; Brace, C.L. Expanded Modeling of Temperature-Dependent Dielectric Properties for Microwave Thermal Ablation. *Phys. Med. Biol.* **2011**, *56*, 5249–5264. [[CrossRef](#)] [[PubMed](#)]
41. Cavagnaro, M.; Pinto, R.; Lopresto, V. Numerical Models to Evaluate the Temperature Increase Induced by Ex Vivo Microwave Thermal Ablation. *Phys. Med. Biol.* **2015**, *60*, 3287–3311. [[CrossRef](#)] [[PubMed](#)]
42. O'Rourke, A.P.; Lazebnik, M.; Bertram, J.M.; Converse, M.C.; Hagness, S.C.; Webster, J.G.; Mahvi, D.M. Dielectric Properties of Human Normal, Malignant and Cirrhotic Liver Tissue: In Vivo and Ex Vivo Measurements from 0.5 to 20 GHz Using a Precision Open-Ended Coaxial Probe. *Phys. Med. Biol.* **2007**, *52*, 4707–4719. [[CrossRef](#)] [[PubMed](#)]
43. Stuchly, M.A.; Athey, T.W.; Samaras, G.M.; Taylor, G.E. Measurement of Radio Frequency Permittivity of Biological Tissues with an Open-Ended Coaxial Line: Part II—Experimental Results. *IEEE Trans. Microw. Theory Tech.* **1982**, *30*, 87–92. [[CrossRef](#)]
44. Burdette, E.; Cain, F.; Seals, J. In Vivo Probe Measurement Technique for Determining Dielectric Properties at VHF through Microwave Frequencies. *IEEE Trans. Microw. Theory Tech.* **1980**, *28*, 414–427. [[CrossRef](#)]
45. Kraszewski, A.; Stuchly, M.A.; Stuchly, S.S.; Smith, A.M. In Vivo and in Vitro Dielectric Properties of Animal Tissues at Radio Frequencies. *Bioelectromagnetics* **1982**, *3*, 421–432. [[CrossRef](#)] [[PubMed](#)]
46. Schwartz, J.L.; Mealing, G.A. Dielectric Properties of Frog Tissues in Vivo and in Vitro. *Phys. Med. Biol.* **1985**, *30*, 117–124. [[CrossRef](#)] [[PubMed](#)]
48. Gabriel, S.; Lau, R.W.; Gabriel, C. The Dielectric Properties of Biological Tissues: II. Measurements in the Frequency Range 10 Hz to 20 GHz. *Phys. Med. Biol.* **1996**, *41*, 2251–2269. [[CrossRef](#)] [[PubMed](#)]
49. Peyman, A.; Holden, S.; Gabriel, C. Mobile Telecommunications and Health Research Programme: Dielectric Properties of Tissues at Microwave Frequencies; Microwave Consultants Limited: London, UK, 2005.
50. Abdilla, L.; Sammut, C.; Mangion, L. Dielectric Properties of Muscle and Liver from 500 MHz–40 GHz.
51. *Electromagn. Biol. Med.* **2013**, *32*, 244–252. [[CrossRef](#)] [[PubMed](#)]
52. Schwan, H.P.; Foster, K.R. RF Field Interactions with Biological Systems: Electrical Properties and Biophysical Mechanisms. *Proc. IEEE* **1980**, *68*, 104–113. [[CrossRef](#)]

53. Foster, K.; Schwan, H. Dielectric Properties of Tissues and Biological Materials: A Critical Review. *Crit. Rev. Biomed. Eng.* **1989**, *17*, 25–104. [[PubMed](#)]
54. Gabriel, S.; Lau, R.W.; Gabriel, C. The Dielectric Properties of Biological Tissues: III. Parametric Models for the Dielectric Spectrum of Tissues. *Phys. Med. Biol.* **1996**, *41*, 2271–2293. [[CrossRef](#)] [[PubMed](#)]
55. Gregory, A.; Clarke, R.; Hodgetts, T.; Symm, G. *RF and Microwave Dielectric Measurements upon Layered Materials Using Coaxial Sensors*; NPL Report MAT 13; National Physical Laboratory: Teddington, UK, 2008.
56. Gulich, R.; Köhler, M.; Lunkenheimer, P.; Loidl, A. Dielectric Spectroscopy on Aqueous Electrolytic Solutions.
57. *Radiat. Environ. Biophys.* **2009**, *48*, 107–114. [[CrossRef](#)] [[PubMed](#)]
58. England, T.S.; Sharples, N.A.A. Dielectric Properties of the Human Body in the Microwave Region of the Spectrum. *Nature* **1949**, *163*, 487–488. [[CrossRef](#)] [[PubMed](#)]
59. Cook, H.F. The Dielectric Behaviour of Some Types of Human Tissues at Microwave Frequencies. *Br. J. Appl. Phys.* **1951**, *2*, 295–300. [[CrossRef](#)]
60. Schwan, H.P. Electrical Properties of Tissue and Cell Suspensions. *Adv. Biol. Med. Phys.* **1957**, *5*, 147–209. [[CrossRef](#)] [[PubMed](#)]
61. Schwan, H.P.; Li, K. Capacity and Conductivity of Body Tissues at Ultrahigh Frequencies. *Proc. IRE* **1953**, *41*, 1735–1740. [[CrossRef](#)]
62. Stuchly, M.A.; Stuchly, S.S. Dielectric Properties of Biological Substances—Tabulated. *J. Microw. Power* **1980**,
63. *15*, 19–25. [[CrossRef](#)]
64. Burdette, E.C.; Friederich, P.G.; Seaman, R.L.; Larsen, L.E. In Situ Permittivity of Canine Brain: Regional Variations and Postmortem Changes. *IEEE Trans. Microw. Theory Tech.* **1986**, *34*, 38–50. [[CrossRef](#)]
65. Smith, S.R.; Foster, K.R. Dielectric Properties of Low-Water-Content Tissues. *Phys. Med. Biol.* **1985**, *30*, 965–973. [[CrossRef](#)] [[PubMed](#)]
66. Zhadobov, M.; Augustine, R.; Sauleau, R.; Alekseev, S.; Di Paola, A.; Le Quément, C.; Mahamoud, Y.S.; Le Dréan, Y. Complex Permittivity of Representative Biological Solutions in the 2–67 GHz Range. *Bioelectromagnetics* **2012**, *33*, 346–355. [[CrossRef](#)] [[PubMed](#)]
67. Di Meo, S.; Martellosio, A.; Pasion, M.; Bozzi, M.; Perregrini, L.; Mazzanti, A.; Svelto, F.; Summers, P.; Renne, G.; Preda, L.; et al. Experimental Validation of the Dielectric Permittivity of Breast Cancer Tissues up to 50 GHz. In Proceedings of the IEEE MTT-S International Microwave Workshop Advanced Materials and Processes for RF and THz Applications (IMWS-AMP), Pavia, Italy, 20–22 September 2017; pp. 20–22.
68. Stuchly, M.A.; Stuchly, S.S. Coaxial Line Reflection Methods for Measuring Dielectric Properties of Biological Substances at Radio and Microwave Frequencies—A Review. *IEEE Trans. Instrum. Meas.* **1980**, *29*, 176–183. [[CrossRef](#)]
69. Athey, T.W.; Stuchly, M.A.; Stuchly, S.S. Measurement of Radio Frequency Permittivity of Biological Tissues with an Open-Ended Coaxial Line: Part I. *IEEE Trans. Microw. Theory Tech.* **1982**, *30*, 82–86. [[CrossRef](#)]
70. Gabriel, C.; Grant, E.H.; Young, I.R. Use of Time Domain Spectroscopy for Measuring Dielectric Properties with a Coaxial Probe. *J. Phys. E* **1986**, *19*, 843–846. [[CrossRef](#)]
71. Foster, K.R.; Schepps, J.L.; Stoy, R.D.; Schwan, H.P. Dielectric Properties of Brain Tissue between 0.01 and 10 GHz. *Phys. Med. Biol.* **1979**, *24*, 1177–1187. [[CrossRef](#)] [[PubMed](#)]
72. Surowiec, A.; Stuchly, S.S.; Eidus, L.; Swarup, A. In Vitro Dielectric Properties of Human Tissues at Radiofrequencies. *Phys. Med. Biol.* **1987**, *32*, 615. [[CrossRef](#)] [[PubMed](#)]
73. Pethig, R. Dielectric Properties of Biological Materials: Biophysical and Medical Applications. *IEEE Trans. Electr. Insul.* **1984**, *EI-19*, 453–474. [[CrossRef](#)]
74. Schepps, J.L.; Foster, K.R. The UHF and Microwave Dielectric Properties of Normal and Tumour Tissues: Variation in Dielectric Properties with Tissue Water Content. *Phys. Med. Biol.* **1980**, *25*, 1149. [[CrossRef](#)] [[PubMed](#)]

75. Gabriel, C.; Gabriel, S.; Corthout, E. The Dielectric Properties of Biological Tissues: I. Literature Survey. *Phys. Med. Biol.* **1996**, *41*, 2231–2249. [[CrossRef](#)] [[PubMed](#)]
76. Gabriel, C. *Compilation of the Dielectric Properties of Body Tissues at RF and Microwave Frequencies*; Report N.AL/OE-TR-1996-0037; Occupational and Environmental Health Directorate, Radiofrequency Radiation Division: Brooks Air Force Base, TX, USA, 1996.
77. Federal Communications Commission. *Tissue Dielectric Properties*; FCC: Washington, DC, USA, 2008. Available online: <https://www.fcc.gov/general/body-tissue-dielectric-parameters> (accessed on 30 October 2017).
78. Andreuccetti, D.; Fossi, R.; Petrucci, C. *An Internet Resource for the Calculation of the Dielectric Properties of Body Tissues in the Frequency Range 10 Hz–100 GHz*; IFAC-CNR: Florence, Italy, 1997; Available online: <http://niremf.ifac.cnr.it/tissprop/> (accessed on 4 June 2018).
79. Alanen, E.; Lahtinen, T.; Nuutinen, J. Variational Formulation of Open-Ended Coaxial Line in Contact with Layered Biological Medium. *IEEE Trans. Biomed. Eng.* **1998**, *45*, 1241–1248. [[CrossRef](#)] [[PubMed](#)]
80. Hagl, D.; Popovic, D.; Hagness, S.C.; Booske, J.H.; Okoniewski, M. Sensing Volume of Open-Ended Coaxial Probes for Dielectric Characterization of Breast Tissue at Microwave Frequencies. *IEEE Trans. Microw. Theory Tech.* **2003**, *51*, 1194–1206. [[CrossRef](#)]
81. Popovic, D.; Okoniewski, M.; Hagl, D.; Booske, J.H.; Hagness, S.C. Volume Sensing Properties of Open Ended Coaxial Probes for Dielectric Spectroscopy of Breast Tissue. In Proceedings of the IEEE Antennas and Propagation Society, Boston, MA, USA, 8–13 July 2001; pp. 254–257.
82. Popovic, D.; McCartney, L.; Beasley, C.; Lazebnik, M.; Okoniewski, M.; Hagness, S.C.; Booske, J.H. Precision Open-Ended Coaxial Probes for in Vivo and Ex Vivo Dielectric Spectroscopy of Biological Tissues at Microwave Frequencies. *IEEE Trans. Microw. Theory Tech.* **2005**, *53*, 1713–1721. [[CrossRef](#)]
83. Taylor, B.N.; Kuyatt, C.E. *Guidelines for Evaluating and Expressing the Uncertainty of NIST Measurement Results*; NIST Technical Note 1297; US Department of Commerce, Technology Administration, National Institute of Standards and Technology: Gaithersburg, MD, USA, 1994.
84. Gabriel, C.; Peyman, A. Dielectric Measurement: Error Analysis and Assessment of Uncertainty.
85. *Phys. Med. Biol.* **2006**, *51*, 6033–6046. [[CrossRef](#)] [[PubMed](#)]
86. Lazebnik, M.; Popovic, D.; McCartney, L.; Watkins, C.B.; Lindstrom, M.J.; Harter, J.; Sewall, S.; Ogilvie, T.; Magliocco, A.; Breslin, T.M.; et al. A Large-Scale Study of the Ultrawideband Microwave Dielectric Properties of Normal, Benign and Malignant Breast Tissues Obtained from Cancer Surgeries. *Phys. Med. Biol.* **2007**, *52*, 6093–6115. [[CrossRef](#)] [[PubMed](#)]
87. Chaudhary, S.S.; Mishra, R.K.; Swarup, A.; Thomas, J.M. Dielectric Properties of Normal & Malignant Human Breast Tissues at Radiowave & Microwave Frequencies. *Indian J. Biochem. Biophys.* **1984**, *21*, 76–79. [[PubMed](#)]
88. Joines, W.T.; Zhang, Y.; Li, C.; Jirtle, R.L. The Measured Electrical Properties of Normal and Malignant Human Tissues from 50 to 900 MHz. *Med. Phys.* **1994**, *21*, 547–550. [[CrossRef](#)] [[PubMed](#)]
89. Martellosio, A.; Pasian, M.; Bozzi, M.; Perregrini, L.; Mazzanti, A.; Svelto, F.; Summers, P.E.; Renne, G.; Preda, L.; Bellomi, M. Dielectric Properties Characterization from 0.5 to 50 GHz of Breast Cancer Tissues. *IEEE Trans. Microw. Theory Tech.* **2017**, *65*, 998–1011. [[CrossRef](#)]
90. Meaney, P.M.; Gregory, A.; Epstein, N.; Paulsen, K.D. Microwave Open-Ended Coaxial Dielectric Probe: Interpretation of the Sensing Volume Re-Visited. *BMC Med. Phys.* **2014**, *14*, 1–11. [[CrossRef](#)] [[PubMed](#)]
91. Meaney, P.M.; Gregory, A.P.; Seppälä, J.; Lahtinen, T. Open-Ended Coaxial Dielectric Probe Effective Penetration Depth Determination. *IEEE Trans. Microw. Theory Tech.* **2016**, *64*, 915–923. [[CrossRef](#)] [[PubMed](#)]
92. Porter, E.; La Gioia, A.; Santorelli, A.; O'Halloran, M. Modeling of the Dielectric Properties of Biological Tissues within the Histology Region. *IEEE Trans. Dielectr. Electr. Insul.* **2017**, *24*, 3290–3301. [[CrossRef](#)]

93. Porter, E.; O'Halloran, M. Investigation of Histology Region in Dielectric Measurements of Heterogeneous Tissues. *IEEE Trans. Dielectr. Electr. Insul.* **2017**, *65*, 5541–5552. [[CrossRef](#)]
94. Peyman, A.; Kos, B.; Djokić, M.; Trotošek, B.; Limbaeck-Stokin, C.; Serša, G.; Miklavčič, D. Variation in Dielectric Properties Due to Pathological Changes in Human Liver. *Bioelectromagnetics* **2015**, *36*, 603–612. [[CrossRef](#)] [[PubMed](#)]
95. Sugitani, T.; Arihiro, K.; Kikkawa, T. Comparative Study on Dielectric Constants and Conductivities of Invasive Ductal Carcinoma Tissues. *IEEE Eng. Med. Biol. Soc.* **2015**, 4387–4390. [[CrossRef](#)]
96. Sabouni, A.; Hahn, C.; Noghianian, S.; Sauter, E.; Weiland, T. Study of the Effects of Changing Physiological Conditions on Dielectric Properties of Breast Tissues. *ISRN Biomed. Imaging* **2013**, *2013*, 894153. [[CrossRef](#)]
97. Reinecke, T.; Hagemeyer, L.; Schulte, V.; Klintschar, M.; Zimmermann, S. Quantification of Edema in Human Brain Tissue by Determination of Electromagnetic Parameters. In Proceedings of the IEEE Sensors, Baltimore, MD, USA, 3–6 November 2013; pp. 1–4.
98. Nicolson, A.; Ross, G.F. Measurement of the Intrinsic Properties of Materials by Time-Domain Techniques. *IEEE Trans. Instrum. Meas.* **1970**, *19*, 377–382. [[CrossRef](#)]
100. Weir, W.B. Automatic Measurement of Complex Dielectric Constant and Permeability. *Proc. IEEE* **1974**, *62*, 33–36. [[CrossRef](#)]
101. Baker-Jarvis, J.; Vanzura, E.J.; Kissick, W.A. Improved Technique for Determining Complex Permittivity with the Transmission/Reflection Method. *IEEE Trans. Microw. Theory Tech.* **1990**, *38*, 1096–1103. [[CrossRef](#)]
102. Kim, S.; Baker-Jarvis, J. An Approximate Approach To Determining the Permittivity and Permeability near $\lambda/2$ Resonances in Transmission/Reflection Measurements. *Prog. Electromagn. Res. B* **2014**, *58*, 95–109. [[CrossRef](#)]
103. Boughriet, A.H.; Legrand, C.; Chapoton, A. Noniterative Stable Transmission/Reflection Method for Low-Loss Material Complex Permittivity Determination. *IEEE Trans. Microw. Theory Tech.* **1997**, *45*, 52–57. [[CrossRef](#)]
104. Baker-Jarvis, J.; Janezic, M.; Domich, P.; Geyer, R. Analysis of an Open-Ended Coaxial Probe with Lift-off for Non Destructive Testing. *IEEE Trans. Instrum. Meas.* **1994**, *43*, 1–8. [[CrossRef](#)]
105. Gregory, A.; Clarke, R. A Review of RF and Microwave Techniques for Dielectric Measurements on Polar Liquids. *IEEE Trans. Dielectr. Electr. Insul.* **2006**, *13*, 727–743. [[CrossRef](#)]
106. Agilent. *Basics of Measuring the Dielectric Properties of Materials*; Agilent Technologies: Santa Clara, CA, USA, 2005.
107. Land, D.V.; Campbell, A.M. A Quick Accurate Method for Measuring the Microwave Dielectric Properties of Small Tissue Samples. *Phys. Med. Biol.* **1992**, *37*, 183. [[CrossRef](#)] [[PubMed](#)]
108. Campbell, A.; Land, D.V. Dielectric Properties of Female Human Breast Tissue Measured in Vitro at 3.2 GHz. *Phys. Med. Biol.* **1992**, *37*, 193–210. [[CrossRef](#)] [[PubMed](#)]
110. Peng, Z.; Hwang, J.Y.; Andriese, M. Maximum Sample Volume for Permittivity Measurements by Cavity Perturbation Technique. *IEEE Trans. Instrum. Meas.* **2014**, *63*, 450–455. [[CrossRef](#)]
111. Campbell, A. Measurements and Analysis of the Microwave Dielectric Properties of Tissues. *J. Appl. Phys.* **1990**, *22*, 95.
113. Ramos, A.; Bertemes-Filho, P. Numerical Sensitivity Modeling for the Detection of Skin Tumors by Using Tetrapolar Probe. *Electromagn. Biol. Med.* **2011**, *30*, 235–245. [[CrossRef](#)] [[PubMed](#)]

114. Raghavan, K.; Porterfield, J.E.; Kottam, A.T.G.; Feldman, M.D.; Escobedo, D.; Valvano, J.W.; Pearce, J.A. Electrical Conductivity and Permittivity of Murine Myocardium. *IEEE Trans. Biomed. Eng.* **2009**, *56*, 2044–2053. [[CrossRef](#)] [[PubMed](#)]
115. Karki, B.; Wi, H.; McEwan, A.; Kwon, H.; Oh, T.I.; Woo, E.J.; Seo, J.K. Evaluation of a Multi-Electrode Bioimpedance Spectroscopy Tensor Probe to Detect the Anisotropic Conductivity Spectra of Biological Tissues. *Meas. Sci. Technol.* **2014**, *25*, 075702. [[CrossRef](#)]
116. Misra, D.K. A Quasi-Static Analysis of Open-Ended Coaxial Lines. *IEEE Trans. Microw. Theory Tech.* **1987**, *35*, 925–928. [[CrossRef](#)]
117. Grant, J.P.; Clarke, R.N.; Symm, G.T.; Spyron, N.M. A Critical Study of the Open-Ended Coaxial-Line Sensor Technique for RF and Microwave Complex Permittivity Measurements. *J. Phys. E Sci. Instrum.* **1989**, *22*, 757–770. [[CrossRef](#)]
118. Jenkins, S.; Preece, A.W.; Hodgetts, T.E.; Symm, G.T.; Warham, A.G.P.; Clarke, R.N. Comparison of Three Numerical Treatments for the Open-Ended Coaxial Line Sensor. *Electron. Lett.* **1990**, *26*, 234–236. [[CrossRef](#)]
119. Misra, D. On the Measurement of the Complex Permittivity of Materials by an Open-Ended Coaxial Probe. *IEEE Microw. Guid. Wave Lett.* **1995**, *5*, 161–163. [[CrossRef](#)]
120. Perez Cesaretti, M.D. General Effective Medium Model for the Complex Permittivity Extraction with an Open-Ended Coaxial Probe in Presence of a Multilayer Material under Test. Ph.D. Thesis, University of Bologna, Bologna, Italy, 2012.
121. Keysight Technologies. *Keysight E5063A ENA Series Network Analyzer*; Keysight Technologies: Santa Clara, CA, USA, 2015.
122. Gabriel, C.; Chan, T.Y.; Grant, E.H. Admittance Models for Open Ended Coaxial Probes and Their Place in Dielectric Spectroscopy. *Phys. Med. Biol.* **1994**, *39*, 2183–2200. [[CrossRef](#)] [[PubMed](#)]
123. Berube, D.; Ghannouchi, F.M.; Savard, P. A Comparative Study of Four Open-Ended Coaxial Probe Models for Permittivity Measurements of Lossy Dielectric/Biological Materials at Microwave Frequencies. *IEEE Trans. Microw. Theory Tech.* **1996**, *44*, 1928–1934. [[CrossRef](#)]
124. Zajíček, R.; Oppl, L.; Vrba, J. Broadband Measurement of Complex Permittivity Using Reflection Method and Coaxial Probes. *Radioengineering* **2008**, *17*, 14–19.
125. Schwan, H.P.; Foster, K.R. Microwave Dielectric Properties of Tissue. Some Comments on the Rotational Mobility of Tissue Water. *Biophys. J.* **1977**, *17*, 193–197. [[CrossRef](#)]
126. Peyman, A. Dielectric Properties of Tissues; Variation with Structure and Composition. In Proceedings of the International Conference on Electromagnetics in Advanced Applications (ICEAA), Torino, Italy, 14–18 September 2009; pp. 863–864.
127. Popovic, D.; Okoniewski, M. Effects of Mechanical Flaws in Open-Ended Coaxial Probes for Dielectric Spectroscopy. *IEEE Microw. Wirel. Components Lett.* **2002**, *12*, 401–403. [[CrossRef](#)]
128. Keysight. N1501A Dielectric Probe Kit 10 MHz to 50 GHz: Technical Overview. 2015. Available online: <http://www.Keysight.Com/En/Pd-2492144-Pn-N1501A/Dielectric-Probe-Kit> (accessed on 30 October 2017).
129. Karacolak, T.; Cooper, R.; Unlu, E.S.; Topsakal, E. Dielectric Properties of Porcine Skin Tissue and in Vivo Testing of Implantable Antennas Using Pigs as Model Animals. *IEEE Antennas Wirel. Propag. Lett.* **2012**, *11*, 1686–1689. [[CrossRef](#)]
130. Nyshadham, A.; Sibbald, C.L.; Stuchly, S.S. Permittivity Measurements Using Open-Ended Sensors and Reference Liquid Calibration—An Uncertainty Analysis. *IEEE Trans. Microw. Theory Tech.* **1992**, *40*, 305–314. [[CrossRef](#)]
131. Marsland, T.P.; Evans, S. Dielectric Measurements with an Open-Ended Coaxial Probe. *IEE Proc. H Microw. Antennas Propag.* **1987**, *134*, 341–349. [[CrossRef](#)]
132. Piuze, E.; Merla, C.; Cannazza, G.; Zambotti, A.; Apollonio, F.; Cataldo, A.; D’Atanasio, P.; De Benedetto, E.; Liberti, M. A Comparative Analysis between Customized and Commercial

- Systems for Complex Permittivity Measurements on Liquid Samples at Microwave Frequencies. *IEEE Trans. Instrum. Meas.* **2013**, *62*, 1034–1046. [[CrossRef](#)]
135. Packard, H. Automating the HP 8410B Microwave Network Analyzer. *Appl. Note* **1980**, *221*, 1–25.
 136. Bobowski, J.S.; Johnson, T. Permittivity Measurements of Biological Samples by an Open-Ended Coaxial Line. *Prog. Electromagn. Res.* **2012**, *40*, 159–183. [[CrossRef](#)]
 137. Peyman, A.; Holden, S.J.; Watts, S.; Perrott, R.; Gabriel, C. Dielectric Properties of Porcine Cerebrospinal Tissues at Microwave Frequencies: In Vivo, in Vitro and Systematic Variation with Age. *Phys. Med. Biol.* **2007**, *52*, 2229–2245. [[CrossRef](#)] [[PubMed](#)]
 138. Smith, P.H. Transmission Line Calculator. *Electronics* **1939**, *12*, 29–31.
 139. Kaatze, U. Complex Permittivity of Water as a Function of Frequency and Temperature. *J. Chem. Eng. Data* **1989**, *34*, 371–374. [[CrossRef](#)]
 141. Anderson, J.M.; Sibbald, C.L.; Stuchly, S.S. Dielectric Measurements Using a Rational Function Model. *IEEE Trans. Microw. Theory Tech.* **1994**, *42*, 199–204. [[CrossRef](#)]
 143. De Langhe, P.; Blomme, K.; Martens, L.; De Zutter, D. Measurement of Low-Permittivity Materials Based on a Spectral-Domain Analysis for the Open-Ended Coaxial Probe. *IEEE Trans. Instrum. Meas.* **1993**, *42*, 879–886. [[CrossRef](#)]
 144. Peyman, A.; Gabriel, C.; Grant, E.H.; Vermeeren, G.; Martens, L. Variation of the Dielectric Properties of Tissues with Age: The Effect on the Values of SAR in Children When Exposed to Walkie-Talkie Devices. *Phys. Med. Biol.* **2009**, *54*, 227–241. [[CrossRef](#)] [[PubMed](#)]
 145. Salahuddin, S.; Porter, E.; Meaney, P.M.; O’Halloran, M. Effect of Logarithmic and Linear Frequency Scales on Parametric Modelling of Tissue Dielectric Data. *Biomed. Phys. Eng. Express* **2017**, *3*, 1–11. [[CrossRef](#)] [[PubMed](#)]
 146. Kraszewski, A.; Stuchly, M.A.; Stuchly, S.S. ANA Calibration Method for Measurements of Dielectric Properties. *IEEE Trans. Instrum. Meas.* **1983**, *32*, 385–387. [[CrossRef](#)]
 147. Buchner, R.; Hefter, G.T.; May, M.P. Dielectric Relaxation of Aqueous NaCl Solutions. *J. Phys. Chem.* **1999**, *103*, 1–9. [[CrossRef](#)]
 149. Wei, Y.Z.; Sridhar, S. Radiation-Corrected Open-Ended Coax Line Technique for Dielectric Measurements of Liquids up to 20 GHz. *IEEE Trans. Microw. Theory Tech.* **1991**, *39*, 526–531. [[CrossRef](#)]
 150. Gregory, A.P.; Clarke, R.N. *Tables of the Complex Permittivity of Dielectric Reference Liquids at Frequencies up to 5 GHz*; NPL Report MAT 23; National Physical Laboratory: Teddington, UK, 2012.
 151. Peyman, A.; Gabriel, C.; Grant, E.H. Complex Permittivity of Sodium Chloride Solutions at Microwave Frequencies. *Bioelectromagnetics* **2007**, *28*, 264–274. [[CrossRef](#)] [[PubMed](#)]
 152. Jordan, B.P.; Sheppard, R.J.; Szwarnowski, S. The Dielectric Properties of Formamide, Ethanediol and Methanol. *J. Phys. D Appl. Phys.* **1978**, *11*, 695–701. [[CrossRef](#)]
 153. Barthel, J.; Buchner, R. High Frequency Permittivity and Its Use in the Investigation of Solution Properties. *Pure Appl. Chem.* **1991**, *63*, 1473–1482. [[CrossRef](#)]
 155. Stogryn, A. Equations for Calculating the Dielectric Constant of Saline Water. *IEEE Trans. Microw. Theory Tech.* **1971**, *19*, 733–736. [[CrossRef](#)]
 157. Nortemann, K.; Hilland, J.; Kaatze, U. Dielectric Properties of Aqueous NaCl Solutions at Microwave Frequencies. *J. Phys. Chem. A* **1997**, *101*, 6864–6869. [[CrossRef](#)]
 158. Lamkaouchi, K.; Balana, A.; Delbos, G.; Ellison, W.J. Permittivity Measurements of Lossy Liquids in the Range 26-110 GHz. *Meas. Sci. Technol.* **2003**, *14*, 444–450. [[CrossRef](#)]
 159. Kaatze, U.; Pottel, R.; Schaefer, M. Dielectric Spectrum of Dimethyl Sulfoxide/Water Mixtures as a Function of Composition. *J. Phys. Chem.* **1989**, *93*, 5623–5627. [[CrossRef](#)]

160. Vij, J.K.; Grochulski, T.; Kocot, A.; Hufnagel, F. Complex Permittivity Measurements of Acetone in the Frequency Region 50–310 GHz. *Mol. Phys.* **1991**, *72*, 353–361. [[CrossRef](#)]
161. Gregory, A.P.; Clarke, R.N. Dielectric Metrology with Coaxial Sensors. *Meas. Sci. Technol.* **2007**, *18*, 1372–1386. [[CrossRef](#)]
162. Peyman, A.; Rezazadeh, A.; Gabriel, C. Changes in the Dielectric Properties of Rat Tissue as a Function of Age at Microwave Frequencies. *Phys. Med. Biol.* **2001**, *46*, 1617–1629. [[CrossRef](#)] [[PubMed](#)]
163. Chen, G.; Li, K.; Ji, Z. Bilayered Dielectric Measurement With an Open-Ended Coaxial Probe. *IEEE Trans. Microw. Theory Tech.* **1994**, *42*, 966–971. [[CrossRef](#)]
164. Huclova, S.; Baumann, D.; Talary, M.; Fröhlich, J. Sensitivity and Specificity Analysis of Fringing-Field Dielectric Spectroscopy Applied to a Multi-Layer System Modelling the Human Skin. *Phys. Med. Biol.* **2011**, *56*, 7777–7793. [[CrossRef](#)] [[PubMed](#)]
165. Meaney, P.M.; Golnabi, A.; Fanning, M.W.; Geimer, S.D.; Paulsen, K.D. Dielectric Volume Measurements for Biomedical Applications. In Proceedings of the 13th International Symposium on Antenna Technology and Applied Electromagnetics and the Canadian Radio Sciences Meeting, Toronto, ON, Canada, 15–18 February 2009.
166. Johnson, C.C.; Guy, A.W. Nonionizing Electromagnetic Wave Effects in Biological Materials and Systems.
167. *Proc. IEEE* **1972**, *60*, 692–718. [[CrossRef](#)]
168. Shahzad, A.; Sonja, K.; Jones, M.; Dwyer, R.M.; O'Halloran, M. Investigation of the Effect of Dehydration on Tissue Dielectric Properties in Ex Vivo Measurements. *Biomed. Phys. Eng. Express* **2017**, *3*, 1–9. [[CrossRef](#)]
169. Farrugia, L.; Wismayer, P.S.; Mangion, L.Z.; Sammut, C.V. Accurate in Vivo Dielectric Properties of Liver from 500 MHz to 40 GHz and Their Correlation to Ex Vivo Measurements. *Electromagn. Biol. Med.* **2016**, *8378*, 1–9. [[CrossRef](#)]
170. Nopp, P.; Rapp, E.; Pfützner, H.; Nakesch, H.; Ruhsam, C. Dielectric Properties of Lung Tissue as a Function of Air Content. *Phys. Med. Biol.* **1993**, *38*, 699–716. [[CrossRef](#)] [[PubMed](#)]
171. Gabriel, C.; Peyman, A.; Grant, E.H. Electrical Conductivity of Tissue at Frequencies below 1 MHz.
172. *Phys. Med. Biol.* **2009**, *54*, 4863–4878. [[CrossRef](#)] [[PubMed](#)]
173. Haemmerich, D.; Ozkan, R.; Tungjitkusolmun, S.; Tsai, J.Z.; Mahvi, D.; Staelin, S.T.; Webster, J.G. Changes in Electrical Resistivity of Swine Liver after Occlusion and Postmortem. *Med. Biol. Eng. Comput.* **2002**, *40*, 29–33. [[CrossRef](#)] [[PubMed](#)]
174. Ranck, J.B.; Bement, S.L. The Specific Impedance of the Dorsal Columns of Cat: An Anisotropic Medium.
175. *Exp. Neurol.* **1965**, *11*, 451–463. [[CrossRef](#)]
176. Hart, F.X.; Dunfee, W.R. In Vivo Measurement of the Low-Frequency Dielectric Spectra of Frog Skeletal Muscle. *Phys. Med. Biol.* **1993**, *38*, 1099–1112. [[CrossRef](#)] [[PubMed](#)]
177. Lopresto, V.; Pinto, R.; Farina, L.; Cavagnaro, M. Treatment Planning in Microwave Thermal Ablation: Clinical Gaps and Recent Research Advances. *Int. J. Hyperth.* **2017**, *33*, 83–100. [[CrossRef](#)] [[PubMed](#)]
178. Young, B.; Woodford, P.; O'Dowd, G. *Wheater's Functional Histology: A Text and Colour Atlas*, 6th ed.; Elsevier Health Sciences: London, UK, 2013.
179. Cross, S.S. Grading and Scoring in Histopathology. *Histopathology* **1998**, *33*, 99–106. [[CrossRef](#)] [[PubMed](#)]
180. Veta, M.; Pluim, J.P.W.; Van Diest, P.J.; Viergever, M.A. Breast Cancer Histopathology Image Analysis: A Review. *IEEE Trans. Biomed. Eng.* **2014**, *61*, 1400–1411. [[CrossRef](#)] [[PubMed](#)]
181. National Health Service (NHS). *Pathology*; National Health Service (NHS): London, UK, 2016.
182. Verkooijen, H.M.; Peterse, J.L.; Schipper, M.E.I.; Buskens, E.; Hendriks, J.H.C.L.; Pijnappel, R.M.; Peeters, P.H.M.; Borel Rinkes, I.H.M.; Mali, W.P.T.M.; Holland, R. Interobserver Variability between General and Expert Pathologists during the Histopathological Assessment

- of Large-Core Needle and Open Biopsies of Non-Palpable Breast Lesions. *Eur. J. Cancer* **2003**, *39*, 2187–2191. [[CrossRef](#)]
183. Gomes, D.S.; Porto, S.S.; Balabram, D.; Gobbi, H. Inter-Observer Variability between General Pathologists and a Specialist in Breast Pathology in the Diagnosis of Lobular Neoplasia, Columnar Cell Lesions, Atypical Ductal Hyperplasia and Ductal Carcinoma in Situ of the Breast. *Diagn. Pathol.* **2014**, *9*, 121. [[CrossRef](#)] [[PubMed](#)]
184. Gage, J.C.; Schiffman, M.; Hunt, W.C.; Joste, N.; Ghosh, A.; Wentzensen, N.; Wheeler, C.M. Cervical Histopathology Variability among Laboratories: A Population-Based Statewide Investigation. *Am. J. Clin. Pathol.* **2013**, *139*, 330–335. [[CrossRef](#)] [[PubMed](#)]
185. Bruggeman, D.A.G. Berechnung Verschiedener Physikalischer Konstanten von Heterogenen Substanzen. 1. Dielektizitätskonstanten Und Leitfähigkeiten Der Mischkörper Aus Isotropen Substanzen. *Ann. Phys.* **1935**, *24*, 636–679. [[CrossRef](#)]

7. Real-Time Brain Stroke Detection Through a Learning-by-Examples Technique—An Experimental Assessment

This chapter is based on following published paper:

Marco Salucci, Jan Vrba, Ilya Merunka, Andrea Massa:

“Real-time brain stroke detection through a learning-by-examples technique—An experimental assessment”,

**Microwave and Optical Technology Letters. 2017; 59: 2796–2799
(Q4, IF = 0,95, 9 citations w/o selfcitations)**

Doi: <https://doi.org/10.1002/mop.30821>

Real-Time Brain Stroke Detection Through a Learning-by-Examples Technique—An Experimental Assessment

Abstract

The real-time detection of brain strokes is addressed within the Learning-by-Examples (LBE) framework. Starting from scattering measurements at microwave regime, a support vector machine (SVM) is exploited to build a robust decision function able to infer in real-time whether a stroke is present or not in the patient head. The proposed approach is validated in a laboratory-controlled environment by considering experimental measurements for both training and testing SVM phases. The obtained results prove that a very high detection accuracy can be yielded even though using a limited amount of training data.

Keywords

brain stroke detection, experimental validation, learning-by-examples, support vector machines

7.1 Introduction

Sensing matter through electromagnetic (EM) waves is nowadays widely spread in many scenarios ranging from subsurface investigations [1,2] to non-destructive testing and evaluation (NDT-NDE) [3] as well as medical applications [4-8].

Recently, the use of microwave probing modalities for estimating the dielectric characteristics of human brain tissues has attracted a lot of attention [7,8]. Unlike computed tomography (CT) and magnetic resonance (MR), microwave imaging (MI) exploits non-ionizing radiation, and it can be implemented with low-cost equipments. On the other hand, processing the scattered signal for reliable diagnoses of the human head is a very challenging task due to the presence of biological media with losses [8]. Regardless of the imaging modality, a rapid identification of the presence of a stroke (ischemic or hemorrhagic) is of fundamental importance to apply suitable treatments and prevent permanent consequences to the patient. Toward such a real-time working, learning-by-examples (LBE) techniques [9] could be a promising candidate approach since they proved to fit such a time requirement in other field of applications [3, 10].

Following this line of reasoning and within the MI framework, this work formulates the brain stroke detection as a binary classification problem solved by means of a support vector machine (SVM) algorithm. During a preliminary off-line phase, a database of input/output (I/O) pairs (i.e., presence of the stroke in a known position of the head vs. scattering measurements collected by an array of antennas) is generated to build a decision function, then used during the online phase to make real-time predictions of the human head conditions (i.e., the presence or not of a stroke). An experimental validation carried out in a laboratory controlled environment with a simplified—but realistic—phantom, is performed to preliminary assess the effectiveness of the proposed implementation besides numerical tests with synthetically generated data.

7.2 Mathematical formulation

Let us consider a three-dimensional (3D) MI system where the investigation domain D_{inv} coincides with the volume of a human head model (Figure 7.1). Moreover, let us model the presence of a stroke as a volumetric discontinuity of the dielectric properties with respect to the background medium of electric permittivity ϵ_{rb} and conductivity σ_b (i.e., $\epsilon_r(\mathbf{r}) \neq \epsilon_{rb}$ and $\sigma(\mathbf{r}) \neq \sigma_b$ for $\mathbf{r} \in V$. V being the volume of the stroke). Such a scenario is probed by a set of A antennas located in an external observation domain D_{obs} surrounding D_{inv} at the positions $\mathbf{r}_a=(X_a, Y_a, Z_a)$, $a=1, \dots, A$ (Figure 7.2). During the acquisition phase, each antenna successively illuminates

the domain D_{inv} with a time-harmonic electromagnetic signal at frequency f , while the scattered field is measured by the remaining $(A - 1)$ antennas. As a result, the following $(A \times A)$ scattering matrix is built

$$\underline{S} = \begin{bmatrix} S_{11} & S_{12} & \cdots & S_{1A} \\ S_{21} & S_{22} & \cdots & S_{2A} \\ \vdots & & \ddots & \vdots \\ S_{A1} & S_{A2} & \cdots & S_{AA} \end{bmatrix} \quad (1)$$

where the generic (a, b) -th entry is given by

$$S_{ab} = \frac{V_a^-}{V_b^+} \quad (2)$$

V_a^- and V_b^+ being the reflected voltage at the a th port and the incident voltage at the b th port, respectively. Because of the reciprocity principle, the set of mutually independent measurements is composed by the $Q = (A + 1)A/2$ scattering coefficients lying above and within the diagonal of S (i.e.,

$$\{S_{ab}; a; b = 1; \dots; A; a \leq b\}.$$

Such measurements account for the presence (absence) of the stroke since the scattering phenomena arising from the probing waves and the pathology in D_{inv} cause a variation (or not) of the scattering parameters with respect to the stroke-free scenario. Starting from such an idea, the inverse problem of stroke detection from the scattered data is reformulated within the LBE framework as a binary classification one, then solved by means of a SVM algorithm [9]. More in detail, a set of N I/O pairs $\{\Psi^{(n)}, \chi(\Psi^{(n)}); n = 1, \dots, N\}$ is generated to model the electromagnetic relationships between scattered data/measurements, $\Psi^{(n)} = \{\Re(S_{ab}^{(n)}), \Im(S_{ab}^{(n)}); a, b = 1, \dots, A, a \leq b\}$, $\Re(\cdot), \Im(\cdot)$ being the real and imaginary parts, respectively, and the status of D_{inv} [i.e., $\chi(\Psi^{(n)}) = +1$ when the stroke is present, $\chi(\Psi^{(n)}) = -1$ without the stroke] during an off-line SVM training phase. The information “coded” in such a training set is then exploited to build the decision function

$$\tilde{\chi}(\Psi) = \text{sgn} \left(\sum_{n=1}^N \chi(\Psi^{(n)}) \alpha^{(n)} \kappa(\Psi^{(n)}, \Psi) + b \right). \quad (3)$$

adopted during the online test phase for predicting the status of D_{inv} in correspondence with a previously unseen set of scattering measurements Ψ . In (3), $\text{sgn}(\cdot)$ denotes the sign function, $0 \leq \alpha^{(n)} \geq C$ are Lagrange multipliers, $n = 1, \dots, N$, C being the so-called penalty factor, b is a bias term [9], while $\kappa(\Psi^{(n)}, \Psi) = \exp(-\gamma \|\Psi^{(n)} - \Psi\|)$, is the radial basis function (RBF) kernel function.

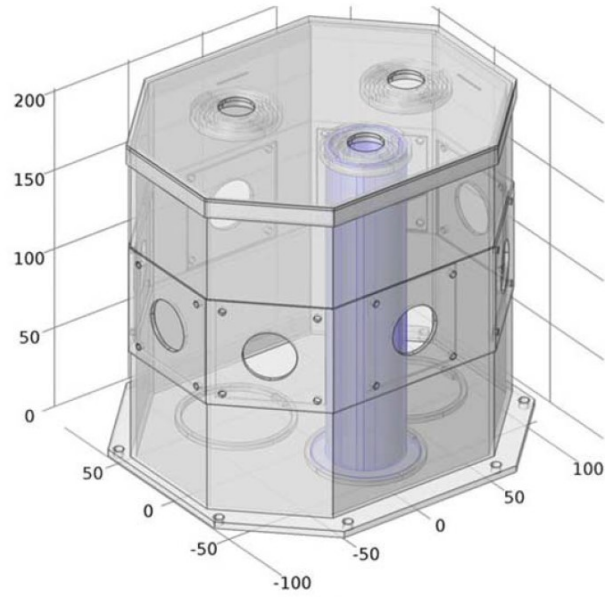


Figure 7.1, 3D view and of the head phantom (D_{inv}).

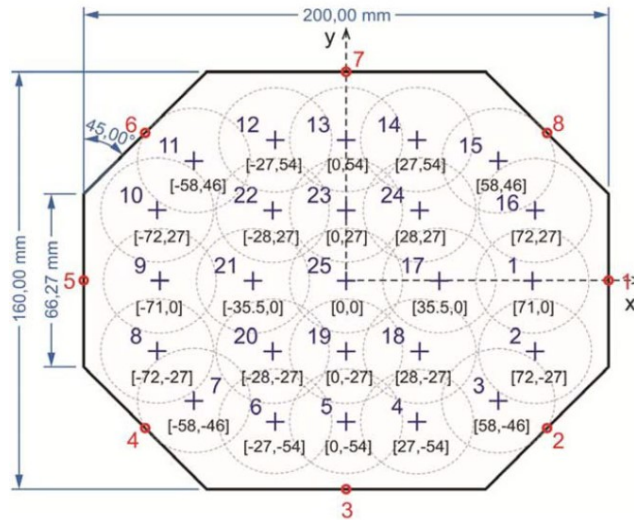


Figure 7.2, 2D section of the head phantom (D_{inv}): antennas positions (red dots) and admissible locations (blue crosses).

7.3 Experimental validation

The proposed real-time LBE-based approach, integrated within a suitably designed acquisition setup, has been validated against laboratory-controlled experimental data collected in a wide measurement campaign at the ELEDIA@ CTU laboratories, Czech Technical University, Prague, Czech Republic. An octagonal prism with dimensions compatible to a human head ($L_x=200$ mm, $L_y=160$ mm, $L_z=200$ mm—Figure 2) has been assumed as D_{inv} and it has been filled with a liquid mixture composed by 64.81 wt % of 1,2- propanediol, 0.79 wt % of NaCl, and 34.4 wt % of water ($\epsilon_r \approx 41.8$ and $\sigma_b \approx 0.97$ S/m at 22 °C and $f=900$ MHz) to emulate the electromagnetic behavior of the brain tissue (IEEE Std 1528–2013).

As for the stroke phantom, it has been modeled with a circular cylinder of diameter 40 mm and height 200 mm (Figure 7.3) manufactured using a 3D printing process. The cylinder has been filled with a liquid of dielectric characteristics $\epsilon_r \approx 32.04$ and $\sigma_b \approx 0.85$ S/m when dealing with an ischemic stroke, while another composition ($\epsilon_r \approx 48.63$ and $\sigma_b \approx 1.28$ S/m) has been selected to fit the hemorrhagic stroke behavior.

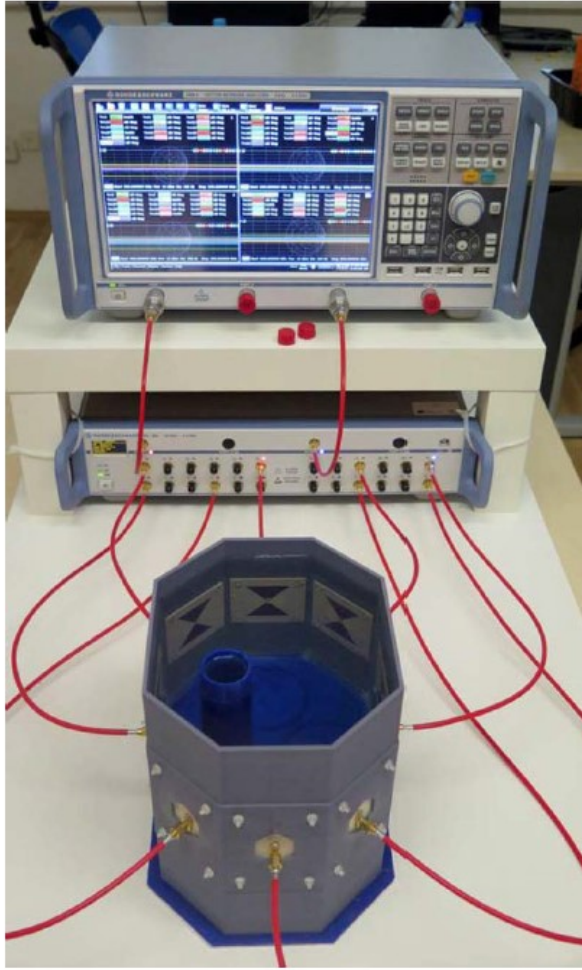


Figure 7.3, Experimental MI system for real-time brain stroke detection.

The head model has been surrounded by $A = 8$ bow-tie antennas printed over Rogers Duroid 4003C substrate of thickness 1.5 mm (Figure 7.3) without ground plane. Each probe has been fed by a coaxial cable without balun, while the acquisition system consisted of a vector network analyzer R&S ZNB4 and a microwave switching matrix R&S ZN-Z84 (Figure 7.3).

During the off-line SVM training phase, different training sets of increasing dimensions ($N=4, \dots, 2500$) have been generated by collecting the scattering measurements at different day times: $N^{(+1)} = N/2$ and $N^{(-1)} = N/2$ data with $(N/4)$ with the ischemic/hemorrhagic stroke randomly located over a fixed set of P525 positions (Figure 7.2) in D_{inv} and without the stroke.

To show the effectiveness of the developed LBE inversion strategy, Figure 7.4 shows the behavior of the classification accuracy (Γ) and error (Ξ) versus the dimension of the SVM training set when setting $C=1$ and $\gamma = 10^{-1}$, as found through a standard fivefold cross-validation approach, and testing over a set of previously unseen $M=500$ test scattering measurements.

As it can be observed, the prediction accuracy rapidly improves as new samples are added to the training set (Figure 7.4) reaching a perfect discrimination ($\Gamma=100\%$, $\Xi=0\%$) between class -1 (i.e., “without stroke”) and class +1 (i.e., “with stroke”) when processing a dataset of dimension $N \geq 50$ (Figure 7.4).

For completeness, Table 7.1 gives the number of false positives and negatives (i.e., test samples wrongly assigned to class -1 and +1) for a set of representative training sizes.

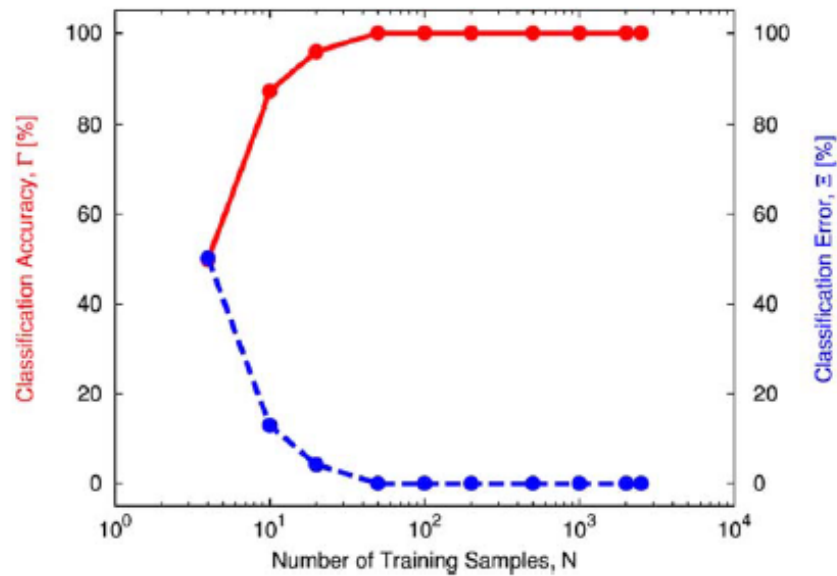


Figure 7.4, Behaviour of the classification accuracy and error versus the number of training samples considered during the off-line phase.

Table 7.1, the number of false positives and negatives (i.e., test samples wrongly assigned to class -1 and +1) for a set of representative training sizes

N	False negative (%)	False positive (%)
4	0.4	100
10	1.6	24.4
20	1.6	6.8
50	0.0	0.0

7.4 Conclusion

In this work, the real-time detection of a brain stroke starting from microwave scattering measurements has been addressed. The experimental validation of a SVM binary classification based approach when implemented in a suitable acquisition setup has pointed out that it is possible, even though in a simplified—but realistic—scenario to yield a very good detection accuracy also when processing smallsize training datasets. Of course, an improved modeling is needed and further extensions are currently under developments to deal with the discrimination between the two types of brain strokes.

Acknowledgments

This work benefited from the networking activities carried out within the SIRENA project (2014–2017) funded by DIGITEO (France) under the “Call for Chairs 2014.”

References

- [1] Lambot S, Giannopoulos A, Pajewski L, Slob E, Sato M. Foreword to the Special issue on advances in groundpenetrating radar research and applications. *IEEE J Staeors*. 2016;9:5–8.
- [2] Salucci M, Oliveri G, Massa A. GPR prospecting through an inverse-scattering frequency-hopping multifocusing approach. *IEEE Trans Geosci Remote Sens*. 2015;53:6573–6592.
- [3] Salucci M, Anselmi N, Oliveri G, et al. Real-time NDT-NDE through an innovative adaptive partial least squares SVR inversion approach. *IEEE Trans Geosci Remote Sens*. 2016;54:6818–6832.
- [4] Hagness S, Fear E, Massa A. Guest-Editorial: special cluster on microwave medical imaging. *IEEE Antennas Wireless Prop Lett*. 2012;11:1592–1597.
- [5] Grzegorzczuk TM, Meaney PM, Kaufman PA, Paulsen KD. Fast 3D tomographic microwave imaging for breast cancer detection. *IEEE Trans Med Imaging*. 2012;31:1584–1592.
- [6] Nguyen PT, Abbosh A, Crozier S. Three-dimensional microwave hyperthermia for breast cancer treatment in a realistic environment using particle swarm optimization. *IEEE Trans Biomed Eng*.
- [7] Marimuthu J, Bialkowski K, Abbosh AM. Software-defined radar for medical imaging. *IEEE Trans Microw Theory Techn*. 2016;64:643–652.
- [8] Zamani A, Abbosh AM, Mobashsher AT. Frequency-based multistatic microwave imaging algorithm with application to brain injury detection. *IEEE Trans Microw Theory Techn*. 2016;64: 653–662.
- [9] Cortes C, Vapnik V. Support-vector networks. *Mach Learn*. 1995;20:273–297.
- [10] Donelli M, Viani F, Rocca P, Massa A. An innovative multiresolution approach for DoA estimation based on a support vector classification. *IEEE Trans Antennas Propag*. 2009;57:2279–2292.

8. Instantaneous Brain Stroke Classification and Localization from Real Scattering Data

This chapter is based on following published paper:

Marco Salucci, Angelo Gelmini, Jan Vrba, Ilja Merunka, Giacomo Oliveri, Paolo Rocca:

“Instantaneous brain stroke classification and localization from real scattering data”.

**Microwave and Optical Technology Letters. 2019; 61: 805–808,
(Q4, IF = 0,96, 2 citations w/o selfcitations)**

Doi: <https://doi.org/10.1002/mop.31639>

Instantaneous Brain Stroke Classification and Localization from Real Scattering Data

Abstract

This work presents a 2-step Learning-by-Examples approach for the real-time classification of hemorrhagic/ ischemic brain strokes and their successive localization from microwave scattering data collected around the human head. An experimental assessment against laboratory-controlled data is performed to assess the potentialities of the proposed approach towards a reliable monitoring and instantaneous diagnosis clinic protocol.

Keywords

brain stroke microwave imaging, experimental data, inverse scattering, learning-by-examples (LBE), support vector machine (SVM)

8.1 Introduction

Brain stroke is worldwide a major cause of permanent disability and death [1–5]. Strokes can be classified into 2 categories: (1) ischemic (almost 85% of occurrences) when they are caused by the abrupt interruption of the blood flow within a region of the brain and (2) hemorrhagic when due to some blood leakage/bleeding phenomena. The latter ones are the most lethal pathology. Recognizing the type of stroke at hand and then inferring its position play a key role towards a suitable and effective clinical treatment just within few hours from the first symptoms [2]. Nowadays, such information mainly arise from 2D images generated through computed tomography (CT) and magnetic resonance imaging (MRI) that, despite their high reliability and robustness, need bulky and expensive instruments, and/or ionizing radiations, which are not suitable for a diffused (i.e. many users) and continuous/repeated monitoring.

Microwave imaging (MI) is another diagnosis technique with some desirable features such as (1) fast acquisition times (typically requiring few milliseconds [2]), (2) safety for the patient (thanks to the exploitation of the 0.5-2.0 GHz band), (3) high portability of the experimental setup, and (4) reduced costs. However, the challenge of developing effective inversion algorithms to quickly process measured data and to provide accurate guesses of the brain status has to be still solved before MI could emerge as an attractive alternative tool for real-time brain stroke diagnosis. Towards this end, several leading-edge research efforts consider the iterative solution of a forward scattering problem of a complex trial brain model to minimize the mismatch between measurement data and simulated ones. For instance, recent attempts employ massive parallel computing [1] to reduce the arising computational burden and to match clinical time constraints, while graphics processing units (GPUs) have been adopted in Ref. [2] to speed up the reconstruction process. However, they still require minutes for 2D images and hours for 3D views when using iterative gradient-based techniques.

Otherwise, Learning-by-Examples (LBE) strategies proved to be able to perform reliable and almost real-time data-inversions in many electromagnetic non-invasive diagnosis scenarios [6] since they do not require the solution of any forward problem during the on-line phase. In such a framework, a LBE-based MI inversion scheme has been proposed in Ref. [7] for the robust and quick detection of a brain stroke in a monitored head phantom. Still following that line-of-reasoning, but addressing the more challenging problem of identifying the stroke typology (i.e. ischemic or hemorrhagic) along with its position within the brain, this letter proposes a 2-step LBE-based classification approach. More specifically, the real-time inversion of experimental data is formulated first as a binary and then as a multi-class classification problem, both solved through a support vector machine (SVM) algorithm [6].

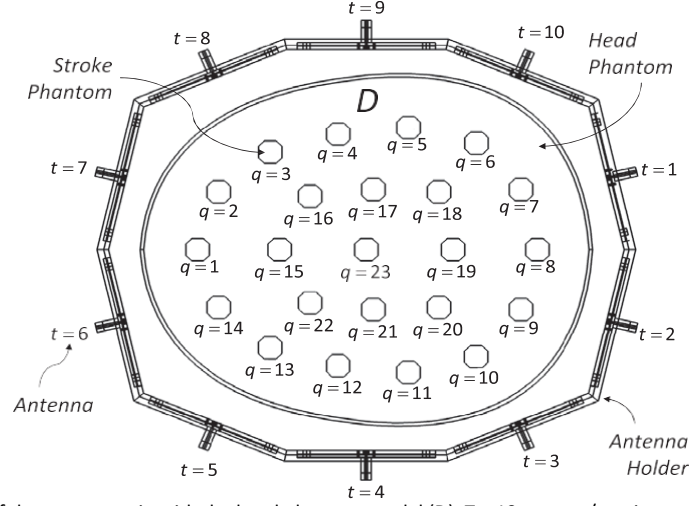


Figure 8.1, Geometry of the test scenario with the head phantom model (D), $T = 10$ sources/receivers, and the $Q = 23$ admissible brains stroke positions.

8.2 Brain stroke classification and normalization method

Let us model the human head as a domain D successively probed by an array of T antennas acting in transceiver mode and placed outside D as shown in Figure 8.1. For each t -th illumination, the complex scattering coefficients $S_{it}, i = 1, \dots, T$, are measured, S_{it} being the i -th transmission ($i \neq t$) or reflection ($i = t$) coefficient, respectively. Due to reciprocity, the set of independent collected data is composed by the following $(T + 1) \times T$ real-valued measured features [7].

$$\underline{\xi} = \{ [\Re(S_{ij}), \Im(S_{ij})]; i, j = 1, \dots, T; i \leq j \} \quad (1)$$

where the symbol $\Re(\cdot)$ [$\Im(\cdot)$] denotes the real (imaginary) part. Since $\varepsilon_r^h > \varepsilon_r^s$ and $\sigma^h > \sigma^s$ [1], $(\varepsilon_r^k, \sigma^k)$ being the relative permittivity and conductivity of an ischemic ($k = s$) or hemorrhagic ($k = h$) stroke (Figure 8.1) within the head phantom, and the measured data (ie, $\underline{\xi}$) depend on the electromagnetic properties of D through the scattering equations [2], the problem of determining the stroke type can be profitably formulated as a binary classification problem. By collecting a set of N input/output pairs during an off-line training phase, $(\underline{\xi}_n, \beta_n), n = 1, \dots, N, \beta_n$ being the (known) label for the n th sample (i.e. $\beta_n = -1 / +1 \rightarrow$ presence of an ischemic / hemorrhagic stroke), the following SVM decision function is built to predict the presence of an ischemic/hemorrhagic stroke from a previously unseen features set $\underline{\xi}$

$$\tilde{\beta}(\underline{\xi}) = \text{sgn} \left\{ \sum_{n=1}^N \alpha_n \beta_n K(\underline{\xi}, \underline{\xi}_n) + \eta \right\} \quad (2)$$

where α_n is the n th Lagrange multiplier, η is a bias term, and

$$K(\underline{\xi}, \underline{\xi}_n) = e^{-\gamma \left\| \underline{\xi} - \underline{\xi}_n \right\|^2} \quad (3)$$

is a radial basis function kernel controlled by the width parameter γ and used to properly model the non-linear relationship between $\underline{\xi}$ and $\beta(\underline{\xi})$ [6].

Once the brain stroke has been classified as ischemic/ hemorrhagic, the same data coded into the feature set $\underline{\xi}$ are processed by means of a multi-class SVM to find the most probable position

of the stroke area among a predefined set of Q candidate locations (Figure 8.1). More specifically, the one-against-one method is adopted [8] by generating $Q \times (Q - 1)/2$ binary classifiers, each trained with scattering data from only 2 classes (ie, 2 stroke positions within the head area D —Figure 8.1). For any couple (a, b) of classes, the binary decision function, $\tilde{\beta}^{ab}(\underline{\xi})$, is built during the off-line phase from N^{ab} training samples.

$$\begin{aligned} \tilde{\beta}^{ab}(\underline{\xi}) &= \text{sgn} \left\{ \sum_{n=1}^{N^{ab}} \alpha_n^{ab} \beta_n^{ab} K^{ab}(\underline{\xi}, \underline{\xi}_n) + \eta^{ab} \right\}; a, b \\ &= \{1, \dots, Q\}; a \neq b. \end{aligned} \quad (4)$$

Finally, the “Max Wins” voting Scheme [8] is applied to choose the class (i.e. the position within D) associated to the measured feature set $\underline{\xi}$ as that with the maximum number of occurrences among all trained binary classifiers.

8.3 Experimental assessment

The experimental validation has been carried out by processing the scattering data acquired with a microwave imaging system (Figure 8.2) composed by: (a) an antenna array of $T = 10$ coaxial-fed slot bow-tie antennas working at $f = 1.0$ GHz [9] and mounted on a decagonal prism container (Figure 8.1); (b) a microwave switching matrix R&S ZN-Z84; (c) a vector network analyser R&S ZNB8; (d) a head phantom within the volume D of dielectric properties equal to the average dielectric parameters of a human head (i.e. $\epsilon_r = 39.8$, $\sigma = 0.94$ S/m); (e) a stroke phantom container of diameter $d = 40$ [mm] filled with a liquid solution modeling either an hemorrhagic ($\epsilon_r^h = 51.4$, $\sigma^h = 1.22$ S/m) or an ischemic ($\epsilon_r^s = 35.6$, $\sigma^s = 0.85$ S/m) brain stroke. In order to evaluate the reliability of the 2 classification steps, the index of classification accuracy Γ , which is a function of the size N of the training set and is given by

$$\Gamma(N) = \frac{M'(N)}{M} \quad (5)$$

where M is the total number of test samples ($M = 230$), while $M'(N) \leq M$ is the number of correctly labelled test samples, has been computed. Concerning the first step (“*Brain Stroke Classification*”) of the proposed LBE-based approach, both training and test sets have been generated by considering an equal number of samples belonging to the 2 stroke classes and varying the stroke phantom position within the set of $Q = 23$ possible locations within the support of the head phantom, D (Figure 8.1). Figure 8.3 summarizes the assessment results in terms of classification accuracy Γ vs the dimension of the training set, N . As it can be observed, the stroke classification significantly and rapidly improves as N increases passing from an already high performance index when $N = 50$ [$\Gamma(50) = 86.5\%$ - Figure 8.3] up to a fully reliable classification ($\Gamma = 100\%$) when $N \geq 100$ (Figure 8.3).

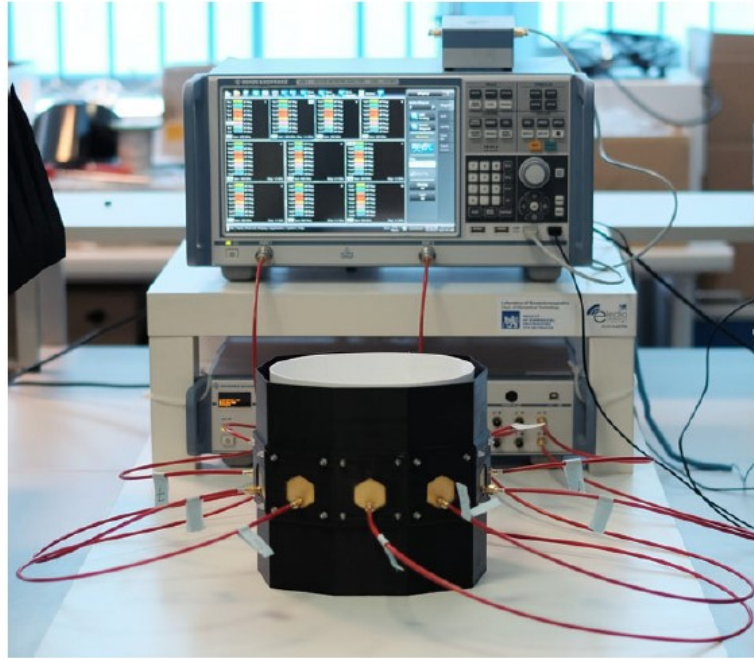


Figure 8.2, Experimental MI system for real-time brain stroke imaging.

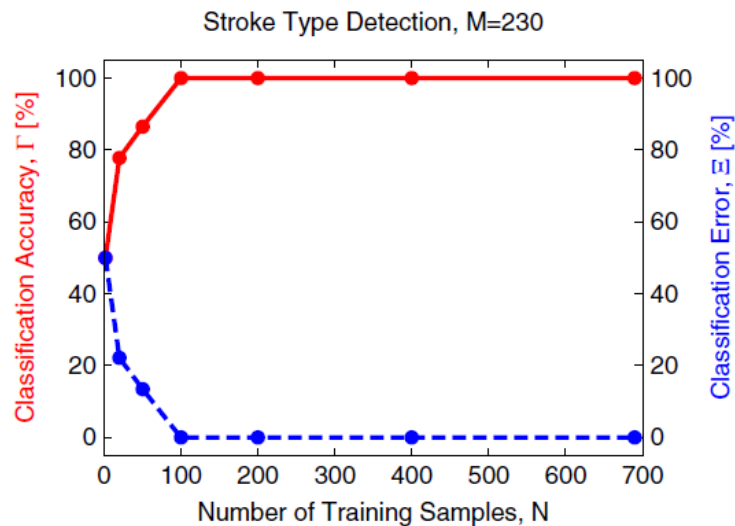


Figure 8.3, Experimental Assessment (Brain Stroke Classification, M = 230) – classification accuracy index, Γ , vs training size, N.

Moving to the retrieval of the stroke position, the multi-class SVM has been trained with $N_q = N/Q$ training samples for each q -th position ($q = 1, \dots, Q$ - Figure 8.1). Despite the more complex problem at hand, due to the presence of Q classes rather than 2 as in the “Brain Stroke Classification” (Step 1), the *LBE-MI* still performs very well (Figure 8.4). Indeed, just growing the training set size from $N = 46$ to $N = 92$ allows one to enhance the correct localization from $\Gamma(46) = 0\%$ up to $\Gamma(92) = 75.2\%$, while $N = 230$ (i.e. $N_q = 10$ training samples for each q -th ($q = 1, \dots, Q$) stroke position) are necessary to avoid wrong predictions (Figure 8.4). Of course, besides the classification accuracy, a key indicator for the proposed diagnosis technique is the computational cost (i.e. CPU time). It turns out that both binary and multi-class SVMs required $<10^{-2}$ sec to make predictions during the *on-line* test phase.

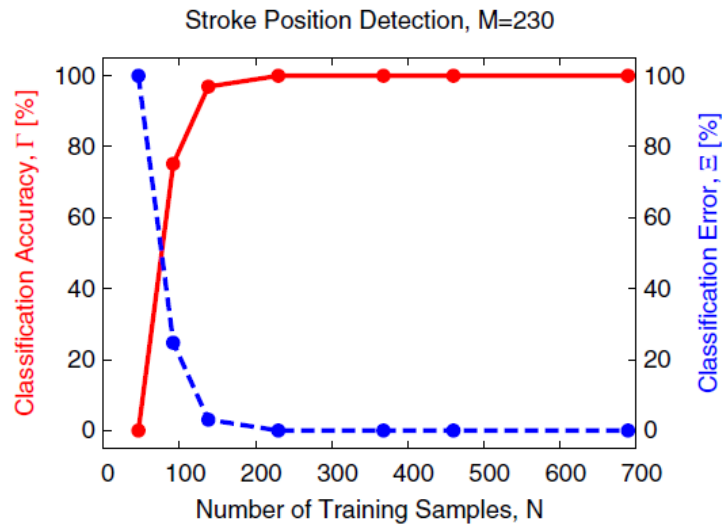


Figure 8.4, Experimental Assessment (Brain Stroke Localization, $M = 230$) – classification accuracy index, Γ , vs training size, N .

8.4 Conclusion

The discrimination between hemorrhagic and ischemic brain strokes as well as their localization have been addressed through a computationally efficient *LBE-MI* strategy. The proposed approach, which considers a cascade of a binary and a multiclass classification, has been successfully validated against real laboratory-controlled scattering data showing a remarkable prediction accuracy along with a very high computational efficiency. These features being of fundamental importance for a rapid intervention (eg, by restoring the damaged tissues through revascularization in case of ischemic strokes), the exploitation of such a *LBE-MI* strategy seems to be viable as an alternative and useful tool for the clinic diagnosis of the brain stroke.

Acknowledgments

This work has been supported by the research program of the Czech Science Foundation, Project no. 17-00477Y. Moreover, it has been partially supported by the Italian Ministry of Foreign Affairs and International Cooperation, Directorate General for Cultural and Economic Promotion and Innovation within the SNATCH Project (2017-2019) and it benefited from the networking activities carried out within the Càtedra de Excelencia UC3M-Santander funded by the Universidad Carlos III de Madrid (Spain) (Prof. A. Massa).

References

- [1] Tournier PH, Bonazzoli M, Dolean V, et al. Numerical modeling and high-speed parallel computing: new perspectives on tomographic microwave imaging for brain stroke detection and monitoring. *IEEE Antennas Propag Mag.* 2017;59: 98-110.
- [2] Hopfer M, Planas R, Hamidipour A, Henriksson T, Semenov S. Electromagnetic tomography for detection, differentiation, and monitoring of brain stroke. *IEEE Antennas Propag Mag.* 2017;59: 86-97.
- [3] Zamani A, Abbosh AM, Mobashsher AT. Frequency-based multistatic microwave imaging algorithm with application to brain injury detection. *IEEE Trans Microwave Theory Technol.* 2016;64: 653-662.
- [4] Persson M, Fhager A, Trefna HD, et al. Microwave-based stroke diagnosis making global pre-hospital thrombolytic treatment possible. *IEEE Trans Biomed Eng.* 2014;61:2806-2817.

- [5] Mohammed BJ, Bertling K, Abbosh AM, Rakic AD. Microwave head imaging system using analogue fibre-optic link for improved detection and localisation. *Electron Lett.* 2016;52:1366-1367.
- [6] Massa A, Oliveri G, Salucci M, Anselmi N, Rocca P. Learning-byexamples techniques as applied to electromagnetics. *J Electromagn Waves Appl.* 2018;32:516-541.
- [7] Salucci M, Vrba J, Merunka I, Massa A. Real-time brain stroke detection through a learning-by-examples technique - an experimental assessment. *Microw Opt Technol Lett.* 2017;59:2796-2799.
- [8] Mathur A, Foody GM. Multiclass and binary SVM classification: implications for training and classification users. *IEEE Geosci Remote Sens Lett.* 2008;5:241-245.
- [9] Merunka I, Vrba J, Fiser O, Vrba D. Comparison of Bow-Tie Slot and Rectangular Waveguide-Based Antennas for Microwave Medical Imaging. 12th European Conference on Antennas and Propagation; April 2018; London, UK.

9. Microwave Tomography System for Methodical Testing of Human Brain Stroke Detection Approaches

This chapter is based on following published paper:

Ilja Merunka¹, Andrea Massa², David Vrba³, Ondrej Fiser³, Marco Salucci² and Jan Vrba³:

“Microwave Tomography System for Methodical Testing of Human Brain Stroke Detection Approaches”,

International Journal of Antennas and Propagation Volume 2019, Article ID 4074862, 9 pages,
(Q3, IF = 1,21, 4 citations w/o selfcitations)

Doi: <https://doi.org/10.1155/2019/4074862>

Microwave Tomography System for Methodical Testing of Human Brain Stroke Detection Approaches

In this work, a prototype of a laboratory microwave imaging system suitable to methodically test the ability to image, detect, and classify human brain strokes using microwave technology is presented. It consists of an antenna array holder equipped with ten newly developed slot bowtie antennas, a 2.5 D reconfigurable and replaceable human head phantom, stroke phantoms, and related measuring technology and software. This prototype was designed to allow measurement of a complete S-matrix of the antenna array. The reconfigurable and replaceable phantom has currently 23 different predefined positions for stroke phantom placement. This setting allows repeated measurements for the stroke phantoms of different types, sizes/shapes, and at different positions. It is therefore suitable for large-scale measurements with high variability of measured data for stroke detection and classification based on machine learning methods. In order to verify the functionality of the measuring system, S-parameters were measured for a hemorrhagic phantom sequentially placed on 23 different positions and distributions of dielectric parameters were reconstructed using the Gauss-Newton iterative reconstruction algorithm. The results correlate well with the actual position of the stroke phantom and its type.

9.1 Introduction

Microwave tomography (MWT) is an emerging imaging technique for retrieving the spatial distribution of dielectric parameters of biological tissues [1]. In microwave imaging, the imaged area is typically exposed to electromagnetic (EM) waves radiated by antenna(s) positioned around the imaged area. The spatial distribution of the dielectric parameters in the imaged area influences the way of propagation of these waves, and the resulting EM field is subsequently measured by the same antennas. The measured data is used to estimate the distribution of dielectric properties within the imaged area. While the use of nonionizing radiation in MWT systems is a good argument when looking for benefits over a computed tomography and mammography (nonionizing radiation would allow frequent screenings), portability and cost effectiveness are good points when comparing MWT with magnetic resonance imaging [2].

Although one of the first reference of microwave hemorrhagic stroke detector can be found in the US patent by inventors Haddad and Trebes [3], there are nowadays several research groups working towards early stroke detection and differentiation systems. Just to name few leaders of the groups active in this field—Mikael Persson from Medfield Diagnostics AB, Sweden [4], Serguei Semenov from EMTensor GmbH, Austria [5], Amin Abbosch from The University of Queensland, Australia [6], and Lorenzo Crocco from the National Research Council of Italy, Italy [7–9]. Thorougher review can be found in [10].

In general, two different approaches for detection and classification of strokes can be found in literature: methods based on visualization (image reconstruction) of dielectric parameters distribution in the region of interests [6, 11] and methods based on machine learning algorithms [4, 12, 13].

Most of the published systems (both hardware and reconstruction/classification algorithms) have not been systematically tested. Typically, one or two stroke phantom positions are selected, and the results obtained are evaluated and presented.

In this paper, we designed and tested a laboratory microwave imaging system suitable for measuring head and stroke phantoms of various types, shapes, and sizes. The stroke phantoms could be placed at any of 23 predefined positions covering almost all the volume of the head

phantom. Such a system is especially suited for testing methods for stroke detection and classification based on machine learning algorithms, but it can be used for testing image reconstruction methods as well. Additionally, the proposed system allows testing of the two approaches for phantoms of different complexities and matching liquids of various dielectric properties. The system was tested using a simple 2.5 D reconfigurable head phantom with hemorrhagic stroke phantom, which was sequentially placed at some of the predefined positions. The system, phantoms, and measurements are described in Section 2. Section 3 includes an analysis of the measured data as a function of stroke phantom position. Finally, a deterministic iterative algorithm for the reconstruction of the dielectric properties distribution was applied in Section 4 to the measured data in order to verify functionality of the presented system.

9.2 Microwave Imaging System Description

9.2.1 Phantoms of Head and Brain Strokes, Antenna Array

The shape of the head phantom was designed with respect to the main objective of the article, namely, to systematically test the use of microwave imaging for the purpose of detection and classification of brain strokes occurring anywhere in the volume of human brain. For this, it is necessary to be able to place a stroke phantom on a predefined position in the entire head phantom. Towards this end, a liquid head phantom has been chosen to fill an elliptical container with a human head-shaped cross section in a transverse plane. The head phantom vessel is placed into the antenna element holder. The space between the vessel and the holder is filled with a matching liquid, see Figure 9.1. Both the antenna holder and the head phantom vessel have a height of 200mm (including a base of 4mm) and a wall thickness of 2mm. The numerical model of the proposed system and its physical form are shown in Figure 9.2. 23 octagonal pins are designed at the bottom of this container and are used to define the positions of phantoms of strokes. These latter are made by hollow cylinders filled by liquids of desired dielectric parameters, having an octagonal opening in their bottom. This ensures accurate and repeatable placement of phantoms of strokes in the head phantom. The containers for stroke phantoms have an internal diameter of 40mm, a height of 196mm, and a wall thickness of 1mm. All the parts were made by 3D printing using Prusa i3 MK2 (Prusa Research, Czech Republic) and PETG material.

9.2.2 Antenna Elements

Ten identical slot bowtie antennas (antenna design is described in [14]) were placed on the walls of the antenna array holder. The antennas were made of two layers of 1.5mm RF substrates Rogers R04003C with the dimensions of $59 \times 59 \text{ mm}^2$ and realized by Pragoboard s.r.o., Prague, Czech Republic. The main advantages of this antenna element design are suppressed radiation outside the imaging area, symmetry of radiated field, mechanical stiffness, and easy, inexpensive, and repeatable production. The front side of the realized antenna and the modules of measured reflection coefficients of all 10 antenna elements laid on the surface of a liquid head phantom are illustrated in Figure 9.3. The reflection coefficients of all ten antenna elements show virtually identical values and a low amplitude (less than -10 dB) in the frequency range from nearly 0.9 to 1.3 MHz. The system introduced in this work can therefore be used at any frequency in this frequency band. The frequency band was chosen in view of the fact that it fits into frequency bands already considered the most suitable for this application [7] considering attenuation of EM waves inside the human head and resolution of the imaging method. Although the authors believe that the higher number of antennas would lead to better

results, the maximal number of antennas is determined by the actual dimensions of the container and the used antenna elements.

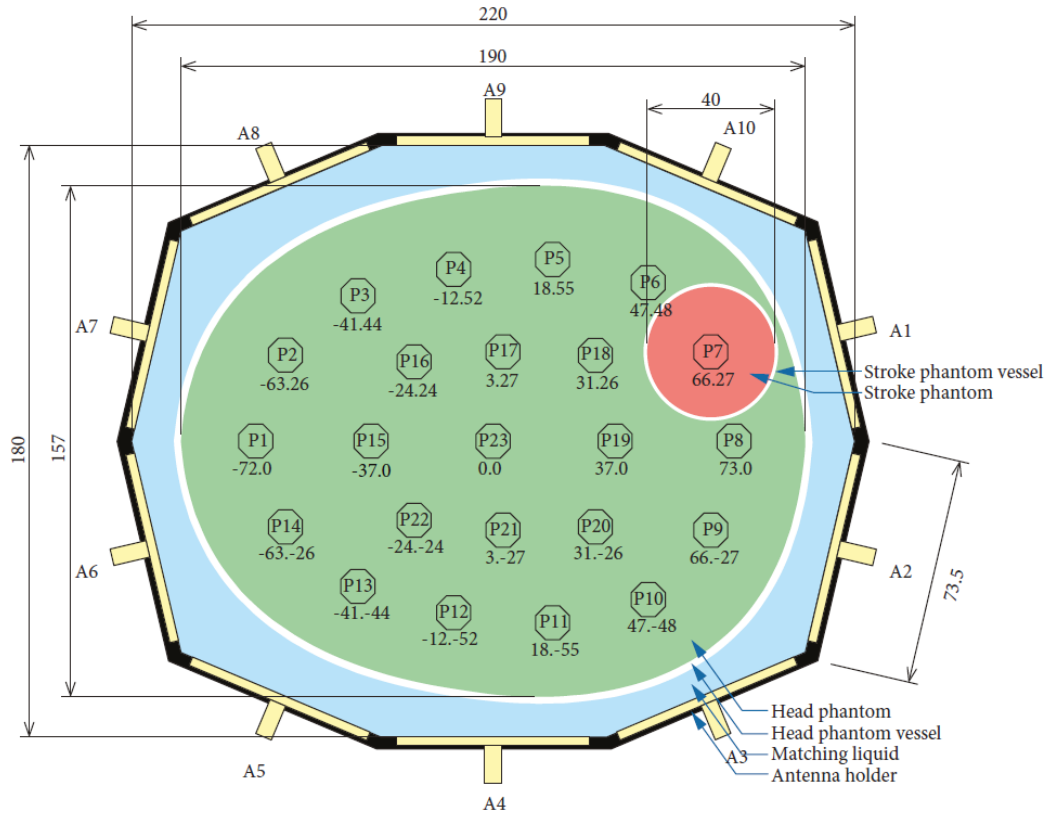


Figure 9.1, Bottom view of measuring container with marked positions of the stroke phantoms. Black: walls of the antenna holder, yellow: antennas with ports, blue: matching liquid, white: head phantom vessel, green: liquid phantom of human head, and red: liquid phantom of stroke at position P7 (all dimensions are in mm).

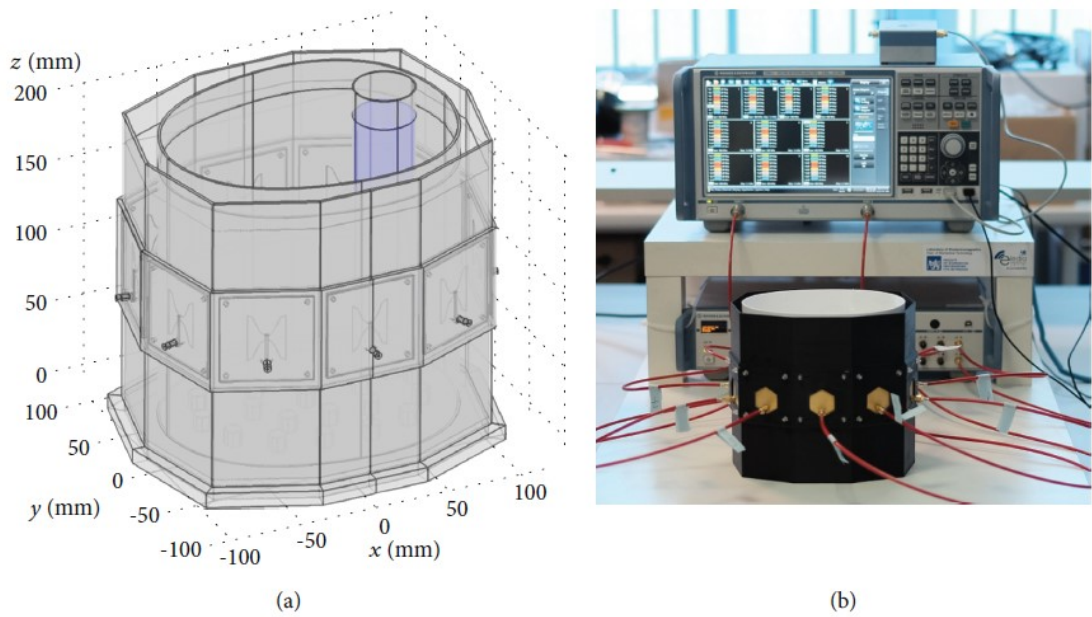


Figure 9.2, 3D model of measuring container with antennas and cylindrical phantom of stroke marked blue (a) and the photograph of the measuring setup (b).

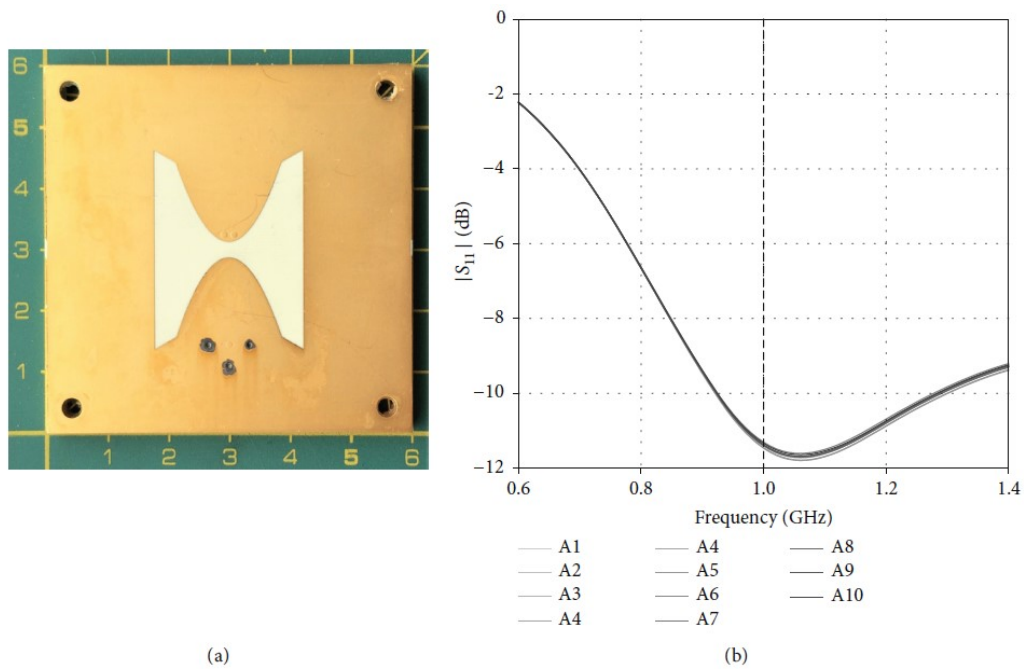


Figure 9.3, Photograph of the antenna element from the side facing to the phantom (a) (dimensions in cm) and measured magnitude of S_{11} for all antennas in frequency range 0.6 - 1.4 GHz heading to the liquid homogeneous phantom of human head (b). Central operating frequency is marked by a dashed line.

9.2.3 Measurement Setup and Settings.

The measuring instruments used in the presented MWI system are the microwave switching matrix ZN-Z84-B42 (Rohde & Schwarz, Germany) and the vector network analyzer (VNA) ZNB4-B32 (Rohde & Schwarz, Germany). The antennas were connected to the switching matrix test ports using semirigid coaxial cables (Rohde & Schwarz, Czech Republic). Although the isolation between all tested matrix ports should be greater than 90 dB, 10 out of 24 ports of the switching matrix test ports involved in the measurement were selected for the highest possible isolation between channels. The fact that 90 dB isolation should be sufficient is supported by another group that used an 80 dB [4] custom-made switching matrix. All high frequency connections were tightened by a torque wrench 0.9 Nm. Setting and triggering of measurements together with reading out of the measured data were done with MATLAB scripts written in-house (MathWorks, MA, USA). The photograph of the MWI system is shown in Figure 9.2. The following parameters of the measurement instruments were used: operating frequency 1GHz, intermediate frequency bandwidth 30 Hz, and output power of the VNA 13 dBm. The working frequency 1GHz was selected with respect to penetration depth, spatial resolution, and last but not least the fact that it fits into the frequency interval preferred for the same application in [7].

9.2.4 Calibration.

A full-port calibration was performed just before the measurement using the automatic calibration unit ZN-Z153 (Rohde & Schwarz, Germany).

Throughout the calibration period, the antenna elements were disconnected from the coaxial cables leading into the switching matrix. To these open ends of the coaxial cables, the calibration unit was three times reconnected (due to the lower number of ports of the calibration unit than the number of used antenna elements/system channels) following the calibration instructions displayed on the VNA. In this way, the switching matrix was included in the full-port VNA calibration.

The VNA, switching matrix, and automatic calibration unit were turned on 90 minutes before the calibration onset. Calibration data was saved and reloaded before each measurement.

9.2.5 Liquid Phantom Composition and Dielectric Properties.

Two liquid phantoms substituting healthy head and brain hemorrhagic stroke tissue were prepared. The dielectric properties of the head phantom are equal to average dielectric parameters of a human head ($\epsilon_{r,HH} = 39.8$, $\sigma_{HH} = 0.94\text{S/m}$) [15]. The dielectric properties of the hemorrhagic stroke phantom are chosen based on the knowledge of the dielectric properties of blood [16], where the contrast to brain tissues is about 50 - 60%. A conservative change at the level of 30% is chosen here ($\epsilon_{r,HR} = 51.4$, $\sigma_{HR} = 1.22\text{ S/m}$) as in [5]. Dielectric properties of the phantoms were measured using DAK (Schmid & Partner Engineering AG, Switzerland) just before the measurement in the MWI system prototype. Compositions in weight percent and comparison of target and measured dielectric properties of the phantoms are listed in Table 9.1. In this table, the HEAD marks the column devoted to the phantom of the head and the HEM marks the column devoted to the hemorrhagic stroke phantom. The dielectric parameters listed in rows following the compositions were measured at a frequency of 1GHz and 25 °C before the measurement in the MWI system. In order to eliminate the reflections from the interface matching liquid-head, the head phantom material was also used as the matching liquid between the antennas and the head vessel.

Table 9.1, Phantom Phantom composition in weight percent, target, and measured dielectric parameters at 1 GHz and 25°C, immediately before the measurement in the MWI system.

	HEAD	HEM
Isopropyl alcohol (wt%)	50.48	34.00
Deionized water (wt%)	48.35	64.67
NaCl (wt%)	1.16	1.33
Target ϵ_r (-)	39.60	51.48
Measured ϵ_r (-)	39.80	51.37
U ($k = 2$) (%)	1.7	2.1
Target σ (S/m)	0.94	1.220
Measured σ (S/m)	0.94	1.224
U ($k = 2$) (%)	2.7	2.7

U: expanded uncertainty of type B, HEAD: head phantom, HEM: hemorrhagic phantom.

9.2.6 Measuring Procedure.

The antenna array holder and the head phantom vessel were firstly filled with homogeneous head phantom liquid. Special attention was paid to elimination of bubbles which appeared on the surface of antennas during the filling procedure of the container. Finally, the container was enclosed by microwave pyramid absorbers. The measurement procedure is composed from two main steps: (1) measurement of the MWI system filled with the head phantom only and (2) measurement with the head phantom including the hemorrhagic stroke phantom. The phantom of stroke was subsequently positioned and measured in all 23 positions (Figure 9.1). Whole S-matrix was measured 10 times in series to cover fluctuations that could appear during the measurement for every position of the stroke. One measurement of the full S-matrix took about 12 s.

9.3 Measured Data

The response of the system to a presence of the phantom of hemorrhagic stroke at all 23 positions is visualized in Figure 9.4. It is calculated as the relative difference in the modules

(equation (1)) and as the absolute difference in the arguments (equation (2)) of the S-parameters measured with (S_{mn}^{STROKE}) and without (S_{mn}^{HOMO}) the stroke phantom, respectively.

$$\Delta|S_{mn}| = \frac{||S_{mn}^{STROKE}| - |S_{mn}^{HOMO}||}{|S_{mn}^{HOMO}|}, \quad (1)$$

$$\Delta\angle S_{mn} = |\angle S_{mn}^{STROKE} - \angle S_{mn}^{HOMO}|. \quad (2)$$

The most responding S-parameters to the stroke at the specific position can be deduced from those images. The characteristic patterns in both amplitude and phase images indicate the strongest responses in transmission coefficients.

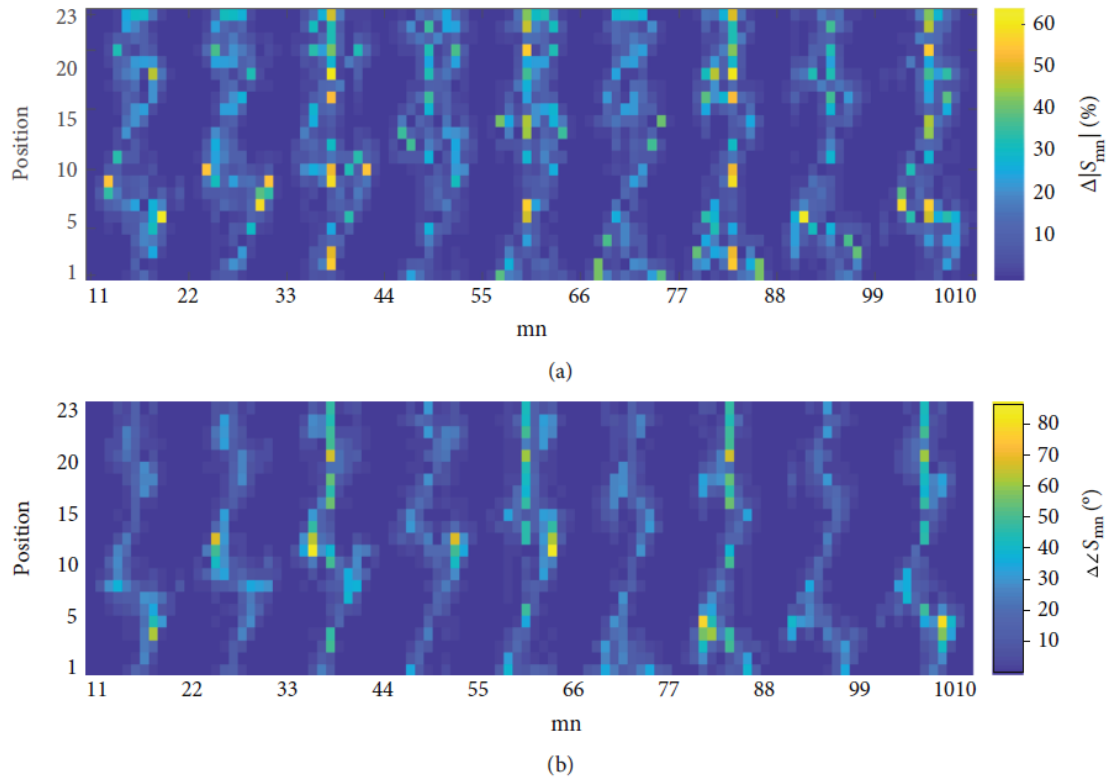


Figure 9.4, Response of the system ((a) relative change in the modulus of S-matrix and (b) change in the phase of S-matrix in degrees) to a presence of the hemorrhagic stroke phantom at 23 different positions (y axes) in the phantom of human head.

9.4 Application of Image Reconstruction Algorithm to Measured Data

A reconstruction algorithm based on Gauss-Newton algorithm with Tikhonov regularization [17] was used to reconstruct the dielectric image in the central plane of the antennas from the measured S parameters. This algorithm is based on deterministic optimization procedure, assuming linear behavior of outcome in every iteration when only a small change in dielectric properties is introduced. In order to reduce the building time of the Jacobian matrix, the so called adjoint method was used [18]. The value of the Tikhonov parameter was determined using the procedure described in [17].

9.5 Image Reconstruction Procedure

The image reconstruction procedure includes solution of forward problem (computation of electromagnetic field distribution and S-matrix), extraction of E-fields and S-matrix, computation of Jacobian, and computation of step in dielectric properties of the material domains. To model the propagation of E-field in the forward step, the 3D numerical version of the real measuring

system was modeled in COMSOL Multiphysics (Figure 9.2 (a)). Models of the real antennas together with SMA ports were used in the numerical model. Special attention was paid to correctly discretize all the model components. Finally, EM field was computed using the finite element method in 3D. All three components of E-field were extracted and used in the inverse step. In order to precisely represent the real-world scenario, any special assumption either simplification in the computational procedure of EM field was not made. Therefore, the framework presented in this paper can be easily adapted to the other realistic scenario by simply replacing the numerical model. Computation of the forward problem is the most computationally extensive procedure and takes about 150 minutes for all 10 antenna ports on the current PC (i7-6700 - 3.4 GHz, 64GB DDR4 RAM - 2133 MHz). The reconstruction algorithm was implemented in MATLAB.

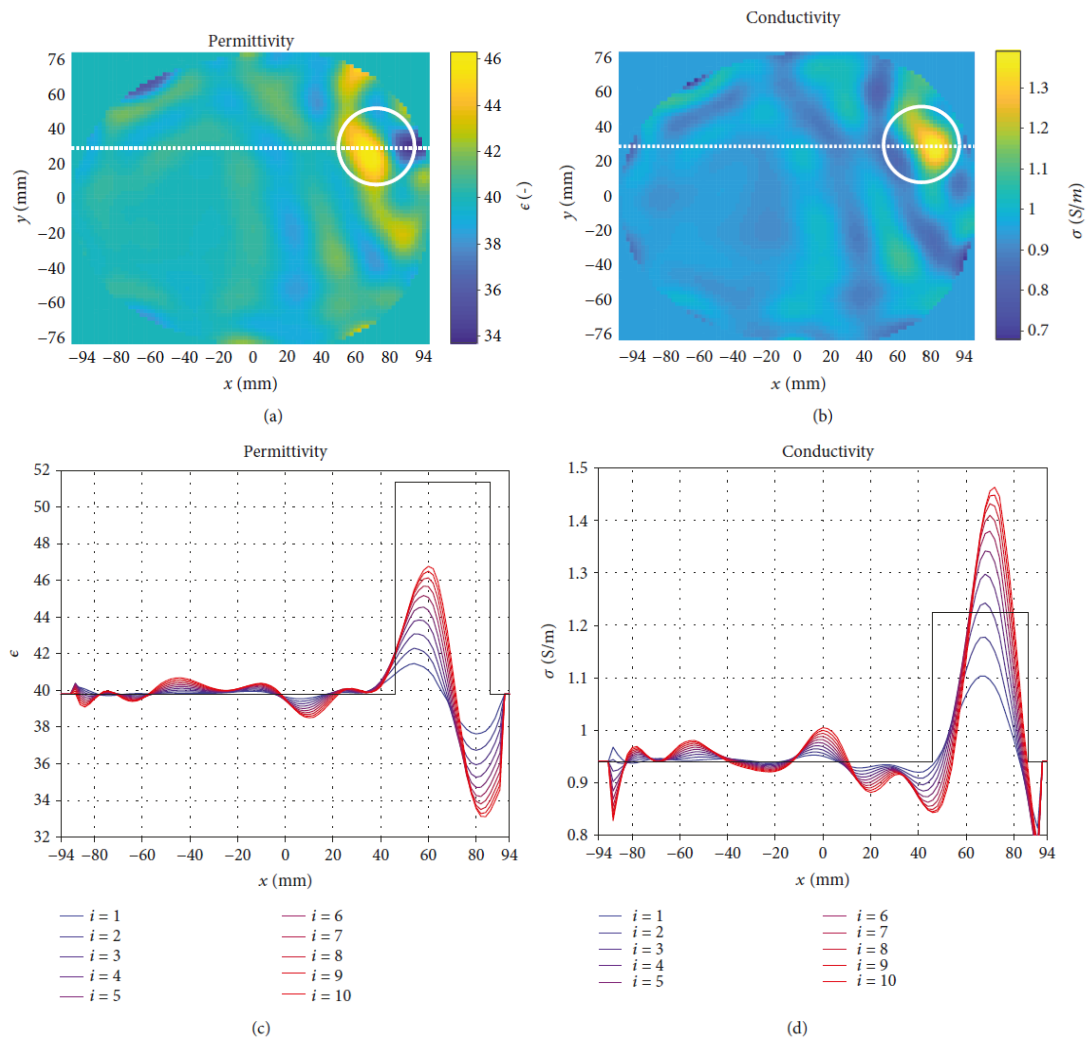


Figure 9.5, Results (a, b) of iterative reconstruction procedure for hemorrhagic stroke phantom at position P7 (marked by white circle) and evolution (c, d) of relative permittivity and conductivity over the iterations ($i = 1$ for the first iteration, $i = 10$ for the tenth iteration) on the line going through the center of the stroke phantom (marked by dashed white lines). Actual values of both relative permittivity and conductivity are marked by solid black lines in graphs (c) and (d).

In an attempt to achieve the actual values of complex permittivity in the region of interest, 10 iterations of the reconstruction algorithm were performed. Since the image reconstruction takes more than 25 hours for 10 iterations, the maximal number of iterations allowed was set to 10. Better results could be possibly achieved with higher number of iterations. However, as it can be seen from Figure 9.5 (c, d) there is only a small change in the dielectric parameters over

the last few iterations. Results of the reconstruction in a plane going through the center of the antennas for hemorrhagic stroke at position P7 are shown in Figure 9.5.

Even though values of relative permittivity and conductivity in the reconstructed images did not reach the actual values and shape of the stroke, the biggest change in those quantities can be observed in the area of the stroke phantom (white circle). Nine different unique positions of the stroke phantom inside the head phantom were selected, and the measured data were processed with the image reconstruction algorithm. In order to show the results of the reconstruction for all the positions of the stroke in one image, 350 values of relative permittivity and conductivity differing the most from the background matching liquid were detected in all 9 images and its positions plotted together for every stroke phantom position, see Figure 9.6 (a) and (b). In this figure, the threshold used to allow the binarization is based on the assumption that the size of the stroke phantom is known. And so, the size of the area covered by the dots of the specific color in Figure 9.6 is equaled to the size of the area of the cross-section of the stroke phantom. Positions of the stroke phantom can be better recognized from images depicting conductivity. Since the quantitative information is lost in Figure 9.6, the maximal values of dielectric parameters are listed in Table 9.2.

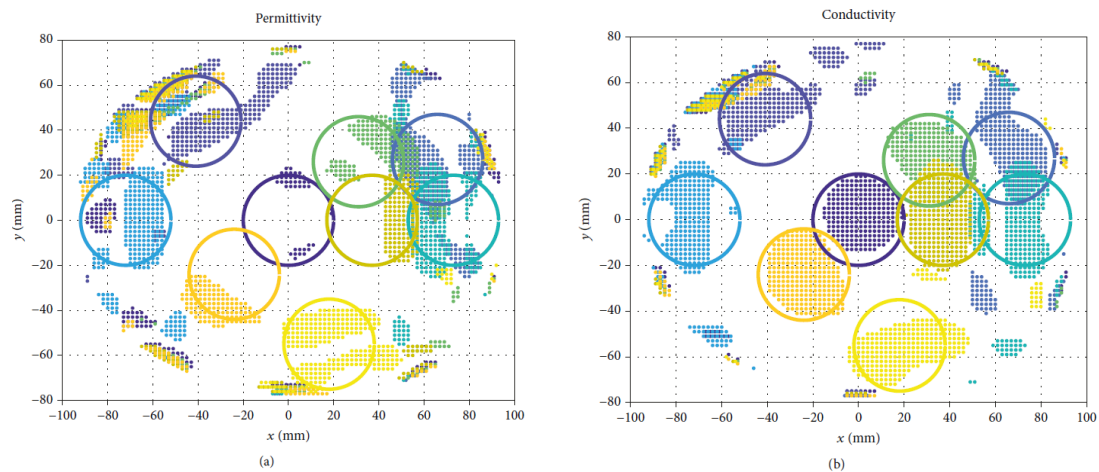


Figure 9.6, Detection of position of the strokes from reconstructed images. Circles mark the actual position of the stroke; dots of adequate color show the detected positions.

Table 9.2, Maximal values of dielectric parameters for the selected positions of the stroke phantom after the reconstruction.

Position	P1	P3	P7	P8	P11	P18	P19	P22	P23
max ϵ_r (-)	48.13	51.34	46.30	47.60	44.87	44.71	44.71	45.23	44.48
max σ (S/m)	1.42	1.32	1.39	1.38	1.30	1.23	1.24	1.22	1.24

9.6 Discussion

The MWI systems are very sensitive to the quality of conducted microwave measurement. There are many cofounders, including temperature drift of measuring devices, changes in complex permittivity of phantoms due to the changes in temperature, evaporation and possible leak of liquids during stroke phantom replacement procedure, appearance of bubbles in the liquid phantoms, and quality of multipoint calibration procedure, that the experimenter has to deal with during the measuring procedure. All those sources of noise negatively impact the quality of reconstructed images. Conservative estimates of the differences between the dielectric properties of brain tissues and areas affected by strokes were considered. It can be assumed that a higher contrast in the dielectric properties of the head phantom and stroke phantoms would yield in better reconstruction results.

The number of antennas/channels of the presented system was determined by the dimensions of the human head/head phantom and the antenna element. For the used antenna elements, only limited size reductions can be achieved. Metamaterial-based structures such as described in [19–21] could be suitable for systems with a higher number of the antenna elements.

The forward problem in every iteration is solved for every antenna element. This can be done in parallel and thus reduce the total computational time. Further reduction of the computational time could be achieved by using the Finite Differences in Time-Domain Method (FDTD) which can be accelerated using GPU. If a broadband formulation of FDTD is used, it is possible to obtain results for multiple frequencies in a single simulation without a significant computational time increase.

In this work, imaging results for only 9 stroke phantom positions are presented, although there are in total of 23 positions available. This step is only motivated by the clarity of the imaging results presented. The 9 positions considered were carefully selected based on the geometric symmetry of the head phantom and antenna array. In other words, the imaging results for each of the remaining 14 positions would not differ much from the results corresponding to one of the 9 positions.

9.7 Conclusion

The prototype of the MWT system allowing systematic evaluation of human brain stroke detection and classification approaches has been presented in this paper. In order to prove the capabilities of the presented system, hemorrhagic phantom of human brain stroke was prepared and the experimental measurements were conducted with this stroke sequentially placed at 23 different positions in the head phantom. Achieved results support the statements of another groups working in this field that the detection and differentiation of the strokes by means of microwave technique should be possible at least in the laboratory conditions. In our future work, we are going to improve our system in several ways to deal with some major known issues such as low sensitivity, spatial resolution, and sensitivity to noise. A 2.5 D anatomically realistic head phantom consisting of three solid layers with shape and dielectric properties corresponding to skin, skull, and cerebrospinal fluid is currently under development. We also plan to combine the reconstructed images with detection and classification by algorithms of machine learning.

References

- [1] A. Fhager, P. Hashemzadeh, and M. Persson, "Reconstruction quality and spectral content of an electromagnetic timedomain inversion algorithm," *IEEE Transactions on Biomedical Engineering*, vol. 53, no. 8, pp. 1594–1604, 2006.
- [2] P. M. Meaney, "Microwave imaging and emerging applications," *International Journal of Biomedical Imaging*, vol. 2012, Article ID 252093, 2 pages, 2012.
- [3] W. Haddad and J. Trebes, "Microwave hemorrhagic stroke detector," US Patent US20 030 018 244 A1, 2003, US Classification 600/371; International Classification A61B5/05; Cooperative Classification A61B5/4076, A61B5/0507, A61B5/05; European Classification A61B5/05M, A61B5/05, <https://www.google.ch/patents/US20030018244>.
- [4] M. Persson, A. Fhager, H. D. Trefna et al., "Microwave-based stroke diagnosis making global prehospital thrombolytic treatment possible," *IEEE Transactions on Biomedical Engineering*, vol. 61, no. 11, pp. 2806–2817, 2014.

- [5] M. Hopfer, R. Planas, A. Hamidipour, T. Henriksson, and S. Semenov, "Electromagnetic tomography for detection, differentiation, and monitoring of brain stroke: a virtual data and human head phantom study," *IEEE Antennas and Propagation Magazine*, vol. 59, no. 5, pp. 86–97, 2017.
- [6] D. Ireland, K. Bialkowski, and A. Abbosh, "Microwave imaging for brain stroke detection using Born iterative method," *IET Microwaves, Antennas & Propagation*, vol. 7, no. 11, pp. 909–915, 2013.
- [7] R. Scapatucci, L. Di Donato, I. Catapano, and L. Crocco, "A feasibility study on microwave imaging for brain stroke monitoring," *Progress In Electromagnetics Research B*, vol. 40, pp. 305–324, 2012.
- [8] R. Scapatucci, O. M. Bucci, I. Catapano, and L. Crocco, "Differential microwave imaging for brain stroke followup," *International Journal of Antennas and Propagation*, vol. 2014, Article ID 312528, 11 pages, 2014.
- [9] R. Scapatucci, J. Tobon, G. Bellizzi, F. Vipiana, and L. Crocco, "Design and numerical characterization of a lowcomplexity microwave device for brain stroke monitoring," *IEEE Transactions on Antennas and Propagation*, vol. 66, no. 12, pp. 7328–7338, 2018.
- [10] L. Crocco, I. Karanasiou, M. L. James, and R. C. Conceição, Eds., *Emerging Electromagnetic Technologies for Brain Diseases Diagnostics, Monitoring and Therapy*, Springer International Publishing, 2018, <https://www.springer.com/la/book/9783319750064>.
- [11] A. Abbosh, "Microwave systems for head imaging: challenges and recent developments," in *2013 IEEE MTT-S International Microwave Workshop Series on RF and Wireless Technologies for Biomedical and Healthcare Applications (IMWS-BIO)*, pp. 1–3, Singapore, December 2013.
- [12] M. Salucci, J. Vrba, I. Merunka, and A. Massa, "Real-time brain stroke detection through a learning-by-examples technique - an experimental assessment," *Microwave and Optical Technology Letters*, vol. 59, no. 11, pp. 2796–2799, 2017.
- [13] M. Salucci, A. Gelmini, J. Vrba, I. Merunka, G. Oliveri, and P. Rocca, "Instantaneous brain stroke classification and localization from real scattering data," *Microwave and Optical Technology Letters*, vol. 61, no. 3, pp. 805–808, 2019.
- [14] I. Merunka, J. Vrba, O. Fiser, and D. Vrba, "Comparison of bowtie slot and rectangular waveguide-based antennas for microwave medical imaging," in *12th European Conference on Antennas and Propagation (EuCAP 2018)*, pp. 1–5, London, UK, April 2018.
- [15] IEEE Std 1528-2013 (Revision of IEEE Std 1528-2003), *IEEE Recommended Practice for Determining the Peak Spatial-Average Specific Absorption Rate (SAR) in the Human Head from Wireless Communications Devices: Measurement Techniques*, IEEE, 2013, <https://search.library.wisc.edu/catalog/9912350582702121>.
- [16] P. A. Hasgall, F. Di Gennaro, C. Baumgartner et al., "IT'IS database for thermal and electromagnetic parameters of biological tissues," January 2015, <http://www.itis.ethz.ch/database>.
- [17] N. Joachimowicz, C. Pichot, and J. P. Hugonin, "Inverse scattering: an iterative numerical method for electromagnetic imaging," *IEEE Transactions on Antennas and Propagation*, vol. 39, no. 12, pp. 1742–1753, 1991.

- [18] Q. Fang, P. M. Meaney, S. D. Geimer, A. V. Streltsov, and K. D. Paulsen, "Microwave image reconstruction from 3-D fields coupled to 2-D parameter estimation," *IEEE Transactions on Medical Imaging*, vol. 23, no. 4, pp. 475–484, 2004.
- [19] M. Polívka and D. Vrba, "Shielded micro-coplanar CRLH TL zeroth-order resonator antenna: critical performance evaluation," *Radioengineering*, vol. 18, no. 1, pp. 1592–1595, 2009.
- [20] J. Vrba and D. Vrba, "A microwave metamaterial inspired sensor for non-invasive blood glucose monitoring," *Radioengineering*, vol. 24, no. 4, pp. 877–884, 2015.
- [21] D. Vrba, J. Vrba, D. B. Rodrigues, and P. Stauffer, "Numerical investigation of novel microwave applicators based on zeroorder mode resonance for hyperthermia treatment of cancer," *Journal of the Franklin Institute*, vol. 354, no. 18, pp. 8734–8746, 2017.

10. Thesis Conclusion

This dissertation thesis was focused mainly on contribution to new prospective technological trends of MWT in medical imaging and diagnostics, especially to its theory and near future clinical applications. I decided to concentrate mostly on the deterministic iterative approaches. These approaches seem to be the one of the most promising for medical application of MWT.

In this chapter I would like to summarize the main results described in my dissertation thesis, which I consider to be my own “dissertable” contributions to the here discussed topics. It consists of following main closely interconnected parts:

- Design of special antenna systems for microwave tomography (Chapter 3, 5 and 9)
- Complex permittivity measurement of human tissues (Chapter 6)
- Study of reconstruction algorithms for microwave tomography and its implementation (Chapter 2, 7 and 8)
- Development of a system for brain stroke detection and classification (Chapter 2, 4 and 9)
- Development of temperature dependent model of dielectric properties of an agar phantom for testing of a system combining MHTS and MWT (Chapter 5)

10.1 Summary

The work here described comes out from main research projects in which I was involved during my doctoral studies (see please at the end of this chapter).

In Chapter 1: “Microwave Imaging: State of the Art”, I described the state of the art in the area of medical applications of microwaves in medical diagnostics and specified main aims of this dissertation thesis.

Consequently, chapters 2 to 9 bring my original (i.e. dissertable) contributions to the discussed scientific topics.

Chapter 2: “Image Reconstruction Algorithm: Iterative Algorithm with Gauss Newton Optimization” describes the basics and implementation of the imaging algorithm implemented in the frame of this dissertation.

Chapter 3: “Antenna Elements for Microwave Tomography” consist of two main parts. In the first part four different antennas were compared with respect to its suitability for use in microwave tomography system (two microstrip patch antennas, wire monopole antenna and waveguide antenna). Aim of this work was to recommend an antenna element for the next generation of our microwave tomography system. Several criterions were defined here and they were evaluated for every tested antenna. While microwave patch antennas fulfil the best most of our criteria, waveguide antenna has the most suitable radiation pattern.

In the second part of this chapter the novel type of bowtie slot antenna (whose radiation is comparable to a waveguide antenna in terms of symmetry) was proposed and described. Furthermore, this antenna is equipped with a ground plane that limits the radiation outside the imaging area. We consider the proposed antenna as a suitable alternative to the waveguide antenna.

In the Chapter 4: “Laboratory Microwave Imaging System for Detection and Classification of Strokes”, there is a description of a prototype of microwave imaging system for brain stroke detection and differentiation, which was developed with my active participation at the Faculty

of Biomedical Engineering of the Czech Technical University in Prague. This prototype composes of measuring container with eight bowtie antennas, vector network analyser and PC with appropriate software. 3D printed measuring container was filled with liquid phantom of human head. Two different phantoms of brain stroke were prepared (haemorrhagic and necrotic) and moved over 25 different positions in measuring container and thereby covering almost all possible areas in the brain phantom. Gauss-newton iterative reconstruction algorithm incorporating computation of EM field in 3D numerical model in every iteration and adjoint method of computation of Jacobian was implemented and applied to measured S parameters. Approximate position of strokes of both types can be observed from reconstructed images of conductivity based on synthetic as well as measured data even after one iteration of the algorithm. Since EM field for empty measuring container can be computed in advance for the first iteration, those results can be obtained in couple of seconds. Furthermore, a tendency to rise or decrease in conductivity in the region of stroke can also be observed from these images, which is important information for differentiation of the strokes.

In the Chapter 5: “Temperature Dependent Complex Permittivity Model of Agar Phantom for Microwave Temperature Distribution Monitoring During Microwave Hyperthermia Treatment”, utilization potential of microwave tomography for temperature monitoring during microwave hyperthermia treatment was discussed. Although temperature in the region is consequently derived from relative change in measured complex permittivity in the heated region, proper temperature dependent model of complex permittivity of human tissues must be known. In order to allow testing of a prototypes, tissue simulating materials are used instead of real tissues and from that reason complex permittivity of agar phantom material was measured and a frequency and temperature dependent model of dielectric properties was created.

Chapter 6: “Dielectric Measurement of Biological Tissues: Challenges and Common Practices” is based on paper published in *Diagnostics* 2018, 8, 40. It is stated here, that EM medical technologies are expanding for both diagnostics and therapy. As these technologies are low-cost and minimally invasive, they have been the focus of significant research efforts in recent years. Such technologies are often based on the assumption that there is a contrast in the dielectric properties of different tissue types or that the properties of particular tissues fall within a defined range. Thus, accurate knowledge of the dielectric properties of biological tissues is fundamental to EM medical technologies. Over the past decades, numerous studies were conducted to expand the dielectric repository of biological tissues. However, dielectric data is not yet available for every tissue type and at every temperature and frequency. For this reason, dielectric measurements sometimes may be performed by researchers who are not specialists in the acquisition of tissue dielectric properties. To this end, this paper reviews the tissue dielectric measurement process performed with an open-ended coaxial probe. Given the high number of factors, including equipment- and tissue-related confounders, that can increase the measurement uncertainty or introduce errors into the tissue dielectric data, this work discusses each step of the coaxial probe measurement procedure, highlighting common practices, challenges, and techniques for controlling and compensating for confounders.

Chapter 7: “Real-time brain stroke detection through a learning-by-examples technique—An experimental assessment” is based on paper published in *Microwave and Optical Technology Letters*, 2017;59:2796–2799. The real-time detection of brain strokes is addressed within the Learning-by-Examples (LBE) framework. Starting from scattering measurements at microwave regime, a support vector machine (SVM) is exploited to build a robust decision function able to infer in real-time whether a stroke is present or not in the patient head. The proposed approach

is validated in a laboratory-controlled environment by considering experimental measurements for both training and testing SVM phases. The obtained results prove that a very high detection accuracy can be yielded even though using a limited amount of training data.

Chapter 8: “Instantaneous Brain Stroke Classification and Localization from Real Scattering Data” is based on paper published in *Microwave and Optical Technology Letters*, 2019;61, 805–808. This chapter presents a 2-step Learning-by-Examples approach for the real-time classification of hemorrhagic/ ischemic brain strokes and their successive localization from microwave scattering data collected around the human head. An experimental assessment against laboratory-controlled data was performed to assess the potentialities of the proposed approach towards a reliable monitoring and instantaneous diagnosis clinical protocol.

Chapter 9: “Microwave Tomography System for Methodical Testing of Human Brain Stroke Detection Approaches” is based on the paper published in *International Journal of Antennas and Propagation* Volume 2019, Article ID 4074862 (9 pages). In this chapter, a prototype of a laboratory microwave imaging system, suitable to methodically test the ability to image, detect, and classify human brain strokes by using microwave technology, is presented. It consists of an antenna array holder equipped with ten newly developed slot bowtie antennas, a 2.5 D reconfigurable and replaceable human head phantom, stroke phantoms, and related measuring technology and software. This prototype was designed to allow measurement of a complete S-matrix of the antenna array. The reconfigurable and replaceable phantom has currently 23 different predefined positions for stroke phantom placement. This setting allows repeated measurements for the stroke phantoms of different types, sizes/shapes, and at different positions. It is therefore suitable for large-scale measurements with high variability of measured data for stroke detection and classification based on machine learning methods. To verify the functionality of the measuring system, S-parameters were measured for a hemorrhagic phantom sequentially placed on 23 different positions and distributions of dielectric parameters were reconstructed using the Gauss-Newton iterative reconstruction algorithm. The results correlate well with the actual position of the stroke phantom and its type.

10.2 Conclusion

In my opinion my doctoral thesis fulfilled the main goals. Initially there was my own research inspired by the COST Action TD1301: “Development of a European-based Collaborative Network to Accelerate Technological and Clinical in the Area of Medical Microwave Imaging”. Major part of the research work within this dissertation thesis has been done in the frame of the research projects granted from the Czech Science Foundation, number 17-20498J: “Non-invasive temperature estimation inside of human body based on physical aspects of ultra-wideband microwave channel” and the German Science Foundation (DFG) in the project HE 6015/2-1. In part it was supported by CTU grant SGS17/182/OHK3/3T/13, too.

11. Publications of the author

11.1 Publications in journals with an impact factor

All authors contributed equally to the publications mentioned in this section.

11.1.1 Publications related to the thesis

[M1] Ilja Merunka, Andrea Massa, David Vrba, Ondrej Fiser, Marco Salucci and Jan Vrba, Microwave Tomography System for Methodical Testing of Human Brain Stroke Detection Approaches. International Journal of Antennas and Propagation. 2019, ISSN 1687-5869.

(Q4, IF = 1,207, 4 citations w/o selfcitations)

Doi: <https://doi.org/10.1155/2019/4074862>

[M2] Salucci M, Vrba J, Merunka I, Massa A. Real-time brain stroke detection through a learning-by-examples technique - An experimental assessment. Microwave and Optical Technology Letters. 2017, 59(11), 2796-2799. ISSN 0895-2477.

(Q4, IF = 0,948, 9 citations w/o selfcitations)

Doi: <https://doi.org/10.1002/mop.30821>

[M3] M. Salucci, A. Gelmini, J. Vrba, I. Merunka, G. Oliveri, P. Rocca, Instantaneous brain stroke classification and localization from real scattering data. Microwave and Optical Technology Letters. 2019, 61(3), 805-808. ISSN 0895-2477.

(Q4, IF = 0,957, 2 citations w/o selfcitations)

Doi: <https://doi.org/10.1002/mop.31639>

[M4] La Gioia, E. Porter, I. Merunka, A. Shahzad, S. Salahuddin, M. Jones, M. O'Halloran Open-Ended Coaxial Probe Technique for Dielectric Measurement of Biological Tissues: Challenges and Common Practices. Diagnostics. 2018, 8(2), 1-38. ISSN 2075-4418.

(2018: Q2, IF = 2,49, 2019: Q1, IF = 3,11, 24 citations w/o selfcitations)

Doi: <https://doi.org/10.3390/diagnostics8020040>

[M5] O. Fiser, I. Merunka, and J. Vrba, Waveguide Applicator System for Head and Neck Hyperthermia Treatment. Journal of Electrical Engineering & Technology. 2016, 11(6), 1744-1753. ISSN 1975-0102.

(2016: Q4, IF = 0.525, 2019: Q4, IF = 0,736)

Doi: <https://doi.org/10.5370/JEET.2016.11.6.1744>

[M6] O. Fiser, M. Helbig, J. Sachs, S. Ley, I. Merunka and J. Vrba, Microwave non-invasive temperature monitoring using UWB radar for cancer treatment by hyperthermia. Progress In Electromagnetics Research. 2018, 2018(162), 1-14. ISSN 1559-8985.

(2018: Q2, IF = 2,32, 2019: Q3, IF = 1,898).

Doi: <https://doi.org/10.2528/PIER17111609>

11.1.2 Publications not related to the thesis

[M7] Chovanec, M.; Zverina, E.; Profant, O.; Balogova, Z.; Kluh, J.; Syka, J.; Lisy, J.; Merunka, I. et al. Does Attempt at Hearing Preservation Microsurgery of Vestibular Schwannoma Affect Postoperative Tinnitus. BioMed Research International. 2015, 2015 ISSN 2314-6133. DOI 10.1155/2015/783169.

[M8] F Fík, Z.; Astl, J.; Zábrodský, M.; Lukeš, P.; Merunka, I.; Betka, J.; Chovanec, M, Minimally Invasive Video-Assisted versus Minimally Invasive Nonendoscopic Thyroidectomy. *BioMed Research International*. 2014, 2014(2014), ISSN 2314-6133. DOI 10.1155/2014/450170.

11.2 International conference contributions

11.2.1 Interbational conference contributions related to the thesis

[M9] MERUNKA, I., et al. 2D Microwave System for Testing of Brain Stroke Imaging Algorithm. In: *Proceedings of European Microwave Conference in Central Europe, EuMCE 2019*. 2019 European Microwave Conference in Central Europe, Praha, 2019-05-13/2019-05-15. Louvain-la-Neuve: European Microwave Association (EuMA), 2019. p. 508-511. ISBN 9782874870675.

[M10] MERUNKA, I., et al. Numerical analysis of microwave tomography system for brain stroke detection. In: FLIEGEL, K. and S. VÍTEK, eds. *2018 28th International Conference Radioelektronika*. 28th International Conference Radioelektronika 2018, Praha, 2018-04-19/2018-04-20. IEEE (Institute of Electrical and Electronics Engineers), 2018. p. 1-4. ISBN 978-1-5386-2485-2. DOI 10.1109/RADIOELEK.2018.8376398.

[M11] MERUNKA, I., et al. Comparison of Bowtie Slot and Rectangular Waveguide-Based Antennas for Microwave Medical Imaging. In: *2018 12th European Conference on Antennas and Propagation*. London, 2018-04-09/2018-04-13. Bruxelles: The European Association on Antennas and Propagation, 2018. ISSN 0537-9989. ISBN 978-1-78561-815-4. DOI 10.1049/cp.2018.0836.

[M12] MERUNKA, I., et al. Comparative Study of Antennas for Microwave Tomography. In: *Proceedings of Progress In Electromagnetics Research Symposium 2017*. Progress In Electromagnetics Research Symposium 2017, St. Petersburg, 2017-05-22/2017-05-25. Cambridge, MA: The Electromagnetics Academy, 2017. p. 1-4. ISSN 1559-9450. ISBN 978-1-5090-6269-0.

[M13] Kantová, M.; Fišer, O.; Merunka, I.; Vrba, J.; Tesařík, J., High-water Content Phantom for Microwave Imaging and Microwave Hyperthermia. In: LHOTSKÁ, L., et al., eds. *World Congress on Medical Physics and Biomedical Engineering 2018*. Prague, 2018-06-03/2018-06-08. Springer Nature Singapore Pte Ltd., 2019. p. 779-783. IFMBE Proceedings. vol. 68/2. ISSN 1680-0737. ISBN 978-981-10-9038-7. DOI 10.1007/978-981-10-9023-3_141.

[M14] Ley, L.; Fišer, O.; Merunka, I.; Vrba, J.; Sachs, J.; Helbig, M., Preliminary Investigations for Reliable Temperature Dependent UWB Dielectric Spectroscopy of Tissues and Tissue Mimicking Phantom Materials. In: *2018 12th European Conference on Antennas and Propagation*. London, 2018-04-09/2018-04-13. Bruxelles: The European Association on Antennas and Propagation, 2018. p. 1-5. ISSN 0537-9989. ISBN 978-1-78561-815-4. DOI 10.1049/cp.2018.0789.

[M15] Ley, L.; Fišer, O.; Merunka, I.; Vrba, J.; Sachs, J.; Helbig, M., Preliminary Investigations for Non-invasive Temperature Change Detection in Thermotherapy by Means of UWB Microwave Radar. In: *2018 40th Annual International Conference of the IEEE Engineering in Medicine and Biology Society (EMBC)*. Honolulu, HI, 2018-07-17/2018-07-21. Piscataway: IEEE, 2018. p. 5386-5389. ISSN 1557-170X. DOI 10.1109/EMBC.2018.8513555.

11.2.2 Abstracts related to the thesis

[M16] MERUNKA, I., et al. Temperature dependent complex permittivity of an agar phantom. In: ICHO 2016 - Scientific Program and Abstract Book. 2016 International Congress of Hyperthermic Oncology, New Orleans, Louisiana, 2016-04-11/2016-04-15. Lawrence: Society for Thermal Medicine, 2016. p. 180.

11.2.3 International conference contributions not related to the thesis

[M17] MERUNKA, I., O. FIŠER, and J. VRBA. E-field distribution measurement system for hyperthermia applicators with LED sensor. In: Proceedings of 14th Conference on Microwave Techniques, COMITE 2015. 14th Conference on Microwave Techniques COMITE 2015, Pardubice, 2015-04-21/2015-04-23. Budapešť: Institute of Electrical and Electronics Engineers Inc., 2015. p. 30-32. ISBN 9781479981212. DOI 10.1109/COMITE.2015.7120227.

[M18] MERUNKA, I., et al. Waveguide hyperthermia applicator with circular polarisation. In: VRBA, D., tvorba DALSIČH 9 AUTORU, and 3 AUTOR, eds. Progress in Electromagnetics Research Symposium in Prague. Progress in Electromagnetics Research Symposium, Prague, 2015-07-06/2015-07-09. Cambridge: Electromagnetics Academy, 2015. p. 2589-2592. ISSN 1931-7360. ISBN 9781934142301.

[M19] MERUNKA, I., et al. Array of Balanced Antipodal Vivaldi Antennas Used For Microwave Hyperthermia Treatment of Neck Cancer. In: ONDRÁČEK, O., et al., eds. 24th International Conference Radioelektronika 2014. Bratislava, 2014-04-15/2014-04-16. Bratislava: Slovak University of Technology, 2014. ISBN 978-1-4799-3715-8. DOI 10.1109/Radioelek.2014.6828451.

[M20] MERUNKA, I., et al. Utilization Potential of Balanced Antipodal Vivaldi Antenna for Microwave Hyperthermia Treatment of Breast Cancer. In: Conference Proceedings of EuCAP 2014. 8th European Conference on Antennas and Propagation, Haag, 2014-04-06/2014-04-11. Bruxelles: The European Association on Antennas and Propagation, 2014. p. 706-710. ISBN 978-88-907018-4-9. DOI 10.1109/EuCAP.2014.6901857. 6 citations w/o selfcitations

[M21] MERUNKA, I., et al. Microwave Hyperthermia Treatment of Neck Cancer Using Eight UWB Antennas. In: European Microwave Week 2014 Conference Proceedings. The 11th European Radar Conference, Rome, 2014-10-08/2014-10-10. London: Horizon House Publications, 2014. p. 790-793. ISBN 978-2-87487-034-7. DOI 10.1109/EuMC.2014.6986553.

[M22] VRBA, J., et al. Research of Biological Effects of em Field in Microwave Frequency Band. In: Progress in Electromagnetics Research Symposium. 2019 Photonics and Electromagnetics Research Symposium - Spring, PIERS-Spring 2019, Řím, 2019-06-17/2019-06-20. Institute of Electrical and Electronics Engineers, Inc., 2019. p. 1449-1451. ISSN 1559-9450. ISBN 9781728134031. DOI 10.1109/PIERS-Spring46901.2019.9017804.

[M23] FIŠER, O., I. MERUNKA, and J. VRBA. Numerical Study of Hyperthermia Applicator System for Tumor Treatment in Head and Neck Region. In: 2018 Progress In Electromagnetics Research Symposium (PIERS | Toyama). The 40th PIERS in Toyama, JAPAN, Toyama, 2018-08-01/2018-08-04. Cambridge: Electromagnetics Academy, 2018. p. 770-774. ISSN 1931-7360. ISBN 9784885523151. DOI 10.23919/PIERS.2018.8597679.

- [M24] FIŠER, O., et al. Numerical Study of Stroke Detection Using UWB Radar. In: 2018 Progress In Electromagnetics Research Symposium (PIERS | Toyama). The 40th PIERS in Toyama, JAPAN, Toyama, 2018-08-01/2018-08-04. Cambridge: Electromagnetics Academy, 2018. p. 160-163. ISSN 1931-7360. ISBN 9784885523151. DOI 10.23919/PIERS.2018.8597601.
- [M25] VRBA, J., et al. Microwaves in Medical Diagnostics and Treatment. In: 2018 Progress In Electromagnetics Research Symposium (PIERS | Toyama). The 40th PIERS in Toyama, JAPAN, Toyama, 2018-08-01/2018-08-04. Cambridge: Electromagnetics Academy, 2018. p. 155-159. ISSN 1931-7360. ISBN 9784885523151. DOI 10.23919/PIERS.2018.8597911.
- [M26] FIŠER, O., I. MERUNKA, and J. VRBA. Microwave Hyperthermia System for Head and Neck Area with Noninvasive UWB Temperature Change Detection. In: Proceedings of Progress In Electromagnetics Research Symposium 2017. Progress In Electromagnetics Research Symposium 2017, St. Petersburg, 2017-05-22/2017-05-25. Cambridge, MA: The Electromagnetics Academy, 2017. p. 1-6. ISSN 1559-9450. ISBN 978-1-5090-6269-0. DOI 10.1109/PIERS.2017.8262015.
- [M27] FIŠER, O., I. MERUNKA, and J. VRBA. Numerical Feasibility Study of New Combined Hyperthermia System for Head and Neck Region. In: European Microwave Week 2017 - Conference Proceedings - EuRAD 2017. European Microwave Week 2017 - EuRAD 2017, Nuremburg, 2017-10-08/2017-10-13. Louvain-la-Neuve: European Microwave Association (EuMA), 2017. p. 719-722. ISBN 978-2-87487-049-1. DOI 10.23919/EuMC.2017.8230948.
- [M28] VRBA, J., et al. Microwave based medical imaging. In: 2017 32nd General Assembly and Scientific Symposium of the International Union of Radio Science, URSI GASS 2017 p. 1-4. Volume 2017-January. ISBN 9789082598704. DOI 10.23919/URSIGASS.2017.8105081.
- [M29] VRBA, J., et al. Microwave hyperthermia applicators - Optimization of SAR and temperature distribution by aid of ferromagnetic nanoparticles. In: ICHO 2016 - Scientific Program and Abstract Book. 2016 International Congress of Hyperthermic Oncology, New Orleans, Louisiana, 2016-04-11/2016-04-15. Lawrence: Society for Thermal Medicine, 2016. p. 110.
- [M30] FIŠER, O., I. MERUNKA, and J. VRBA. Design, Evaluation and Validation of Planar Antenna Array for Breast Hyperthermia Treatment. In: Proceedings of 14th Conference on Microwave Techniques, COMITE 2015. 14th Conference on Microwave Techniques COMITE 2015, Pardubice, 2015-04-21/2015-04-23. Budapešť: Institute of Electrical and Electronics Engineers Inc., 2015. p. 33-36. ISBN 9781479981212. DOI 10.1109/COMITE.2015.7120228.
- [M31] MOLL, J., et al. Non-invasive microwave lung water monitoring: Feasibility study. In: Proceedings of the 9th European Conference on Antennas and Propagation (EUCAP 2015). 2015 9th European Conference on Antennas and Propagation, Lisbon, 2015-04-12/2015-04-17. Piscataway: IEEE, 2015. p. 1-4. ISBN 978-88-907018-5-6.
- [M32] VOJÁČKOVÁ, L., et al. Interstitial Applicators for Breast Cancer Treatment by Microwave Thermoablation. In: ONDRÁČEK, O., et al., eds. 24th International Conference Radioelektronika 2014. Bratislava, 2014-04-15/2014-04-16. Bratislava: Slovak University of Technology, 2014. ISBN 978-1-4799-3715-8. DOI 10.1109/Radioelek.2014.6828456.

11.3 Scientific projects participation

11.3.1 International projects

GAČR/17-20498J: “Non-invasive temperature estimation inside of human body based on physical aspects of ultra-wideband microwave channel”, 3-years project with DFG (2017-2019), supported by the Czech Science Foundation (Grant Agency of the Czech Republic), Member of the research team.

COST Action TD1301: “Development of a European-based Collaborative Network to Accelerate Technological, Clinical and Commercialization Progress in the Area of Medical Microwave Imaging”. Member of the research team.

COST Action BM1309: “European network for innovative uses of EMFs in biomedical applications (EMF-MED)”. Member of the research team.

11.3.2 National projects

GAČR/17-00477Y: “Physical nature of interactions of EM fields generated by MTM structures with human body and study of their prospective use in medicine”, 3-years project (2017-2019), supported by the Czech Science Foundation (Grant Agency of the Czech Republic), Member of the research team.

SGS17/182/OHK3/3T/13: “Development of optical sensors and systems and microwave biomedical technologies”, 3-years project (2017-2019), Member of the research team.

SGS14/189/OHK3/3T/13: “Interaction of the EM field with biological systems and their applications in medicine”, 3-years project (2014-2016), support of CTU in Prague. Member of the research team.

11.4 Memberships in conference organizing committee

Member of organizing committee of **PIERS 2015** (Progress in Electromagnetic Research, July 6 – 9, 2015, Prague, Czech Republic).

Member of organizing committee of **EuMCE 2019** (European Microwave Conference in Central Europe, May 13 – 15, 2019, Prague, Czech Republic)

11.5 International internships

9-11 / 2015, **National University of Ireland in Galway, Ireland**

Topic: Collaboration in areas of microwave hyperthermia and microwave tomography

In the frame of COST-STSM-TD1301-26530

2017 (4 x 1 week of workshops, Lodz, Barcelona, Coimbra, Budapest)

Starship innovation fellowship programme

Topic: Biodesign Concept

11.6 Special awards

Student Award for paper:

E-field Distribution Measurement System For Hyperthermia Applicators with LED Sensor at 14th Conference on Microwave Techniques **COMITE 2015**